The effect of uncertainty in MEG-to-MRI coregistrations on MEG inverse problems

Impressum

Max Planck Institute for Human Cognitive and Brain Sciences, 2020

Titelbild: © Hermann Sonntag, 2020

Druck: DRUCKEREI Ehnert & Blankenburg GmbH, Leipzig

ISBN 978-3-941504-90-5

The effect of uncertainty in MEG-to-MRI coregistrations on MEG inverse problems

Der Fakultät für
Informatik und Automatisierung
der Technischen Universität Ilmenau
eingereichte

Dissertation

zur Erlangung des akademischen Grades
Doktor-Ingenieur
Dr.-Ing.

vorgelegt
von Hermann Sonntag
geboren am 4. Mai 1986 in Pirna

Gutachter:
Prof. Dr.-Ing. habil. Jens Haueisen
Prof. Dr. rer. nat. Carsten Wolters
Prof. Gareth Barnes

Tag der Verteidigung: Ilmenau, den 19.12.2019

Abstract

For high precision in source estimates of magnetoencephalography (MEG) data, high accuracy of the coregistration of sources and sensors is mandatory. Usually, the source space is derived from magnetic resonance imaging (MRI). Sensor-to-MRI coregistrations are the focus of this thesis. The quality of coregistrations is assessed and the effect of their uncertainties on source estimates is analyzed. Both topics, the quality assessment and the propagation of uncertainties to source estimates are treated separately.

In this thesis, the target registration error (TRE) is proposed as criterion for the quality of sensor-to-MRI coregistrations. TRE measures the effect of uncertainty in coregistrations at all points of interest. In total, 5 544 data sets with sensor-to-head and 128 head-to-MRI coregistrations, from a single MEG laboratory, were analyzed. An adaptive Metropolis algorithm was used to estimate the optimal coregistration and to sample the coregistration parameters (rotation and translation). I found an average TRE between 1.3 and 2.3 mm at the head surface. A mean absolute difference in coregistration parameters between the Metropolis and iterative closest point algorithm of $(1.9 \pm 1.5)^\circ$ and (1.1 ± 0.9) mm was found. A paired sample t-test indicated a significant improvement in goal function minimization by using the Metropolis algorithm. The sampled parameters allowed computation of TRE on the entire grid of the MRI volume. Hence, I recommend the Metropolis algorithm for head-to-MRI coregistrations.

The propagation of coregistration uncertainty to source estimates was performed by using pseudospectral approximations of beamformer and standardized low resolution tomography (sLORETA). This approach was tested for auditory, visual and somatosensory brain activity with different signal to noise ratios and source orientation constraints on datasets of 20 subjects. By using pseudospectral approximations as efficient surrogates, the spatial distribution of the source estimate maximum was sampled for 50 000 coregistrations. From the results, it can be concluded that it is possible to apply stochastic spectral methods to MEG source estimation with high accuracy. The investigated effects of coregistration uncertainties on source estimates are small, typically the maximum location varied within a range of 5 mm, which is in the range of the localization errors. Pseudospectral approximations of the source estimates reduced computation times considerably by a factor of approximately 10 000 for beamformer and 50 000 for sLORETA compared to the exact original computations.

Kurzfassung

Für eine hohe Präzision in der Schätzung von Gehirnaktivität, ausgehend von Daten der Magnetoenzephalographie (MEG), ist eine sehr genaue Koregistrierung der Quellen und Sensoren notwendig. Üblicherweise werden hierbei die Quellorte der Gehirnaktivität bezüglich zu Koordinaten der Magnetresonanztomographie (MRI) angegeben. Die Sensor-zu-MRI Koregistrierungen sind der Schwerpunkt dieser Arbeit. Die Qualität von Koregistrierungen wird bewertet und der Effekt ihrer Unsicherheiten auf Schätzungen der Gehirnaktivität beziehungsweise auf Quellschätzungen wird untersucht. Beide Themen, die Qualitätsbewertung und die Übertragung der Unsicherheiten auf Quellschätzungen werden separat behandelt.

In dieser Arbeit wird vorgeschlagen, den *target registration error* (TRE) als Qualitätskriterium für Sensor-zu-MRI Koregistrierungen zu verwenden. Der TRE kann den Effekt von Koregistrierungsunsicherheiten an beliebigen Punkten messen. Insgesamt wurden 5 544 Datensätze mit Sensor-zu-Kopf und 128 Datensätze mit Kopf-zu-MRI Koregistrierungen aus einem Labor analysiert. Ein adaptiver Metropolis-Algorithmus wurde genutzt um optimale Koregistrierungen zu schätzen und um Stichproben ihrer Parameter (Rotation und Translation) zu ziehen. Es wurde ein TRE von 1.3 und 2.3 mm an der Kopfoberfläche gefunden. Weiter wurde eine mittlere absolute Differenz der Koregistrierungsparameter zwischen Metropolis-Algorithmus und dem etablierten *iterative closest point*-Algorithmus von $(1.9 \pm 1.5)^\circ$ und (1.1 ± 0.9) mm gefunden. Ein Zweistichproben-t-Test zeigte eine signifikante Verbesserung in der Optimierung der Zielfunktion durch den Metropolis-Algorithmus. Die Stichproben der Parameter erlaubten die Berechnung des TREs auf dem gesamten Gitter des MRI-Volumens.. Aus diesen Gründen wird der Metropolis-Algorithmus für Kopf-zu-MRI Koregistrierungen empfohlen.

Die Übertragung der Koregistrierungsunsicherheit auf Quellschätzungen erfolgte unter Verwendung von speziellen Polynom-Entwicklungen des *Beamformers* und der *standardized low resolution tomography* (sLORETA). Dieser Ansatz wurde für auditorische, visuelle und somatosensorische Hirnaktivität mit verschiedenen Signal-Rausch-Verhältnissen und Beschränkungen der Quellorientierung auf Datensätzen von 20 Probanden getestet. Durch die Verwendung von Polynom-Entwicklungen als effiziente Surrogate wurde die örtliche Verteilung des Quellschätzungs-Maximums für 50 000 Koregistrierungen ermittelt. Aus den Ergebnissen lässt sich schließen, dass es möglich ist, Polynom-Entwicklungen mit hoher Genauigkeit auf MEG-Quellschätzungen anzuwenden. Die untersuchten Auswirkungen von Koregistrierungsunsicherheiten auf Quellschätzungen sind gering, typischerweise variierte

die Position des Maximums innerhalb eines Bereichs von 5 mm, was im Bereich der Lokalisierungsfehler liegt. Polynom-Entwicklungen der Quellschätzungen reduzierten die Berechnungszeiten erheblich um den Faktor von etwa 10 000 für *Beamformer* und 50 000 für sLORETA im Vergleich zu den exakten Originalrechnungen.

Acknowledgements

This work was only possible through the great support of many individuals and I want to express my deep gratitude, appreciation and respect for them and their contributions.

In particular, I want to thank Dr. Burkhard Maeß for many fruitful discussions, suggestions and great support in all of my texts and presentations. He became my adviser, mentor and friend, he always found time to discuss my questions and concerns. Burkhard also helped a lot with his talent to make thoughts and texts clearer and easier to understand. I am very grateful to have Prof. Jens Haueisen as my advisor since my Bachelor thesis, I could count on his excellent support whenever I faced a scientific challenge. He guided me in each important step of my scientific career and I could benefit from his broad band of expertise in science and engineering. Thank you both for reading and commenting my manuscripts and this thesis. Further, I thank Prof. Angela Friederici for her support and for allowing me to finish my doctoral project at the Max Planck institute for human cognitive and brain sciences.

I want to thank Dr. Thomas Knösche for his profound comments and arguments in many discussions and meetings. It was a pleasure to meet and work with Dr. Konstantin Weise, he shared his knowledge and experiences and we had many insightful discussions. I also want to thank him for consistently answering my questions and for reading and commenting on the methods part of this thesis. It was a fortunate coincidence that I could talk to Matti Stenroos at a conference and I want to thank him for generously sharing his software. I really enjoyed working with Yvonne Wolff-Rosier, who always helped to implement an idea in the lab and her work attitude was positively infectious. She showed me how to conduct MEG measurements and in this domain her level of precision and rapidity is unbeatable. I want to thank my colleague and friend Tim Kunze, it was great to talk to him about science, life, just about everything.

Most importantly I want to thank my wonderful wife Laura for her love, patience and motivation during the long and sometimes difficult time. Her support allowed me to finish this project in a positive and joyful way. Finally, I want to thank my parents Christina and Tobias who always helped me to accomplish my dreams and ideas.

Hermann Sonntag
Leipzig, Mai 2019

Contents

Nomenclature

Abbreviations

A1	primary auditory cortex.
A4	auditory 4 complex.
A5	auditory 5 complex.
BA	broadman area.
BEM	boundary element method.
CC	correlation coefficent.
CPU	central processing unit.
EEG	electroencephalography.
FEM	finite element method.
GB	gigabyte.
LBelt	lateral belt complex.
LCMV	linearly constrained minimum variance.
MAG	magnification.
MBelt	medial belt complex.
MEG	magnetoencephalography.
MIPS	MIPS Technologies, Incorporation.

MRI magnetic resonance imaging.

PBelt para-belt complex.

PI para-insular area.

RAM random-access memory.

RDM relative difference measure.

RI retro-insular cortex.

RMS root mean square.

sLORETA standardized low resolution brain electromagnetic tomography.

SNR signal-to-noise ratio.

SSS signal space separation.

STSdp dorsal bank of superior temporal sulcus posterior.

SVD singular value decomposition.

TA2 anterior superior temporal area TA2 (Economo and Koskinas, 1925).

TM trademark.

TRE target registration error.

V1 primary visual cortex.

V2 second visual area.

Mathematical notation

A, a	scalar.
$\vec{a}$	spatial vector in three dimensional space.
$\boldsymbol{a}$	general vector.
$\lvert a \rvert$, $\lvert \boldsymbol{a} \rvert$	absolute value of a scalar and norm of a vector, respectively.
$\operatorname{diag}(\boldsymbol{a})$	diagonal matrix with diagonal elements $\boldsymbol{a}$.
$\bar{\vec{a}}$	expected value of a spatial vector.
$\mathbb{E}[\cdot]$	expected value.
$\operatorname{Var}[\cdot]$	variance.
$\hat{a}$, $\hat{\boldsymbol{a}}$	estimates of a scalar and a vector, respectively.
$.^{\mathsf{T}}$	transposed.
$\operatorname{quaternion}[\boldsymbol{R}]$	quaternion derived from a rotation matrix $\boldsymbol{R}$.
$\mathcal{A} \subseteq \mathcal{B}$	$\mathcal{A}$ is a subset of $\mathcal{B}$.
$\mathcal{A} \cup \mathcal{B}$	union of $\mathcal{A}$ and $\mathcal{B}$.
$\mathcal{A} \setminus \mathcal{B}$	set difference between $\mathcal{A}$ and $\mathcal{B}$: set of all elements that are members of $\mathcal{A}$ but not members of $\mathcal{B}$.

Chapter 1

Introduction

As soon as measured data are evaluated in fields of science or engineering, uncertainty analysis is an inevitable component of the interpretation of subsequent results. Uncertainty analysis is on the one hand the assessment of sources of uncertainty and on the other hand the estimation of the impact of these uncertainties on derived quantities. This kind of analysis is essential for all sorts of quality assessments or assurances. The aim of this thesis is the development of methods for systematic quality assessments and assurances in magnetoencephalography (MEG) analysis.

In many fields of medical engineering, quality assurance has high priority. There are several publications in radiation therapy and protection, computer tomography and magnetic resonance imaging (MRI) focusing on quality assessment and assurance only (Brendemühl et al., 2007; Weppler et al., 2018; Taguchi et al., 2018; Küstner et al., 2018). Extensive quality assurance are the basis of these diagnostic or therapeutic modalities for clinical applications. However, in the field of electroencephalography (EEG)/MEG this topic is underrepresented. The MEG is far from clinical routines, although it would offer some advantages like high temporal resolution together with the availability of simple volume conductor modelling. Therefore, it is necessary to develop the branch of quality assessments in the MEG field as a basis for clinical applications. This thesis is a contribution to verification and validation in neuroscience (Mulugeta et al., 2018) by means of analysing methods for testing the robustness of MEG models.

MEG measures the magnetic flux or flux differences at several sensors around the human head. The sources of interest of the measured magnetic flux data are intracranial electric currents of neural activity. An important aim of MEG analysis is to estimate parameters of these current sources e.g., the location and the ampli-

tude. The analysis step of source parameter estimation from measured MEG data is also referred to as source reconstruction. From the measurement to the source reconstruction, a number of other analysis steps are involved and each comes with its own uncertainties. Let me guide you from the perspective of an MEG data analyst from the measurement to the source reconstruction, focusing on uncertainties.

At the sensor level, the magnetic flux of intracranial currents is usually in the amplitude range of 1 to 100 fT and measurable frequencies range normally from 0.3 to 1 000 Hz (Y. Lin et al., 2018; Milde et al., 2009; Papadelis et al., 2009). This signal is interfered with magnetic flux of other electric currents within the human body e.g., currents in the heart and other muscles. These interferences with magnetic flux of the human body which do not originate in the brain are often referred to as artefacts in MEG analysis. Several deterministic (signal space projection, jump detection) (Nolte and Hämäläinen, 2001; Cheveigné and Arzounian, 2018) and non-deterministic (independent component analysis) methods (Escudero et al., 2007) are extensively used for artefact rejection or reduction. Another source of uncertainty at the sensor level is technical noise, either sensor noise or environmental noise. Technical noise is assumed to be a stationary random process and often it is considered a zero mean Gaussian process within a predefined frequency band (Hansen, Kringelbach, and Salmelin, 2010). Usually, it is described by its covariance matrix, which is either estimated from empty room measurements or from time intervals of measurements with subjects. None of these methods is able to detect or remove artefacts without uncertainty and usually this source of uncertainty and its effects are not analyzed.

Source reconstructions incorporate sensor level data, coregistration between the MEG device and subject's individual head coordinate system and preprocessed MRI data in computational models of the physical system. To this end, anatomical information of the MRI is used to model tissue conductivities and boundaries numerically in a volume conductor model. One first challenge is the computation of the magnetic field outside of the head for a certain electric source model within the brain, which is also referred to as forward solution. Both, conductivities and their boundaries can only be estimated with considerable uncertainties. Similar methods as in this thesis have already been employed to predict the effect of conductivity uncertainties on forward solutions and source reconstructions (De Staelen et al., 2013; Schmidt et al., 2014; Saturnino et al., 2019). Numerical methods like boundary element method (BEM) and finite element method (FEM) are used to compute forward solutions of realistic head models and they are in general computationally expensive. The reconstruction of cortical activity by means of single or distributed sources from MEG

measurements is an ill-posed inverse problem. Many of these inverse problems add a considerable computational burden on top of the computation of forward solutions. Inverse problems also add their uncertainties e.g. in source positions and densities and in the validity of their goal functions.

In the following, I briefly review some important uncertainty analysis methods and their properties, which might be useful for MEG computations. The focus, however, will be on stochastic spectral methods.

Monte Carlo sampling A sampling of deterministic computation results is referred to as Monte Carlo sampling, if the input is generated as independent realizations of random variables. The random variables in this context are defined beforehand by fixed probability distributions. This approach is straightforward since the computations stays unchanged and is only run for a number of input realizations. Hence, Monte Carlo sampling is a stochastic collocation method. From the samples of Monte Carlo computation results, statistics e.g., mean, variance and higher moments are estimated directly by using the estimators for independent random variables. However, the convergence rates of the statistics are slow e.g., $1/\sqrt{M}$ for the mean, where M is the sample size. The slow convergence renders Monte Carlo sampling unfeasible for computationally expensive problems. Accelerations of this method have been proposed e.g., latin hypercubes (Loh, 1996) or low-discrepancy point sets (Chen, Golberg, and Hon, 1998). These methods introduce a more systematic random sampling of computations, which increases convergence rates and thus reduces the number of necessary samples. However, for high dimensional parameter spaces and expensive computations, accelerated Monte Carlo sampling is still not practicable.

Perturbation methods If a computation result is the solution of a system of differential equations with stochastic parameters, the perturbation method can be applied. This method expands stochastic parameters by using truncated Taylor series around their mean. The Taylor series are substituted back into the differential equations and a more complex system of equations is obtained. Because of the complexity of the expanded system, the Taylor series is typically truncated at second order or below (Xiu, 2009). A subsequent limitation of perturbation methods is that they do not perform well for large magnitudes of uncertainties (Xiu, 2009; Ghanem and Spanos, 1991). The probability distribution function of the computation result cannot be readily computed from the perturbation method (Ghanem and Spanos, 1991).

Operator based methods The problem of solving differential equations is equivalent to the problem of finding the inverse of a given operator. If it exists, the inverse of an operator can be expanded in a convergent series (Ghanem and Spanos, 1991). By using a series expansion of the inverse operator, the solution of a stochastic differential equation can be expressed as a series of powers of the stochastic parameters. This expansion is similar to the perturbation method and also limited to uncertainties of small magnitudes (Xiu, 2009; Ghanem and Spanos, 1991). The inversion of the operator is usually extremely laborious and practically often restricted to the second order (Ghanem and Spanos, 1991).

Stochastic spectral methods A collection of methods for uncertainty analysis are generalizations of the 'Wiener-Hermite Chaos' (Xiu and Karniadakis, 2002; Xiu and Karniadakis, 2003; Xiu and Hesthaven, 2005). The computations are projected on an orthogonal polynomial basis in the space of the random parameters. In this work, such methods are referred to as stochastic spectral methods. In the literature, different terms are used for stochastic spectral methods, which can be confusing for the reader e.g., Wiener-Askey or generalized polynomial chaos (Xiu and Karniadakis, 2002; Xiu and Karniadakis, 2003; Weise et al., 2015). These methods have been applied to a variety of mathematical and physical computations with good convergence and efficiency (Ghanem and Spanos, 1991; Xiu and Karniadakis, 2002) and are considered among the most widely used methods for uncertainty analysis (Xiu, 2009). Stochastic spectral methods will be the focus of the uncertainty propagation chapter of this work. Ghanem and Spanos (1991) applied stochastic spectral methods to finite elments by using the polynomial basis as proposed by Wiener (1938). This method was generalized by Xiu and Karniadakis (2002) to polynomials of the Askey-scheme. From the perspective of application, the generalization by Xiu and Karniadakis (2002) extends the choice of stochastic parameter distributions from normal distributions to other continuous and discrete distributions. Stochastic spectral methods provide advantages over other uncertainty analysis methods, namely the availability of error measures for the approximation, expressions of statistical moments in closed forms and acceleration of the original simulator by means of a fast surrogate. The probability density function of computations can be approximately sampled by Monte Carlo sampling or one of its accelerations on the surrogate. An disadvantage of polynomial bases is that higher order polynomials are prone to unstable swings. In stochastic spectral methods, these swings can occur at places with a small likelihood in the input space. Another limitation of stochastic

spectral methods is that the probability distribution of the inputs must be known in order to select the correct polynomial basis.

Outline of this thesis This paragraph briefly outlines this thesis and ends with a list of its scientific contributions. In chapter 2, methods for estimating coregistration uncertainties are proposed. The focus is set on quality assessment and the multivariate distribution of coregistration parameters. Subsequently, stochastic spectral methods of uncertainty propagation are introduced in chapter 3. Applications to MEG forward computations and solutions of related inverse problems are explained in the same chapter. The results of both the coregistration uncertainty assessment and uncertainty propagation are presented in chapter 4. Discussion of the findings and conclusions of this thesis are given separately for uncertainty assessment and propagation in chapter 5.

The work presented in this thesis provides the following scientific contributions:

- Quality assessment of *MEG-to-MRI* coregistrations by using the target registration error (TRE) as a quality measure.
- Improvement of *head-to-MRI* coregistrations by using a Metropolis algorithm.
- Conjunction of coregistration uncertainties and head movements
- Propagation of uncertainty from coregistration to forward computations and source estimates.
- Sensitivity analysis of forward computations and source estimates for coregistration parameters.

Chapter 2

Assessment of coregistration uncertainties

2.1 Introduction to the problem

The accuracy of the coregistration for MEG source reconstructions is limited by stochastic and systematic errors in the three measurement modalities involved: MEG, 3D-digitizer and MRI. While several suggestions have been made in the past to improve the accuracy of the coregistrations (Singh et al., 1997; Adjamian et al., 2004; Troebinger et al., 2014; Meyer et al., 2017), no standard has been yet established. In this thesis I assess the quality of coregistrations using target registration error (TRE). TRE is an error vector, of a point localization, resulting from coregistration uncertainties. I propose a sequence of methods that are able to estimate TRE at any point of interest.

Coregistration procedures for MEG studies typically involve estimating sets of homologous positions, or coordinates, across at least two out of the three data modalities involved. Each of the three modalities, (MEG, 3D-digitizer and MRI), provides a unique device coordinate system. The MEG device coordinate system is defined by the MEG manufacturer to provide sensor positions. MRI acquires an image relative to scanner-specific coordinates. During 3D-digitization, anatomical landmarks are used to establish a subject-specific head coordinate system. Within this thesis, all positions will be reported relative to this head coordinate system. The term 'MEG coordinates' will refer to those which were originally given relative to the MEG device coordinate system and subsequently transformed to the 3D-digitized head coordinate system. Likewise, coordinates which are extracted from an MRI scan and transformed to the 3D-digitized head coordinate system, will be referred

to as 'MRI coordinates'. In practice, the results of brain activity studies are typically presented in head coordinates derived from brain internal fiducials only identifiable in structural MRI data, for example, MNI-coordinates[1] (Evans et al., 1993).

For convenience, I will use the following labels for the different coregistrations. MEG to head coordinate transformations will be referred to as *MEG-to-head* whereas head to MRI coordinate transformations will be referred to as *head-to-MRI*. Both are assumed to be proper rigid transformations (rotation and translation). To assess the overall quality of the two coregistrations as a unit, they will be linked and referred to as *MEG-to-MRI*.

There are a number of issues which contribute to coregistration uncertainty. During MEG recordings the positions of the localization coils (coils for short) are estimated via magnetic field measurements and inverse modeling. The solutions depend on signal quality and coil positions relative to the sensors (Ahlfors and Ilmoniemi, 1989; Fuchs et al., 1995). However, the coils make contact with the skin and can introduce error if their positions change while under tension. Further, MRI scans may show systematic spatial deformations of the head shape, for instance due to air-filled cavities in the head or even via physical deformations of the head surface, for example by headphones. In addition, estimation of the skin surface from MRI data depends on a threshold. The extracted surface may therefore appear systematically above or below the actual skin surface. According to Singh et al. (1997) defining anatomical landmarks, during the registration procedure, using two points on the ears and a third on the nasion only allows repeatability on the order of one millimeter at best. The overall accuracy of the 3D-digitizer is influenced by the precision in digitizing the coil positions and the head shape. However, during the digitization procedure these points can migrate slightly due to the elastic nature of the human skin. Finally, coordinate transformations are based either on matching corresponding points (fiducials) between two coordinate systems or on surfaces (surface matching). Pure fiducial based coregistrations are sensitive to fiducial localization errors and are highly likely to suffer larger errors than surface matching coregistrations when there are small numbers of fiducials (Singh et al., 1997; Huppertz et al., 1998).

Several techniques have addressed the problem of fiducial localization errors. One option is to fixate the participant's head using bite bars or head casts (Singh et al., 1997; Meyer et al., 2017). Another common approach is to digitize the

[1] At the Montreal Neurological Institute (MNI), brain atlases were constructed from different sets of MR images. Different atlases are also named according to the number of MR images, which are the basis of the atlases (e.g. MNI305).

coils and head surface relative to an additional reference, attached to the subject's head (Polhemus, 2012). This technique does account for head movements during digitization. However, the methods proposed in this thesis are also applicable to other *MEG-to-head* coregistrations, which use either different definitions of the head coordinate system or additional mechanical means.

Schwartz et al. (1996) compared the two registration families (fiducial-based and surface matching) with respect to the *head-to-MRI* coregistrations. They used between 2 000 and 4 000 head shape points for surface matching and 3 points for pure fiducial-based registrations. Their surface matching algorithm was based on a distance transform and the mean distance of all head shape points as cost function. They reported an accuracy improvement for the surface matching technique compared to manual registrations. The achieved accuracy of the registration was proportional to the number of head shape points. Registration errors of 0.7 ± 0.3 mm were reported, estimated on a 150 mm cube, sampled every 2 mm using simulation tests. Huppertz et al. (1998) also estimated the accuracy of a surface matching technique for *head-to-MRI* registrations for EEG data analysis. Between 1 000 to 1 800 head shape points were digitized and an iterative bisection search was used for surface matching. They computed mean registration errors of 1.4 to 1.8 mm for 7 fiducial points using a test–retest design with 10 repetitions and 20 subjects. The larger registration error compared to Schwartz et al. (1996) might be related to the points, where the registration error was measured. More specifically, Schwartz et al. (1996) defined an equidistant grid in the MRI volume, while Huppertz et al. (1998) used 7 fiducials at the head surface. Naturally, the points on the head surface show larger mean registration errors due to rotation uncertainties than fiducial points near the origin. Wagner and Fuchs (2001) used a similar approach to Huppertz et al. (1998) utilizing approximately 300 head shape points. Their algorithm minimizes the L^1-norm of the distances of head shape points to the MRI surface. Unfortunately, no information about the achieved accuracy was provided.

There is substantial variability in the literature concerning *head-to-MRI* coregistration methods. For example, handheld laser scanners (Koessler, Cecchin, et al., 2011; Hironaga et al., 2014) and photogrammetry systems (Koessler, Maillard, et al., 2007; Baysal and Şengül, 2010; Qian and Sheng, 2011) are proposed as alternatives to the electro-magnetic 3D digitization of electrode positions or head surface scanning. Baysal and Şengül (2010) used a single camera photogrammetry system for EEG electrode localization and reported a maximum localization error of 0.77 mm with 25 electrodes. In a similar setting, Qian and Sheng (2011) reported a maximum localization error of 1.19 mm. They used 2 mirrors in addition to the system of

Baysal and Şengül (2010). Koessler, Maillard, et al. (2007) compared a geodesic photogrammetry system with the *Polhemus FASTRAK* and other electrode digitization techniques. They reported an root mean square (RMS) position error of 1.27 mm for the geodesic photogrammetry system and 1.02 mm for the *Polhemus*. Koessler, Cecchin, et al. (2011) tested EEG-to-MRI coregistrations using a 3D laser scanner. An average of 5 263 face shape points were recorded and an iterative closest point (ICP) algorithm was applied to the face shapes. They reported a mean residual error of the electrode coregistration of 2.11 mm for 65 electrode positions. Hironaga et al. (2014) proposed a 3D laser scanner system for the *MEG-to-MRI* coregistration. They found superior registrations using the forehead surface compared to the upper head shape. Further, they reported that TRE was at the submillimeter level using their regional registration method. The methods, proposed below, can be directly applied to data sets of the photogrammetry and laser scanner systems as mentioned above.

Previous studies have often only provided RMS of matched point residuals, for example, residuals of coil positions or head shape points, as a measure of the goodness of fit. It has been shown, however, that these RMS of residuals and TRE are uncorrelated (Fitzpatrick, 2009). Hence, the RMS of residuals are not well suited for determining the quality of the coregistrations. Finally, previous studies concerned with the accuracy of coregistration measured or simulated TRE at only a few points (Fuchs et al., 1995; Singh et al., 1997; Huppertz et al., 1998; Adjamian et al., 2004). In this thesis I sample the distribution of coregistration parameters, and therefore TRE becomes a computable measure at any point of interest. Consequently, I propose an overall assessment of the quality of individual coregistrations based on TRE.

2.2 Instrumentation

All data sets in the analysis were recorded using a *Neuromag Vectorview* MEG with 102 planar magnetometers and 204 planar gradiometers. In the laboratory, five localization coils are always used. At the beginning of each measurement the five coils are energized by currents of unique frequencies. This allows one to disentangle the superimposed fields and to estimate each coil's position, with respect to the MEG device, separately. For the 3D-digitization of the coils and head shape, a *Polhemus FASTRAK* system was used, which has a accuracy specification of 0.8 mm RMS for all receiver positions in a radius of 760 mm from the transmitter (Polhemus, 2012). This distance is never exceeded in the lab. The MRI surface extraction is based on

the *Freesurfer* segmentation of 3 T T1-weighted MPRAGE or MP2RAGE images with a voxel size of 1 mm × 1 mm × 1 mm.

2.3 Head coordinate system

The definition of head coordinates depends on the MEG or EEG setup. In this thesis *Neuromag* head coordinates were used. This coordinate system is often referred to as RAS, which is a mnemonic for the axes' pointing directions: right, anterior and superior. The first axis of the head coordinate system is aligned with anatomical points on each ear, with coordinates increasing from left to right. The second axis intersects perpendicularly, at the origin with the first, such that it runs through the nasion from posterior. Thereby, the origin is not necessarily located at the middle between the ears. Again, the third axis intersects at the origin, perpendicular to the first and second axes and coordinates are counted positive from inferior towards the subject's vertex. This coordinate system was defined in Ahlfors and Ilmoniemi (1989) and is common for data acquisition with *Neuromag* devices (*Elekta Neuromag data acquisition user's manual* 2007, pages 25–26).

2.4 Rotation by quaternions

I used unit quaternions for the parametrization of rotations and their uncertainties for the following reasons. Quaternions provide a convenient four-dimensional representation of object rotations. They can be directly used to find the least squares solution of the coregistration of two corresponding point sets, while prohibiting reflections (Besl and McKay, 1992). This is an advantage over the singular value decomposition based method, which permits reflections and may thereby yield an improper rotation matrix. Furthermore, quaternion parameters provide an efficient method for three-dimensional rotations involving no trigonometric function computations. The quaternion-based rotation is continuous over the unit sphere in $\mathbb{R}^4$. The axis of a rotation is defined by a unit vector $\vec{u}$. A unit quaternion representing the rotation around $\vec{u}$ by an angle of θ is written as

$$\begin{aligned} \boldsymbol{q} &= \exp\left[(\theta/2)\left(u_1\boldsymbol{i} + u_2\boldsymbol{j} + u_3\boldsymbol{k}\right)\right] \\ &= \cos(\theta/2) + \left(u_1\boldsymbol{i} + u_2\boldsymbol{j} + u_3\boldsymbol{k}\right)\sin(\theta/2) \\ &= q_0 + q_1\boldsymbol{i} + q_2\boldsymbol{j} + q_3\boldsymbol{k}\,, \end{aligned} \tag{2.1}$$

where $\boldsymbol{i}$, $\boldsymbol{j}$ and $\boldsymbol{k}$ represent the three imaginary units of quaternions. Using eq. (2.1), the rotation of a vector $\vec{v}$ around $\vec{u}$ by an angle of θ is defined by

$$\vec{v}' = \boldsymbol{q}\,(v_1\boldsymbol{i} + v_2\boldsymbol{j} + v_3\boldsymbol{k})\,\boldsymbol{q}^{-1} = \boldsymbol{R}\,(\boldsymbol{q})\,\vec{v}\,, \tag{2.2}$$

where the inverse rotation quaternion $\boldsymbol{q}^{-1}$ is simply obtained by converting the sign of the exponent in eq. (2.1) and $\boldsymbol{R}\,(\boldsymbol{q})$ denotes the respective rotation matrix as a function of $\boldsymbol{q}$. In the scope of this thesis, the imaginary parts of the quaternion are referred to as rotation parameters and the real part is redundant for unit quaternions. The rotation matrix $\boldsymbol{R}\,(\boldsymbol{q})$ is derived from the quaternion without using trigonometric functions as

$$\boldsymbol{R}\,(\boldsymbol{q}) = \begin{pmatrix} q_0^2 + q_1^2 - q_2^2 - q_3^2 & 2\,(q_1q_2 - q_0q_3) & 2\,(q_1q_3 + q_0q_2) \\ 2\,(q_1q_2 + q_0q_3) & q_0^2 + q_2^2 - q_1^2 - q_3^2 & 2\,(q_2q_3 - q_0q_1) \\ 2\,(q_1q_3 - q_0q_2) & 2\,(q_2q_3 + q_0q_1) & q_0^2 + q_3^2 - q_1^2 - q_2^2 \end{pmatrix}, \tag{2.3}$$

see equation (21) in Besl and McKay (1992) for reference. In order to evaluate rotations using a spatial distance, the rotation effect at a radius R is used. On the plane orthogonal to the rotation axis, a rotation by an angle of θ relates to a distance of $R \cdot \theta$. The relation of angles and unit quaternion parameters is derived from

$$q_1^2 + q_2^2 + q_3^2 = \sin^2(\theta/2) \tag{2.4}$$

and for small angles $\theta \approx 2\sqrt{q_1^2 + q_2^2 + q_3^2}$. Hence the effect of rotations for points at the surface of a sphere, with a radius R, is approximated by multiplying them $(q_1\,, q_2\,, q_3)$ with the diameter of sphere $2R$. This scaling is used in section 2.10, where the rotation parameters are sampled together with the translation parameters in the 6-dimensional parameter space. I selected $R = 100\,\text{mm}$ as a scaling radius to approximate the radius of human heads.

2.5 Coregistration model

2.5.1 MEG-to-Head

This coregistration is based on $M < 10$ corresponding points, for example, coil positions. Coil positions were first measured by the 3D digitizer and expressed in the head coordinate system. They are estimated in MEG device coordinates based on fitting a magnetic dipole field for each coil using mne-python (Gramfort, 2013). The coregistration for the *MEG-to-head* alignment of the points $\boldsymbol{A} = (\vec{a}_1, \vec{a}_2, \ldots, \vec{a}_M)$

localized in the MEG and $\boldsymbol{B} = \left(\vec{b}_1, \vec{b}_2, \ldots, \vec{b}_M\right)$ digitized in the head coordinate system is given by

$$\vec{b}_m = \boldsymbol{R}(\boldsymbol{p})\,\vec{a}_m + \vec{s} + \vec{\epsilon}_m\,, \qquad m = 1, 2, \ldots, M\,, \tag{2.5}$$

where the transformation is defined by the quaternion $\boldsymbol{p}$ dependent rotation $\boldsymbol{R}$ and the translation $\vec{s}$ plus the error vector $\vec{\epsilon}_m$. The estimated solution to the coregistration problem is the set of parameters $\hat{\boldsymbol{p}}$ and $\hat{\vec{s}}$, which minimizes the residuals $\vec{\delta}_m$ in the least squares sense according to

$$\hat{\boldsymbol{p}},\, \hat{\vec{s}} = \underset{\boldsymbol{p},\,\vec{s}}{\operatorname{argmin}} \sum_{m=1}^{M} |\boldsymbol{R}(\boldsymbol{p})\,\vec{a}_m + \vec{s} - \vec{b}_m|^2 \tag{2.6}$$

$$\hat{\vec{b}}_m = \boldsymbol{R}(\hat{\boldsymbol{p}})\,\vec{a}_m + \hat{\vec{s}} \tag{2.7}$$

$$\vec{\delta}_m = \vec{b}_m - \hat{\vec{b}}_m\,. \tag{2.8}$$

I implemented the quaternion-based least squares solution for the problem in eq. (2.6) as proposed by Besl and McKay (1992).

For approximate parameter covariance estimation, the problem in eq. (2.5) is centred and linearized at the minimum of eq. (2.6) as

$$\vec{b}^{\,\mathsf{c}}_m = \boldsymbol{J}_m \cdot (\tilde{p}_1, \tilde{p}_2, \tilde{p}_3, \tilde{s}_1, \tilde{s}_2, \tilde{s}_3) + \vec{\epsilon}_m\,, \qquad m = 1, 2, \ldots, M\,, \tag{2.9}$$

where the superscript $^{\mathsf{c}}$ denotes vector subtraction of the respective mean $\frac{1}{M}\sum_{m=1}^{M}\vec{b}_m = \frac{1}{M}\sum_{m=1}^{M}\hat{\vec{b}}_m$ and the Jacobians read

$$\boldsymbol{J}_m = \begin{pmatrix} 0 & 2\hat{b}^{\mathsf{c}}_{3m} & -2\hat{b}^{\mathsf{c}}_{2m} & 1 & 0 & 0 \\ -2\hat{b}^{\mathsf{c}}_{3m} & 0 & 2\hat{b}^{\mathsf{c}}_{1m} & 0 & 1 & 0 \\ 2\hat{b}^{\mathsf{c}}_{2m} & -2\hat{b}^{\mathsf{c}}_{1m} & 0 & 0 & 0 & 1 \end{pmatrix}, \tag{2.10}$$

(Wheeler and Ikeuchi, 1995). Under the assumption of homoscedastic errors ϵ with zero mean and variance σ^2_ϵ, the parameter covariance matrix of the respective linear least squares estimate of the quaternion $\tilde{\boldsymbol{p}}$ and translation $\tilde{\vec{s}}$ yields

$$\operatorname{Var}\left[\tilde{p}_1, \tilde{p}_2, \tilde{p}_3, \tilde{s}_1, \tilde{s}_2, \tilde{s}_3\right] = \sigma^2_\epsilon \cdot \left(\boldsymbol{J}^{\mathsf{T}}\boldsymbol{J}\right)^{-1}\,, \tag{2.11}$$

see equation (2.1.6) in Björck (2015), where $\boldsymbol{J}^{\mathsf{T}} = \left(\boldsymbol{J}_1^{\mathsf{T}}, \boldsymbol{J}_2^{\mathsf{T}}, \ldots, \boldsymbol{J}_M^{\mathsf{T}}\right)$. As a result of the centring, there is no coupling between quaternion and translation parameters

and two matrices are derived separately as

$$\mathrm{Var}\left[\tilde{p}_1, \tilde{p}_2, \tilde{p}_3\right] = \sigma_\epsilon^2 \cdot \left(4 \sum_{m=1}^{M} \left(|\hat{\vec{b}}_m^{\mathsf{c}}|^2 \boldsymbol{I} - \hat{\vec{b}}_m^{\mathsf{c}} \hat{\vec{b}}_m^{\mathsf{c}\,\mathsf{T}}\right)\right)^{-1} \tag{2.12}$$

$$\mathrm{Var}\left[\tilde{s}_1, \tilde{s}_2, \tilde{s}_3\right] = \sigma_\epsilon^2 \cdot \boldsymbol{I}/M\,, \tag{2.13}$$

where $\boldsymbol{I}$ is the identity matrix of size 3. The right hand expression of eq. (2.12) is equivalent to a related variance estimate, see equation (33) in (Markley and Mortari, 2000).

2.5.2 Head-to-MRI

This is a coregistration of $N \sim 500$ points describing the head shape as measured by the 3D digitizer $\boldsymbol{D} = \left(\vec{d}_1, \vec{d}_2, \ldots, \vec{d}_N\right)$. A second list with a point matrix $\boldsymbol{E}$ is estimated via the segmented MRI data $\boldsymbol{E} = \{\vec{e}_1, \vec{e}_2, \ldots, \vec{e}_P\}$. The subset $\boldsymbol{F} = \left(\vec{f}_1, \vec{f}_2, \ldots, \vec{f}_N\right)$ that best corresponds to $\boldsymbol{D}$ depends on the quaternion $\boldsymbol{q}$ and the translation $\vec{t}$ and is the result of the closest point operator $\mathcal{C}$, defined by

$$\vec{f}_n = \underset{\vec{f}}{\mathrm{argmin}} |\boldsymbol{R}(\boldsymbol{q})\, \vec{d}_n + \vec{t} - \vec{f}|^2\,, \vec{f} \in \boldsymbol{E} \tag{2.14}$$

$$\boldsymbol{F} = \mathcal{C}\left(\boldsymbol{R}(\boldsymbol{q})\, \boldsymbol{D} + \vec{t}\mathbf{1}^{\mathsf{T}},\, \boldsymbol{E}\right)\,, \quad \mathbf{1}^{\mathsf{T}} = (1, \ldots, 1) \in \mathbb{R}^{1\times N}\,. \tag{2.15}$$

For the operator $\mathcal{C}$, I used an efficient balltree implementation of the *scikit-learn* module (Pedregosa et al., 2012). Omitting the explicit notation of $\mathcal{C}$, the *head-to-MRI* problem reads as

$$\vec{f}_n\left(\boldsymbol{q}, \vec{t}\right) = \boldsymbol{R}(\boldsymbol{q})\, \vec{d}_n + \vec{t} + \vec{\eta}_n\,, \qquad n = 1, 2, \ldots, N \tag{2.16}$$

and a solution is

$$\hat{\boldsymbol{q}}, \hat{\vec{t}} = \underset{\boldsymbol{q}, \vec{t}}{\mathrm{argmin}} \sum_{n=1}^{N} |\boldsymbol{R}(\boldsymbol{q})\, \vec{d}_n + \vec{t} - \vec{f}_n\left(\boldsymbol{q}, \vec{t}\right)|^2 \tag{2.17}$$

$$\hat{\vec{f}}_n = \boldsymbol{R}(\hat{\boldsymbol{q}})\, \vec{d}_n + \hat{\vec{t}} \tag{2.18}$$

$$\vec{\zeta}_n = \vec{f}_n\left(\hat{\boldsymbol{q}}, \hat{\vec{t}}\right) - \hat{\vec{f}}_n\,, \tag{2.19}$$

where $\vec{\eta}$ and $\vec{\zeta}_n$ are the error and residual vectors, respectively. In realistic setups, the optimization problem of eq. (2.17) may not have a unique solution and due to the non-linearity of $\mathcal{C}$, no closed-form solution is available. Thus, an approximate

solution is found using an iterative closest point (ICP) algorithm, which is likely to find local minima and therefore depends on the starting value (Besl and McKay, 1992). Hence, the starting value was manually set by utilizing the 3D-digitized ear and nasion points and the 3D rendered MRI segmentation of the head shape. The estimates $\left\{\hat{\boldsymbol{q}}, \hat{\vec{t}}\right\}$ were computed by the ICP implementation in mne-python (Gramfort, 2013). An overview of the coordinate system definitions and respective coregistration parameters is depicted in fig. 2.1.

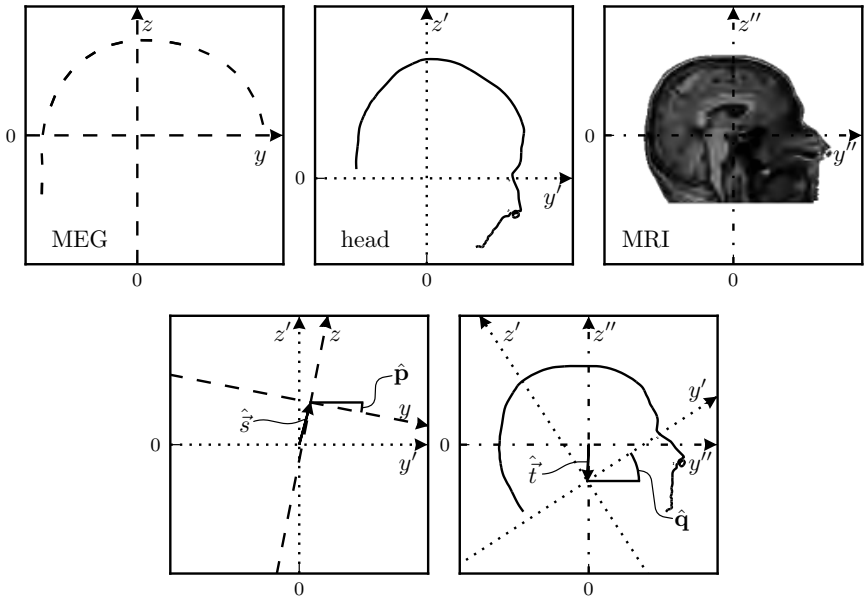

Figure 2.1: In the top row, the MEG, head and MRI coordinate systems are shown separately. The MEG coordinates are denoted by (y, z) and the respective axes are plotted by dashed lines relative to the contour of the MEG sensor configuration. Dotted lines represent the axes of the head coordinates (y', z') and the head contour is outlined within the respective coordinate frame. The MRI coordinate axes are plotted by dash-dotted lines, the respective coordinates are denoted by (y'', z'') and a sagittal MRI slice is shown accordingly. In the bottom row, the notations and line styles are adopted from the top row and MEG/head and head/MRI coordinates are depicted relative to each other in the left and right box, respectively. The parameter notations $\{\hat{\boldsymbol{p}}, \hat{\vec{s}}\}$ and $\{\hat{\boldsymbol{q}}, \hat{\vec{t}}\}$ denote rotations and translations of MEG-to-head and head-to-MRI, respectively. Axes scaling is identical for all of the five sub-figures.

2.6 Data sets

2.6.1 MEG-to-Head

MEG data sets measured in the MEG laboratory in the years from 2007 to 2016 were retrieved from the archive and analysed. For this thesis, the term 'MEG data set' denotes an MEG measurement block with coil position acquisition at the beginning of the block. All included data sets had five coils attached to the participant's head. I further restricted the selection to MEG data sets where none of the 204 gradiometers were marked as a bad channel. In agreement with *Elekta Neuromag data acquisition user's manual* (2007, pages 38–39), two further quality control criteria were taken into account. First, the goodness-of-fit value for each coil had to be 0.98 or larger. Second, the discrepancy between coil distances calculated from either MEG localization or from 3D digitization had to be smaller than 5 mm. In total, 7 314 MEG data sets were considered, 5 544 of them matched all of the selection criteria and formed the basis of the *MEG-to-head* coregistration analysis. A total of 1 770 MEG data sets were rejected, 7 had bad gradiometers, 81 because of no coil measurement, 349 had less than 5 active coils, 405 because of the discrepancy between coil distances and 928 had goodness-of-fit values below 0.98.

2.6.2 Head-to-MRI

For the *head-to-MRI* coregistrations, only those MEG data sets were considered for which a segmented MRI data set was available and which included more than 200 head shape digitization points. *Head-to-MRI* coregistrations were conducted using *MNE*, where the head surface extracted from MRI is matched with the 3D-digitized head shape using the ICP algorithm (Hämäläinen, 2010, pages 195–197). Head shape points with a distance greater than 10 mm from the MRI surface were excluded, as suggested by Hämäläinen (2010, page 317). A total of 128 *head-to-MRI* data sets were selected for the analysis. A total of 149 *head-to-MRI* data sets were rejected because they had less than 200 head shape points. Most of the rejected data sets were from a time prior to the laboratory adopting more strict procedures. The recommended number of head shape points was increased over the years.

2.7 Scales of the coordinate systems

When coregistering data sets of different modalities, but from the same participant (i.e. the same head), one would not expect a need to scale the dimensions. However, as briefly raised in the introduction, different methods may lead to systematic

differences in the metrical scaling. Thus far, I had assumed identical scalings in the different coordinate systems, that is, there is no change in length during the transformations. This assumption, however, can be checked by analysing distance measures within each coordinate system separately. The available data allowed pairwise comparisons of *MEG* with *head* and *head* with *MRI* coordinates. To this end, I conducted a singular value decomposition (SVD) of the centred point clouds in both coordinate systems. For convenience, I introduce the centring (demeaning) matrix for M points

$$\boldsymbol{C}_M = \boldsymbol{I} - \frac{1}{M}\mathbf{1}\mathbf{1}^\intercal\,, \tag{2.20}$$

where $\boldsymbol{I}$ is the identity matrix of size M and $\mathbf{1}\mathbf{1}^\intercal$ is an $M \times M$ matrix with each element equal to one. For the centred point sets in the two coordinate systems $\boldsymbol{A}^{\mathsf{c}} = \boldsymbol{A}\boldsymbol{C}_M$ and $\boldsymbol{B}^{\mathsf{c}} = \boldsymbol{B}\boldsymbol{C}_M$, this reads as

$$\boldsymbol{A}^{\mathsf{c}} = \boldsymbol{U}_A \operatorname{diag}(\vec{\sigma}_A)\, \boldsymbol{V}_A^\intercal \tag{2.21}$$

$$\boldsymbol{B}^{\mathsf{c}} = \boldsymbol{U}_B \operatorname{diag}(\vec{\sigma}_B)\, \boldsymbol{V}_B^\intercal \tag{2.22}$$

$$c = |\vec{\sigma}_A|/|\vec{\sigma}_B| \tag{2.23}$$

where $\vec{\sigma}_A$ and $\vec{\sigma}_B$ are the vectors of the positive singular values. The scaling coefficient c between two systems is the quotient of the l^2-norms of the singular value vectors. Table 2.1 shows a mean scaling of $c \simeq 1.005$ for *MEG-to-head*, which trans-

Table 2.1: Scaling statistics of MEG-to-head and head-to-MRI are tested (two-tailed t-test).

Type	**mean**	**SD**	***t*-value**	***p*-value**
MEG-to-head	1.005	0.007	50.309	< 0.001
Head-to-MRI	1.003	0.004	7.270	< 0.001

lates to a 0.5 mm difference at the head surface for a head radius of 100 mm. The expected error for the coil locations is in a similar range of about 1 mm (Ahlfors and Ilmoniemi, 1989; Fuchs et al., 1995). Thus, I assume that the *MEG* coordinates are systematically scaled by a factor of 1.005 and applied the correction to the *MEG* coordinates. The reason for this scaling effect might be the slight pressing force on the coils during digitization, which shifts the coils inwards and thus introduces a smaller scaling for digitization compared to MEG localization.

Table 2.1 shows a mean scaling of $c \simeq 1.003$ for *head-to-MRI*, which results in a 0.3 mm difference at the head surface. Both scaling values were significantly different from 1. However, I have taken into account only the first and ignored the

second. This is because of the large variability between subjects at the level of the surface extraction from MRI data sets, in comparison to the estimated scaling value. Furthermore, it is in agreement with Schwartz et al. (1996), who state that surface matching is scaling independent if scaling effects are smaller than 3 mm.

2.8 Coil localization errors

The *MEG-to-head* coregistration is based on coil localizations. Fuchs et al. (1995) investigated coil localization errors for three orthogonal coils (triplets), combined in a coil set, using a 31-channel Philips MEG. They found that the coil localization error depends on the coil position relative to the sensor array as well as on the signal strength. For a coil position below the sensor array they reported the difference between measured and true location to be less then 1.8 mm, with a mean of 1.1 mm. The *Neuromag Vectorview* device uses simpler single coils (no triplets) and it is a whole-head device with roughly ten times as many channels. I investigated the device-specific error magnitude and its spatial dependency for data with 102 planar magnetometers and 204 planar gradiometers. The coils were localized via their magnetic fields, each coil being modeled as a magnetic dipole (Fuchs et al., 1995). Coil localization was exclusively based on the data of the 204 gradiometers because gradiometers have a higher signal to noise ratio for nearby sources due to their inbuilt suppression of distant (interfering) sources. I estimated the variance of the noise via the norm of the misfit $\boldsymbol{\chi}$ between the magnetic flux sensor signals $\boldsymbol{s}$ and the modeled data

$$\boldsymbol{\chi}\left(\hat{\vec{r}}\right) = \boldsymbol{s} - \boldsymbol{G}\left(\hat{\vec{r}}\right)\boldsymbol{G}\left(\hat{\vec{r}}\right)^{+}\boldsymbol{s} \tag{2.24}$$

$$\sigma^2_{\mathsf{noise}} \sim \frac{|\boldsymbol{\chi}|^2}{204 - d}\,, \tag{2.25}$$

where $\boldsymbol{G}\left(\hat{\vec{r}}\right)$ is the leadfield of the magnetic dipole at $\hat{\vec{r}}$ and $\boldsymbol{G}\left(\hat{\vec{r}}\right)^{+}$ is the respective pseudoinverse. The optimization has $d = 6$ degrees of freedom for each coil and I assumed that the noise follows an independent *normal* distribution with zero mean, $\sigma^2_{\mathsf{noise}}$ variance and the respective probability density π_{noise} in each channel. Without prior knowledge about the parameters, the log-likelihood of the magnetic dipole location, given the measurement data, is defined by

$$\log \pi\left(\vec{r} \mid \boldsymbol{s}\right) = \sum_{l=1}^{204} \log \pi_{\mathsf{noise}}\left(\chi_l\left(\vec{r}\right)\right). \tag{2.26}$$

Samples are drawn from the probability density $\pi(\vec{r} \mid \boldsymbol{s})$ of the coil location, given the measurements, using the adaptive Metropolis algorithm of Haario, Saksman, and Tamminen (2001) on the log-likelihood, see eq. (2.26). I performed 10 000 runs of the Metropolis algorithm, including 1 000 burn-in samples. In this test, $5 \times 5\,544$ coil positions of the *MEG-to-head* data sets were included. The maximal spatial error was only weakly dependent on the location in space. I estimated the dependency to 1.5×10^{-3}, which represents 0.15 mm at a distance of 100 mm. Since this effect is about a 10-th of the expected maximal error, I assumed equal coil localization errors for the volume of interest. However, Fuchs et al. (1995) found a stronger dependency of the localization error on the position relative to the sensors. This effect is likely related to the shape of the sensor array, as they used a 31-channel *Phillips*-MEG with parallel sensor orientation and a smaller head coverage compared to the whole head, radially oriented sensor setup in this thesis.

2.9 Estimating errors from residuals

2.9.1 General considerations

This section is about the relation of errors, parameter estimates and residuals when parameters of a model are estimated from a sample of observations. For the case of coregistration estimation, the problem is defined in the previous section. Let me therefore explain the relation of errors, parameter estimates and residuals by investigating the *MEG-to-head* problem of eq. (2.5). M corresponding points are measured with three spatial dimensions in two coordinate systems. The problem is the estimation of parameters of a proper rigid transformation, namely rotation and translation, which transform the set of points from the first to the second system by means of the minimum sum of squared residuals. From measurements, the set of points are denoted by $\boldsymbol{A} = (\vec{a}_1, \vec{a}_2, \ldots, \vec{a}_M)$ and $\boldsymbol{B} = \left(\vec{b}_1, \vec{b}_2, \ldots, \vec{b}_M\right)$ in the first and second system respectively. Suppose, the vector set of the first system is already centred by defintion and hence

$$\sum_{k=1}^{M} \vec{a}_k = \vec{0}\,. \tag{2.27}$$

For the analysis of variances of residuals and parameter estimates, the problem of eq. (2.5) is transformed to the case, where the true rotation and translation

implement the identity operator $\boldsymbol{p}_{true} = (1,\, 0,\, 0,\, 0)$ and $\vec{s}_{true} = (0,\, 0,\, 0)^{\mathsf{T}}$:

$$\vec{b}_m = \boldsymbol{R}\,(\boldsymbol{p}_{true})\,\vec{a}_m + \vec{s}_{true} + \vec{\epsilon}_m = \vec{a}_m + \vec{\epsilon}_m\,. \tag{2.28}$$

Linearization at $\boldsymbol{p}_{true}$, $\vec{s}_{true}$ and least squares fitting of the parameters gives

$$\begin{aligned} \vec{b}_m &= \vec{a}_m + \boldsymbol{J}_m\boldsymbol{\nu} + \vec{\delta}_m \\ \boldsymbol{\nu} &= (p_1,\, p_2,\, p_3,\, s_1,\, s_2,\, s_3)^{\mathsf{T}} \end{aligned} \tag{2.29}$$

where $\boldsymbol{J}_m$ is the Jacobian of rotation and translation for the point $\vec{a}_m$ at $\boldsymbol{p}_{true}$, $\vec{s}_{true}$ and $\vec{\delta}_m$ are the residuals. The real quaternion part p_0 of the Jacobian vanishes at $\boldsymbol{p}_{true}$ and hence the Jacobian reduces to the imaginary quaternion and translation. According to eq. (2.29), the Jacobian reads

$$\boldsymbol{J}_m = \begin{pmatrix} 0 & 2a_{3m} & -2a_{2m} & 1 & 0 & 0 \\ -2a_{3m} & 0 & 2a_{1m} & 0 & 1 & 0 \\ 2a_{2m} & -2a_{1m} & 0 & 0 & 0 & 1 \end{pmatrix}. \tag{2.30}$$

For the following consideration, the matrices $\boldsymbol{A}$ and $\boldsymbol{B}$ are vectorized to $\boldsymbol{a}$ and $\boldsymbol{b}$ by means of

$$\boldsymbol{a} = \left(\vec{a}_1^{\mathsf{T}},\, \vec{a}_2^{\mathsf{T}}, \ldots, \vec{a}_M^{\mathsf{T}}\right)^{\mathsf{T}} = (a_{11},\, a_{21}, \ldots, a_{3M})^{\mathsf{T}} \in \mathbb{R}^{3M}\,, \tag{2.31}$$

the according error vector is $\boldsymbol{\epsilon} = \boldsymbol{b} - \boldsymbol{a}$ and the Jacobian becomes

$$\boldsymbol{J} = \left(\boldsymbol{J}_1^{\mathsf{T}},\, \boldsymbol{J}_2^{\mathsf{T}}, \ldots, \boldsymbol{J}_M^{\mathsf{T}}\right)^{\mathsf{T}} \in \mathbb{R}^{3M\times 6}\,. \tag{2.32}$$

In vectorized form, the relation between errors, parameter estimates and residuals of the linearized problem reads

$$\boldsymbol{\epsilon} = \boldsymbol{J}\boldsymbol{\nu} + \boldsymbol{\delta} \tag{2.33}$$

The least squares solution parameters $\boldsymbol{\nu}$ can be simply expressed by singular value decomposition (SVD) of the Jacobian

$$\boldsymbol{J} = \boldsymbol{U}_{\{1,\ldots,3M\}\{1,\ldots 6,\}}\boldsymbol{S}\boldsymbol{V}^{\mathsf{T}} \tag{2.34}$$

$$\boldsymbol{\nu} = \boldsymbol{V}\boldsymbol{S}^{-1}\boldsymbol{U}^{\mathsf{T}}_{\{1,\ldots,6\}\{1,\ldots,3M\}}\boldsymbol{\epsilon}\,, \tag{2.35}$$

where $\boldsymbol{U} \in \mathbb{R}^{3M\times 3M}$, $\boldsymbol{V} \in \mathbb{R}^{6\times 6}$ are orthogonal matrices, and $\boldsymbol{S} \in \mathbb{R}^{6\times 6}$ is a diagonal matrix. Left multiplication of eq. (2.33) by $\boldsymbol{U}^{\mathsf{T}}$ and substitution of the Jacobian by its SVD gives

$$\tilde{\boldsymbol{\epsilon}} = \boldsymbol{U}^{\mathsf{T}}\boldsymbol{\epsilon} = \boldsymbol{U}^{\mathsf{T}}\boldsymbol{U}_{\{1,\ldots,3M\}\{1,\ldots 6,\}}\boldsymbol{S}\boldsymbol{V}^{\mathsf{T}}\boldsymbol{\nu} + \boldsymbol{U}^{\mathsf{T}}\boldsymbol{\delta}\,. \tag{2.36}$$

With eq. (2.35), it is obvious that

$$\boldsymbol{U}^{\mathsf{T}}_{\{1,\dots,6\}\{1,\dots,3M\}}\boldsymbol{\delta} = (0,\,0,\dots,0) \in \mathbb{R}^6 \tag{2.37}$$

and for shorter notation

$$\tilde{\boldsymbol{\delta}} = \boldsymbol{U}^{\mathsf{T}}_{\{7,\dots,3M\}\{1,\dots,3M\}}\boldsymbol{\delta} \in \mathbb{R}^{3M-6}\,. \tag{2.38}$$

To summarize the last steps, the residuals are projected onto its $3M-6$ dimensional subspace by the left multiplication of $\boldsymbol{U}^{\mathsf{T}}$, respectively the first 6 elements of this projection become zero and only the last $3M-6$ elements are of interest and referred to as $\tilde{\boldsymbol{\delta}}$. Because of the orthogonality of $\boldsymbol{U}$

$$\tilde{\boldsymbol{\epsilon}} = \boldsymbol{f}\left(\boldsymbol{\nu},\,\tilde{\boldsymbol{\delta}}\right) = \begin{pmatrix} \boldsymbol{S}\boldsymbol{V}^{\mathsf{T}} & \boldsymbol{0} \\ \boldsymbol{0}^{\mathsf{T}} & \boldsymbol{I} \end{pmatrix}\left(\boldsymbol{\nu},\,\tilde{\boldsymbol{\delta}}\right)^{\mathsf{T}},\boldsymbol{I} \in \mathbb{R}^{(3M-6)\times(3M-6)},\boldsymbol{0} \in \mathbb{R}^{6\times(3M-6)}\,, \tag{2.39}$$

where $\boldsymbol{I}$ is an identity matrix and $\boldsymbol{0}$ is a zero matrix. The Jacobian of $\boldsymbol{f}$ is of importance for the change of variables later and defined as

$$\boldsymbol{J}_{\boldsymbol{f}} = \begin{pmatrix} \boldsymbol{S}\boldsymbol{V}^{\mathsf{T}} & \boldsymbol{0} \\ \boldsymbol{0}^{\mathsf{T}} & \boldsymbol{I} \end{pmatrix}. \tag{2.40}$$

For the following consideration, a multivariate *normal* error distribution is assumed with

$$\boldsymbol{\epsilon} \sim \mathcal{N}\left(\boldsymbol{0}, \sigma_\epsilon^2 \boldsymbol{I}\right),\boldsymbol{I} \in \mathbb{R}^{3M\times 3M} \tag{2.41}$$

and because of the orthogonality of $\boldsymbol{U}$ it is straightforward to conclude that also

$$\tilde{\boldsymbol{\epsilon}} \sim \mathcal{N}\left(\boldsymbol{0}, \sigma_\epsilon^2 \boldsymbol{I}\right),\boldsymbol{I} \in \mathbb{R}^{3M\times 3M}\,. \tag{2.42}$$

The probability density function of a multivariate *normal* distribution with zero mean and full rank covariance matrix $\boldsymbol{C} \in \mathbb{R}^{N\times N}$ reads

$$\pi_\xi\left(\boldsymbol{\xi}\right) = \frac{1}{\sqrt{(2\pi)^N\left|\boldsymbol{C}\right|}}\exp\left[\frac{1}{2}\boldsymbol{\xi}^{\mathsf{T}}\boldsymbol{C}^{-1}\boldsymbol{\xi}\right], \tag{2.43}$$

which yields in case of the errors

$$\pi_{\tilde{\epsilon}}\left(\tilde{\boldsymbol{\epsilon}}\right) = \frac{1}{\sqrt{(2\pi)^{3M}\,\sigma_\epsilon^{6M}}}\exp\left[\frac{1}{2\sigma_\epsilon^2}\tilde{\boldsymbol{\epsilon}}^{\mathsf{T}}\tilde{\boldsymbol{\epsilon}}\right]. \tag{2.44}$$

A change of variables gives the joint probability density of parameter estimates and residuals as

$$\pi_{\nu,\tilde{\delta}}\left(\boldsymbol{\nu},\,\tilde{\boldsymbol{\delta}}\right) = |\det \boldsymbol{J_f}| \frac{1}{\sqrt{(2\pi)^{3M}\,\sigma_\epsilon^{6M}}} \exp\left[\frac{1}{2\sigma_\epsilon^2}\left(\boldsymbol{\nu}^\mathsf{T}\boldsymbol{V}\boldsymbol{S}^2\boldsymbol{V}^\mathsf{T}\boldsymbol{\nu} + \tilde{\boldsymbol{\delta}}^\mathsf{T}\tilde{\boldsymbol{\delta}}\right)\right], \tag{2.45}$$

where $|\det \boldsymbol{J_f}| = \sqrt{|\det \boldsymbol{J}^\mathsf{T}\boldsymbol{J}|}$ and

$$\boldsymbol{J}^\mathsf{T}\boldsymbol{J} = \boldsymbol{V}\boldsymbol{S}^2\boldsymbol{V}^\mathsf{T} \begin{pmatrix} 4\sum_{m=1}^{M}\left(|\vec{a}_m|^2\boldsymbol{I} - \vec{a}_m\vec{a}_m^\mathsf{T}\right) & \boldsymbol{0} \\ \boldsymbol{0} & M\boldsymbol{I}\,. \end{pmatrix} \tag{2.46}$$

The marginal probability densities of the parameter estimates and residuals are found by

$$\begin{aligned} \pi_\nu\left(\boldsymbol{\nu}\right) &= \frac{1}{\sqrt{(2\pi)^{3M}\,\sigma_\epsilon^{6M}|\det\left(\boldsymbol{J}^\mathsf{T}\boldsymbol{J}\right)^{-1}|}} \int_{\Omega\tilde{\boldsymbol{\delta}}} \exp\left[\frac{1}{2\sigma_\epsilon^2}\left(\boldsymbol{\nu}^\mathsf{T}\boldsymbol{J}^\mathsf{T}\boldsymbol{J}\boldsymbol{\nu} + \tilde{\boldsymbol{\delta}}^\mathsf{T}\tilde{\boldsymbol{\delta}}\right)\right]\mathrm{d}\tilde{\boldsymbol{\delta}} \\ &= \frac{1}{\sqrt{(2\pi)^{6}\,|\det\left(\boldsymbol{J}^\mathsf{T}\boldsymbol{J}/\sigma_\epsilon^2\right)^{-1}|}} \exp\left[\frac{1}{2\sigma_\epsilon^2}\boldsymbol{\nu}^\mathsf{T}\boldsymbol{J}^\mathsf{T}\boldsymbol{J}\boldsymbol{\nu}\right] \end{aligned} \tag{2.47}$$

and accordingly

$$\pi_{\tilde{\delta}}\left(\tilde{\boldsymbol{\delta}}\right) = \frac{1}{\sqrt{(2\pi)^{3M-6}\,\sigma_\epsilon^{2(3M-6)}}} \exp\left[\frac{1}{2\sigma_\epsilon^2}\tilde{\boldsymbol{\delta}}^\mathsf{T}\tilde{\boldsymbol{\delta}}\right]. \tag{2.48}$$

From eq. (2.47) follows the covariance of the parameter estimates as

$$\boldsymbol{C}_{\hat{p}_1,\hat{p}_2,\hat{p}_3} = \sigma_\epsilon^2\left(4\sum_{m=1}^{M}\left(|\vec{a}_m|^2\boldsymbol{I} - \vec{a}_m\vec{a}_m^\mathsf{T}\right)\right)^{-1} \tag{2.49}$$

$$\boldsymbol{C}_{\hat{\tilde{s}}} = \left(\sigma_\epsilon^2/M\right)\boldsymbol{I}\,, \tag{2.50}$$

which is equivalent to equation (33) in (Markley and Mortari, 2000) for the quaternion parameters and the well known $\sqrt{1/M}$ characteristic for the standard error of the mean. Since $\boldsymbol{\delta} = \boldsymbol{U}_{\{1,\ldots,3M\}\{7,\ldots,3M\}}\tilde{\boldsymbol{\delta}}$, the residuals are linear combinations of $\tilde{\boldsymbol{\delta}}$ and hence are *normally* distributed as well. The variance estimate of the residuals σ_δ^2 relates to σ_ϵ^2 in the probability density of the sum of squares $x = \sum_{m=1}^{3M-6}\tilde{\delta}_m^2$, with the expected value of $\mathbb{E}\left[x^2\right] = (3M-6)\,\sigma_\epsilon^2$. Because $\boldsymbol{U}$ is orthogonal and therefore does not change the sum of squares of a vector by matrix multiplication, it follows $\sum_{m=1}^{3M}\delta_m^2 = \sum_{m=1}^{3M-6}\tilde{\delta}_m^2$. From this relation follows the dependence of the variances

of residuals and errors as

$$\sigma_{\delta}^2 = \frac{3M-6}{3M}\sigma_{\epsilon}^2 \,. \tag{2.51}$$

So far, a *normal* error distribution was assumed and the distribution of the residuals was derived accordingly. In reality, the distribution of the errors is not known a priori and needs to be inferred from the residuals. For the inference of errors from residuals in the more general case compared to eq. (2.48), the error probability density is only available in implicit form of the integral equation

$$\pi_{\tilde{\delta}}\left(\tilde{\boldsymbol{\delta}}\right) = \int_{\Omega\boldsymbol{\nu}} \pi_{\epsilon}\left(\boldsymbol{U}\boldsymbol{\epsilon}\right) \mathrm{d}\boldsymbol{\nu} \,. \tag{2.52}$$

However, there might not be an analytical solution for eq. (2.52) and the estimation of the complete $\pi_{\tilde{\delta}}$ is prone to errors because of the high dimensionality of $\tilde{\boldsymbol{\delta}}$. Further, in the case of coregistration estimation over different subjects respectively different point set configurations, the Jacobian of the transformation changes for each configuration and it is impossible to estimate $\pi_{\tilde{\delta}}$. Therefore, I suggest to infer the error distribution numerically by simulation of residuals from theoretical error distributions. The integral in eq. (2.52) may change the shape of the probability density e.g., from a triangular to a uniform density, but the distribution family is not changed as drastically e.g., the uniform and triangular densities are both special cases of the trapezoidal distribution. Therefore, it is nearby to infer the distribution family of the errors from the residuals. This conclusion is applied in the next section in order to estimate the error probability density.

2.9.2 Inference of errors by simulation

All residuals $\vec{\delta}_m$ and $\vec{\zeta}_n$, as defined in section 2.5, were separately concatenated from either $K = 5\,544$ *MEG-to-head* or $L = 128$ *head-to-MRI* coregistrations in the samples Δ and Z, respectively. The empirical distribution functions of a sample Δ of size K is denoted by $F_{\delta,\,K}$ and may be defined in terms of the order statistics $\Delta_{(1)} \leq \Delta_{(2)} \leq \cdots \leq \Delta_{(K)}$ by

$$F_{\delta,\,K}\left(x\right) = \begin{cases} 0 & \text{if } x < \Delta_{(1)} \\ k/K & \text{if } \Delta_{(k)} < x \leq \Delta_{(k+1)},\; 1 \leq k < K \\ 1 & \text{if } x \geq \Delta_{(K)} \end{cases} \tag{2.53}$$

(Pratt and Gibbons, 1981, their equation (2.1)). I modelled the distributions of the error elements of $\vec{\epsilon}_m$ and $\vec{\eta}_n$ using theoretical distributions for continuous random

variables, for example, a logistic or a *normal* distribution. However, the errors cannot be assessed directly. Therefore, the optimal theoretical distribution for the errors is chosen on the basis of the distributions of the residuals. From a list of continuous candidate distributions I selected those with no, or one, shape parameter. These were implemented in *scipy* and had good convergence (excluding *rice* and *erlang* distributions). Overall, these criteria resulted in a list of 69 distributions. For the n-th candidate with distribution function $G_{n,\,0}\,(x \mid \lambda_n,\, \mu_n,\, \sigma_n)$, the parameters shape λ_n, mean μ_n and scale σ_n were optimized according to

$$\hat{\boldsymbol{y}}_{\delta,\,n} = \underset{\lambda,\,\mu,\,\sigma}{\operatorname{argmin}} \left\{ \sup_x \left| F_{\delta,\,K}\,(x) - G_{n,\,0}\,(x \mid \lambda,\, \mu,\, \sigma) \right| \right\} \tag{2.54}$$

$$\hat{\boldsymbol{y}}_{\zeta,\,n} = \underset{\lambda,\,\mu,\,\sigma}{\operatorname{argmin}} \left\{ \sup_x \left| F_{\zeta,\,L}\,(x) - G_{n,\,0}\,(x \mid \lambda,\, \mu,\, \sigma) \right| \right\} \tag{2.55}$$

$$n = 1,\, 2,\, \ldots 69\,,$$

where the optimization argument is the one-sample, two-sided Kolmogorov–Smirnov statistic (Pratt and Gibbons, 1981, their equation (7.1)). The *generalized normal* and the *Students's* t-distribution yielded the smallest Kolmogorov–Smirnov statistics in eq. (2.56) for the *MEG-to-head* $F_{\delta,\,K}\,(x)$ and *head-to-MRI* $F_{\zeta,\,L}\,(x)$, respectively.

The best fitting distributions were used as a basis to simulate residuals. Utilizing the *generalized normal* distribution $\mathcal{GN}\left(\lambda,\, 0,\, \sigma^2\right)$ for $\tilde{\epsilon}$ I simulated $\tilde{\delta}\left(\lambda,\, \sigma^2\right)$ by replacing $\vec{a}_m$ with $\tilde{\vec{a}}_m = \vec{b}_m + \tilde{\vec{\epsilon}}_m$ in eq. (2.6). Accordingly, with the *Student's t*-distribution with shape λ and scale τ for $\tilde{\zeta}$ the residuals $\tilde{\eta}\left(\lambda,\, \sigma^2\right)$ are simulated by replacing $\vec{d}_n$ with $\tilde{\vec{d}}_n = \mathcal{C}\left(\hat{\vec{d}}_n,\, \boldsymbol{E}\right) + \tilde{\vec{\zeta}}_n$ in eq. (2.17). The two-sample, two-sided Kolmogorov–Smirnov statistics (Pratt and Gibbons, 1981, their equation (3.1))

$$D_{\tilde{\delta}}\,(\lambda,\, \sigma) = \max_x \left| F_{\delta,\,K}\,(x) - F_{\tilde{\delta},\,K}\,(x \mid \lambda,\, \sigma) \right| \text{ and} \tag{2.56}$$

$$D_{\tilde{\zeta}}\,(\lambda,\, \sigma) = \max_x \left| F_{\zeta,\,L}\,(x) - F_{\tilde{\zeta},\,L}\,(x \mid \lambda,\, \sigma) \right| \tag{2.57}$$

were scanned for the set of parameters given in table 2.2, which was selected in proximity of the optimum. Additionally, the *normal* distribution was tested for comparison (table 2.2). Scanning of the Kolmogorov–Smirnov goal function is not deterministic since I drew samples from a distribution to simulate errors and residuals. Therefore, error estimates of the Kolmogorov–Smirnov statistics were computed via multiple simulations of error distribution parameters, more specifically, 5 simulations for *MEG-to-head* and 10 simulations for *head-to-MRI*. For *head-to-MRI*, 5 simulations were insufficient because of higher variability in the correspond-

Table 2.2: Shape and scale parameters of the error distributions that were used to scan the Kolmogorov–Smirnov goal function.

Type	**name**	**shape**	**scale in mm**
MEG-to-head	*Gen. normal*	1.7, 1.8 . . . 2.1	1.30, 1.35 . . . 1.55
	Normal		0.90, 0.95 . . . 1.10
Head-to-MRI	*Student's t*	3, 4 . . . 7	0.90, 1.00 . . . 1.30
	Normal		1.30, 1.35 . . . 1.60

ing Kolmogorov–Smirnov statistic. The minimum of the Kolmogorov–Smirnov goal function corresponds to a certain distribution function, which is taken as a model to approximate the error distribution. Hence, these distribution parameters were utilized to sample the coregistration parameters in the following section.

2.10 Coregistration parameter sampling

In the previous section I approximated the distribution of errors for the point measurement in the coregistration problem of eq. (2.5) and eq. (2.16). I denoted the probability densities of the error distributions by π_ϵ and π_η for *MEG-to-head* and *head-to-MRI*, respectively. For the sampling of coregistration parameter distributions, I considered the centred and pre-registered problems. The centring matrix transforms the coregistration points into their centred representation, for example, $\boldsymbol{B}^{\mathsf{c}}$. During pre-registration, coordinates from each modality are converted to head coordinates and aligned with the corresponding data set. Having already applied a least squares or ICP optimization, all that remains in terms of error is the misalignment between the sets of data points and hence $\hat{\boldsymbol{p}} = \hat{\boldsymbol{q}} = \boldsymbol{0}$ and $\hat{\vec{s}} = \hat{\vec{t}} = \vec{0}$.

Log probability densities of a spatial error vector (e.g. $\vec{a}$) are defined by

$$\log \pi\left(\vec{a}\right) = \sum_{n=1}^{3} \log \pi\left(a_n\right).$$

The log-likelihood of the *MEG-to-head* parameters $\{\boldsymbol{p}, \vec{s}\}$, given the observation $\boldsymbol{B}^{\mathsf{c}}$ and $\hat{\boldsymbol{B}}^{\mathsf{c}}$ reads

$$\log \rho\left(\boldsymbol{p},\, \vec{s} \mid \boldsymbol{B}^{\mathsf{c}},\, \hat{\boldsymbol{B}}^{\mathsf{c}}\right) = \sum_{m=1}^{M} \log \pi_{\hat{\epsilon}}\left[\boldsymbol{R}\left(\boldsymbol{p}\right) \hat{\vec{b}}^{\mathsf{c}}_m + \vec{s} - \vec{b}^{\mathsf{c}}_m\right]. \tag{2.58}$$

For the log-likelihood of the *head-to-MRI* parameters $\left\{\boldsymbol{q}, \vec{t}\right\}$, given the observation $\boldsymbol{F}^{\mathsf{c}}$ and $\hat{\boldsymbol{F}}^{\mathsf{c}}$, the additional closest point operator $\mathcal{C}$ is required and $\log \phi$ is therefore equivalently defined as

$$\log \phi \left(\boldsymbol{q},\, \vec{t} \,|\, \boldsymbol{E}^{\mathsf{c}},\, \hat{\boldsymbol{F}}^{\mathsf{c}}\right) = \sum_{n=1}^{N} \log \pi_{\hat{\eta}} \left[\boldsymbol{R}\left(\boldsymbol{q}\right) \hat{\vec{f}}_n^{\mathsf{c}} + \vec{t} - \mathcal{C}\left(\boldsymbol{R}\left(\boldsymbol{q}\right) \hat{\vec{f}}_n^{\mathsf{c}} + \vec{t},\, \boldsymbol{E}^{\mathsf{c}}\right)\right]. \quad (2.59)$$

Utilising the log-likelihood, the target distributions of the parameters $\boldsymbol{p}$, $\vec{s}$ and $\boldsymbol{q}$, $\vec{t}$ given the observation, are sampled using a Metropolis algorithm on eq. (2.58) and eq. (2.59), respectively. Metropolis algorithms draw samples from an unknown distribution using samples from a known distribution, which is referred to as proposal distribution. The original Metropolis algorithm uses a fix proposal distribution. However, the convergence rate of the sample, to the desired unknown distribution, depends on the choice of the proposal distribution. The adaptive Metropolis algorithm updates the proposal distribution by optimising the convergence using information from the sample chain at the current state. Haario, Saksman, and Tamminen (2001) used a Gaussian kernel proposal distribution with zero mean, hence only the proposal covariance needed updating. An adaptive update scaling of the covariance of $2.4^2/d$ was used, following Haario, Laine, et al. (2006), with the dimensionality of the parameter-space $d = 6$. The algorithm is non-Markovian but it has correct ergodic properties according to Haario, Saksman, and Tamminen (2001). During parameter sampling, the adaptation of the Metropolis algorithm was performed for each step. Before sampling, the rotation parameters were scaled by $2R = 200\,\mathrm{mm}$ to homogenise the parameter space. The initial proposal variance was set to $(5\,\mathrm{mm})^2$ for the *MEG-to-head* parameters and to $(0.5\,\mathrm{mm})^2$ for the *head-to-MRI* parameters based on prior experience. I performed 10^5 Metropolis algorithm iterations of the *MEG-to-head* and $500 \times N$ iterations of the *head-to-MRI* coregistrations, where N is the number of head shape points. A burn in sample size of 1 000 was used for both *MEG-to-head* and *head-to-MRI*. The Metropolis sampling was implemented using the software library of Parno, Davis, and Conrad (2017). Since the adaptive Metropolis algorithm has correct ergodic properties, integral expressions over functions of the probability density of the parameters like the mean and the variance can be estimated by the respective expressions of sums over the functions on the sample. Since the mean of the rotation parameters does not represent the mean rotation in general, I decided to provide the sample MLE instead of the mean. In the expression of the variance of a parameter x, the mean is replaced by the sample

MLE accordingly as

$$\int_{-\infty}^{\infty} \rho\,(x)\,(x - x_{MLE})^2\,\mathrm{d}x \approx \frac{1}{N}\sum_{n=1}^{N}(x_n - \hat{x}_{MLE})^2$$

$$\mathrm{spread}\,(x) = \sqrt{\frac{1}{N}\sum_{n=1}^{N}(x_n - \hat{x}_{MLE})^2}\,, \tag{2.60}$$

where ρ is the probability density and N is the sample size. Throughout this thesis, the measure in eq. (2.60) is referred to as 'spread'.

2.11 MEG-to-MRI

In the previous section, I referred to the centred and pre-registered problems for each of the two coregistrations (*MEG-to-head* and *head-to-MRI*) separately. These centrings introduce a systematic shift between the translation parameters in the coordinate systems of both coregistrations. However, taking this into account is straightforward. One has to add the mean point $\bar{\vec{b}}$ of the first, and to subtract the mean point $\bar{\vec{d}}$ of the second coregistration, that is, de-centring after the first and re-centring before the second transformation. Consequently, the chained coregistration of a point $\vec{a}^{\,\mathsf{MEG}}$ based on the *MEG-to-head* and *head-to-MRI*, as computed by the Metropolis algorithm, can be written as:

$$\vec{a}^{\,\mathsf{MRI}}_{k,\,l} = \boldsymbol{R}\,(\boldsymbol{q}_l)\cdot\left(\boldsymbol{R}\,(\boldsymbol{p}_k)\,\vec{a}^{\,\mathsf{MEG}} + \vec{s}_k + \bar{\vec{b}} - \bar{\vec{d}}\right) + \vec{t}_l \tag{2.61}$$

$$\vec{a}^{\,\mathsf{MRI}}_{\mathsf{MLE}} = \boldsymbol{R}\,(\boldsymbol{q}_{\mathsf{MLE}})\cdot\left(\boldsymbol{R}\,(\boldsymbol{p}_{\mathsf{MLE}})\,\vec{a}^{\,\mathsf{MEG}} + \vec{s}_{\mathsf{MLE}} + \bar{\vec{b}} - \bar{\vec{d}}\right) + \vec{t}_{\mathsf{MLE}}\,, \tag{2.62}$$

where $\cdot_{\mathsf{MLE}}$ is the maximum likelihood estimate of the parameter from the Metropolis algorithm. The indices k and l in eq. (2.61) refer to the k-th and l-th subsample of *MEG-to-head* and *head-to-MRI* Metropolis samples, respectively. For random sampling, k and l are drawn from the discrete uniform distribution of natural numbers between 1 and the corresponding Metropolis sample size. Apart from the additional indexing, the notation is adopted from eq. (2.5) and eq. (2.16), respectively (fig. 2.1). I defined TRE $\vec{\psi}$ for the point $\vec{a}^{\,\mathsf{MEG}}$ by

$$\vec{\psi}\left(\vec{a}^{\,\mathsf{MEG}} \mid \boldsymbol{p}_k,\,\boldsymbol{q}_l,\,\vec{s}_k,\,\vec{t}_l\right) = \vec{a}^{\,\mathsf{MRI}}_{k,\,l} - \vec{a}^{\,\mathsf{MRI}}_{\mathsf{MLE}}\,. \tag{2.63}$$

The RMS of TRE, defined by

$$\mathrm{RMS}\,(\boldsymbol{\Psi}) = \sqrt{\frac{1}{G}\sum_{g=1}^{G}|\vec{\psi}_g|^2}\,, \tag{2.64}$$

was used as a quality measure based on TRE at a specified point grid of size G. Statistics of $\vec{\psi}$ and $\mathrm{RMS}\,(\boldsymbol{\Psi})$ were estimated by computation of eq. (2.63) and eq. (2.64) for a large number of subsamples $\{\boldsymbol{p}_k,\, \vec{s}_k\}$ and $\left\{\boldsymbol{q}_l,\, \vec{t}_l\right\}$.

Chapter 3

Uncertainty and sensitivity analysis

3.1 Introduction

In the previous chapter, I proposed a method for assessing the quality of coregistrations. This method is also used to assess the distribution of coregistration uncertainties. Figure 3.1 depicts a typical MEG setup where the sensors are aligned with a head model for estimation of brain activity from sensor data.

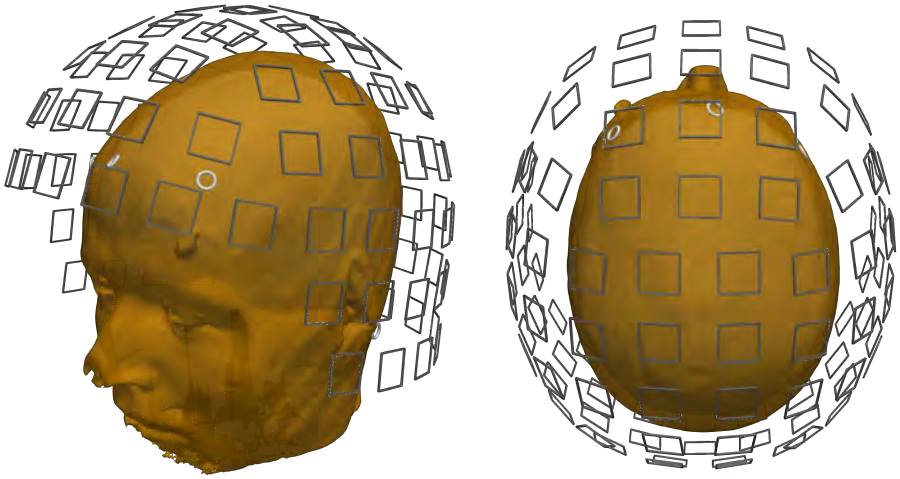

(a) (b)

Figure 3.1: The coregistration setup for one subject shown from two viewpoints (a) and (b). Grey square shapes depict the magnetometers and white tori represent the localization coil positions and orientations. The head surface, as extracted from MRI, is rendered in beige.

Estimates of brain activity are also referred to as source estimates and their accuracy depends on the coregistration of sensors and the head model. In this chapter, a method is described to investigate the propagation of coregistration uncertainties to source estimates. To this end, the method of stochastic spectral approximations is introduced for the general propagation of input uncertainties to the output of computations in section 3.2. In section 3.4 a method is proposed which transforms Gaussian coregistration uncertainties in a way that stochastic spectral methods can be applied. The subsequent section 3.5 describes the simulation of magnetic fields from sources in predefined brain areas which is used later in this thesis. Stochastic spectral methods are applied to the simulation of magnetic fields for a simplified case of coregistration uncertainties. Section 3.6 is based on the simulation of magnetic fields and two methods of source estimation, namely the linearly constrained minimum variance (LCMV) beamformer and the standardized low resolution brain electromagnetic tomography (sLORETA) are introduced. For different test cases of source estimates, stochastic spectral methods are applied and coregistration uncertainties are propagated to beamformer and sLORETA results.

3.2 Stochastic spectral methods

3.2.1 Representation of random processes on polynomial basis

Stochastic spectral methods expand a function $f(\boldsymbol{x})$ using orthogonal polynomials of random input variables. In the following, the expansion is described for the univariate input space and later generalized to multivariate expansions. A univariate orthogonal polynomial space with respect to the measure $\rho(x)$ in Ω is spanned from a set of polynomials ψ_m satisfying the orthogonality conditions

$$\langle \psi_m, \psi_n \rangle = \langle \psi_m, \psi_m \rangle \cdot \delta_{mn} \,, \tag{3.1}$$

where δ_{mn} is the Kronecker delta and the inner product $\langle \cdot, \cdot \rangle$ is defined as

$$\langle \psi_m, \psi_n \rangle = \int_\Omega \psi_m(x)\, \psi_n(x)\, \rho(x)\, \mathrm{d}x \tag{3.2}$$

(Xiu and Karniadakis, 2002; Xiu, 2009). Here, the weighting function $\rho(x)$ is a probability density function. The unknown transfer function $f(x)$ is expressed on

the basis of ψ_p by the polynomial expansion

$$f(x) = \sum_{p=0}^{\infty} c_p \psi_p(x) \ , \tag{3.3}$$

where p is the polynomial order of ψ_p. For example, f can be the magnetic field at a sensor or brain activity at a point in the source space and x can be a shift or rotation of the human head relative to the sensors. In practice, where $f(x)$ describes a real physical system, the contribution of the terms in eq. (3.3) is decreasing with higher orders which allows to truncate the polynomial series at a finite polynomial order. In this thesis, a truncated series of f up to the order P is denoted by $\hat{f}$:

$$f(x) \approx \hat{f}(x) = \sum_{p=0}^{P} c_p \psi_p(x) \ . \tag{3.4}$$

Xiu and Karniadakis (2002) have shown, that the statistical moments of such an expansion converge to the real moments of any random function with finite second-order moments. However, they further demonstrate that the convergence rate of the expansion eq. (3.4) is optimal, in fact it is exponential, when the weighting function $\rho(x)$ of the polynomial basis is equal to the probability density function of the random variable x. Subsets of polynomials in the Askey-scheme were found to form an orthogonal polynomial basis with respect to probability density functions of well known probability distributions (Xiu and Karniadakis, 2002; Xiu, 2009), for example,

- Hermite polynomials: Gaussian distribution
- Laguerre polynomials: Gamma distribution
- Jacobi polynomials: Beta distribution
- Legendre polynomials: Uniform distribution.

This association of polynomials with certain probability distributions allows to expand each random input variable on the basis of an optimal orthogonal polynomial set. In this thesis, only Gaussian input variables are considered and hence, the polynomials ψ_m are probabilists' Hermite polynomials:

$$\langle \psi_m, \psi_n \rangle = \frac{1}{\sqrt{2\pi}} \int_{-\infty}^{\infty} \psi_m(x) \, \psi_n(x) \, e^{\frac{-x^2}{2}} \, \mathrm{d}x = n! \cdot \delta_{mn} \, . \tag{3.5}$$

It is straightforward to generalize the concept above to the K-variate random input vector $\boldsymbol{x} = (x_1, x_2, \ldots, x_K)$ with K independent components. The joint probability density function of $\boldsymbol{x}$ is then

$$\rho(\boldsymbol{x}) = \prod_{k=1}^{K} \rho_k(x_k) \,, \tag{3.6}$$

where $\rho_k(x_k)$ is the probability density of the k-th input variable. According to this, the K-variate orthogonal polynomials $\psi_m(\boldsymbol{x})$ are constructed as products of univariate polynomials in each variable:

$$\Psi_{\boldsymbol{m}}(\boldsymbol{x}) = \psi_{m_1}(x_1) \cdot \psi_{m_2}(x_2) \cdots \psi_{m_K}(x_K) \,,\ \{m_1, m_2, \ldots, m_K\} = \boldsymbol{m} \in \mathcal{M} \,, \tag{3.7}$$

where m_k is the order of polynomial $\psi_{m_k}(x_k)$ and $\boldsymbol{m}$ is a multi-index of the multi-index set $\mathcal{M} \subset \mathbb{N}_0^K$. Analogue to the univariate case, the orthogonality holds as:

$$\begin{aligned} \langle \Psi_{\boldsymbol{m}}, \Psi_{\boldsymbol{n}} \rangle &= \langle \Psi_{\boldsymbol{m}}, \Psi_{\boldsymbol{m}} \rangle \cdot \prod_{k=1}^{K} \delta_{m_k\, n_k} \\ \langle \Psi_{\boldsymbol{m}}, \Psi_{\boldsymbol{n}} \rangle &= \int_{\Omega} \Psi_{\boldsymbol{m}}(\boldsymbol{x})\, \Psi_{\boldsymbol{n}}(\boldsymbol{x})\, \rho(\boldsymbol{x})\, \mathrm{d}\boldsymbol{x} \,, \end{aligned} \tag{3.8}$$

where Ω is the support of the random variables $\boldsymbol{x}$ The definition of $\mathcal{M}$ is critical since it determines the number of basis polynomials. A possible choice for $\mathcal{M}$ are full tensor index sets, where all combinations of polynomial orders up to P are employed in each random variable. This choice is not desirable for practical computations as the number of basis polynomials is $(P+1)^N$ and increases too much for large K (Xiu, 2009). An alternative are total order multi-index sets, which limit the sum of polynomial orders over all variables:

$$\mathcal{M}_P := \left\{ \boldsymbol{m} \in \mathbb{N}_0^K : |\boldsymbol{m}|_1 = \sum_{k=1}^{K} m_k \leq P \right\} . \tag{3.9}$$

The number of basis polynomials associated with total order sets $\mathcal{M}_P$ can be expressed as the binomial coefficient $\binom{K+P}{K}$. Total order sets are used in most computations with stochastic spectral methods (Xiu, 2009). For this thesis, a variant of total order sets is used, which is tailored to Gaussian numerical integration and it is described in detail in section 3.2.2.

3.2.2 Smolyak pseudospectral approximation method

Introduction

The analytic solution of spectral expansion coefficients can be expressed by the integral

$$c_{\boldsymbol{m}} = \frac{1}{\langle \Psi_{\boldsymbol{m}},\, \Psi_{\boldsymbol{m}} \rangle} \int_{\Omega} f(\boldsymbol{x})\, \Psi_{\boldsymbol{m}}(\boldsymbol{x})\, \rho(\boldsymbol{x})\, \mathrm{d}\boldsymbol{x}\,. \tag{3.10}$$

In almost all practical cases, however, it is not possible to find an analytic solution of this integral. An alternative are non-intrusive approaches, which do not depend on the governing equations and instead treat a simulator as a black box. One of these approaches is the pseudospectral approximation method where the integral in eq. (3.10) is computed numerically and hence, the function $f(\boldsymbol{x})$ is only evaluated at a finite number of quadrature nodes. For numerical integration schemes, let

$$Q_N \rho \circ y = \sum_{n=1}^{N} w_n \cdot y(x_n) \approx \int_{\Omega_\rho} y(x) \cdot \rho(x)\, \mathrm{d}x \tag{3.11}$$

be the univariate quadrature of a function y with weighting ρ, where N is the number of nodes, w_n and x_n are the weights and nodes, respectively. Both w_n and x_n depend on N and ρ. A rule $Q_N \rho$ is referred to as Gaussian quadrature when the integral is solved exactly for polynomials of degree $M = 2N - 1$ or less. In other words $\sum_{n=1}^{N} w_n \cdot y(x_n) = \int_{\Omega_g} y(x) \cdot \rho(x)\, \mathrm{d}x$, when y is a sum of polynomials up to the order $2N - 1$. Dependent on the weighting, different terms are associated to quadrature rules, for example Gauss-Legendre and Gauss-Hermite quadrature for uniform or normal distribution weighting, respectively. Here, Gauss-Hermite quadrature is used because it is optimal for *normal* inputs (as decribed in section 3.2.1). The nodes of a univariate Gaussian quadrature Q_N are the roots of the associated order N polynomial. A multivariate quadrature in K variables, which is exact for all products of univariate polynomials up the orders $2N_1 - 1, \ldots, 2N_K - 1$ can be computed by full tensor products $\otimes$ of univariate rules as

$$\begin{aligned} Q_{\boldsymbol{N}\,\boldsymbol{\rho}} \circ y &= \sum_{n_1=1}^{N_1} \cdots \sum_{n_K=1}^{N_K} w_{n_1} \cdots w_{n_K} \cdot y(x_{n_1},\, \ldots,\, x_{n_K}) \\ &= [Q_{N_1\,\rho_1} \otimes \cdots \otimes Q_{N_K\,\rho_K}] \circ y \end{aligned} \tag{3.12}$$

So far the exactness of integrating $y(x) \cdot \rho(x)$ was considered for polynomial y. The integrand in pseudospectral approximations, however, is $f(\boldsymbol{x})\, \Psi_{\boldsymbol{m}}(\boldsymbol{x})\, \rho(\boldsymbol{x})$ and it is of greater interest here. Again, $f(\boldsymbol{x})\, \Psi_{\boldsymbol{m}}(\boldsymbol{x})$ is considered as a polynom. In the ideal

case, where f and the polynomial basis have the same maximal polynomial order, a quadrature rule is exact for transfer functions f up to the orders $N_1, \ldots, N_K$ when it is exact for polynomial orders $2N_1, \ldots, 2N_K$. Hence, the set of polynomial orders up to $N_1, \ldots, N_K$ is also referred to as half-exact set of a quadrature rule. Figure 3.2 depicts the polynomial orders (a) of two variables, which can be exactly integrated by the full tensor nodes (b).

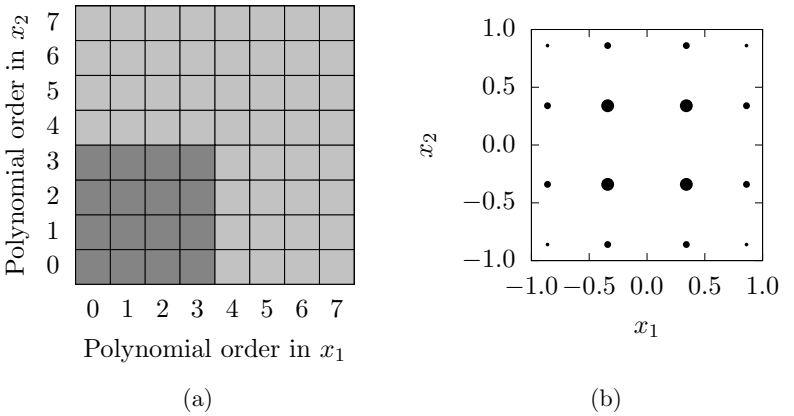

Figure 3.2: Exact (light grey) and half-exact (dark grey) sets of polynomial orders are depicted for a full tensor quadrature in (a). In (b), the corresponding quadrature nodes are plotted.

This example shows 4×4 nodes which are needed to exactly integrate all polynomial products of orders up to 7,7. Let $f(x)$ be a polynomial of order M, then the highest order integrand of an exact polynomial expansion of f is $f(x)\,\psi_M(x)\,\rho(x)$, which is of polynomial order $2M$. For Gaussian quadrature rules, $M+1$ nodes are sufficient to exactly expand f. In this example, $\{0, \ldots, M\}$ is the half-exact set of the quadrature rule with $M+1$ nodes. This concept is generalized to the multivariate case and the half-exact set of the quadrature rule in fig. 3.2 is depicted by dark grey squares in (a). The quadrature in fig. 3.2 is able to exactly expand a polynomial function in two variables of orders up to 3, 3 in the transfer function f.

Smolyak quadrature

In the previous section, the basics of pseudospectral approximations and full tensor quadrature were introduced. A problem with full tensor quadrature is the exponential increase of quadrature nodes and hence, numerical computations, when the number of input variables increases (curse of dimensionality). Smolyak algorithms

help to reduce the cost by omitting the coupling of higher order quadrature in different variables. Conrad and Marzouk (2013) motivated this approach by the following example. They consider the function $f(x_1, x_2) = x_1^7 + x_2^7 + x_1^3 x_2$. A full tensor pseudospectral expansion would estimate all polynomial coefficients up the orders $x_1^7 x_2^7$ and hence requiring 8×8 nodes of a Gaussian quadrature. However, in this particular case, an exact expansion of f can be constructed more efficiently by 8×1, 1×8 and 4×2 nodes. Smolyak algorithms make use of this approach since in case of the presented spectral projection approach, the polynomial basis is known (Conrad and Marzouk, 2013). For K inputs, Smolyak algorithms work for so-called admissible multi-index sets. Here, a multi-index $\boldsymbol{s} \in \mathbb{N}_0^K$ refers to quadrature levels in each input. An increment in the quadrature level is related to an increment in the number of quadrature nodes. The backward neighborhood of a multi-index $\boldsymbol{s}$ is defined as the multi-index set

$$n_b(\boldsymbol{s}) := \left\{ \boldsymbol{s} - \boldsymbol{u}_k : \forall k \in \{1 \dots K\}, \, \boldsymbol{s} - \boldsymbol{u}_k \in \mathbb{N}_0^K \right\} . \tag{3.13}$$

A multi-index set $\mathcal{S}$ is admissible if and only if for all multi-indices in $\mathcal{S}$, the backward neighborhood is a subset of $\mathcal{S}$:

$$\forall \boldsymbol{s} \in \mathcal{S}, \, n_b(\boldsymbol{s}) \subseteq \mathcal{S} . \tag{3.14}$$

Examples of admissible multi-index sets are total order multi-index sets

$$\mathcal{S}_N := \left\{ \boldsymbol{s} \in \mathbb{N}_0^K : |\boldsymbol{s}|_1 \leq N \right\} , \tag{3.15}$$

where the sum of quadrature levels over all inputs is limited to N. Total order multi-index sets are the most widely studied choice and suggested by Smolyak (Conrad and Marzouk, 2013). The Smolyak algorithm defines the difference operators for a set $\mathcal{Q}$ of univariate quadrature levels s as

$$\Delta_{k\,0}(\mathcal{Q}) := Q_{N_k(0)\,\rho_k} = 0 \tag{3.16}$$

$$\Delta_{k\,s}(\mathcal{Q}) := Q_{N_k(s)\,\rho_k} - Q_{N_k(s-1)\,\rho_k}, \, s \in \mathbb{N}_1 , \tag{3.17}$$

where $Q_{N_k(s)\,\rho_k}$ is a univariate quadrature for input k with weighting ρ_k and $N_k(s)$ nodes. Let $\mathcal{E}_k(s)$ be the exact set of a univariate quadrature $Q_{N_k(s)\,\rho_k}$. Conrad and

Marzouk (2013) have proven, that the multivariate Smolyak quadrature

$$\begin{aligned} A\left(\mathcal{Q}, \mathcal{S}\right) \circ f &= \sum_{\boldsymbol{s} \in \mathcal{S}} \left[\Delta_{1\, s_1}\left(\mathcal{Q}\right) \otimes \cdots \otimes \Delta_{K\, s_K}\left(\mathcal{Q}\right)\right] \circ f \\ &= \sum_{\boldsymbol{s} \in \mathcal{S}} c_{\boldsymbol{s}} \left[Q_{N_1(s_1)\, \rho_1} \otimes \cdots \otimes Q_{N_K(s_K)\, \rho_K}\right] \circ f \end{aligned} \tag{3.18}$$

is exact for all polynomial orders in

$$\mathcal{E}\left(A\left(\mathcal{Q}, \mathcal{S}\right)\right) \supseteq \bigcup_{\boldsymbol{s} \in \mathcal{S}} \mathcal{E}_1\left(s_1\right) \otimes \cdots \otimes \mathcal{E}_K\left(s_K\right) . \tag{3.19}$$

The $c_{\boldsymbol{s}}$ in eq. (3.18) are integer coefficients, resulting from a rearrangement of the difference operators. The exactness relation of eq. (3.19) holds for quadrature rules with nested exactness. That is, univariate quadrature rules with N_k nodes must include the exact set of their rules with less nodes. This condition is fulfilled for most quadrature rules, for example for Gaussian quadrature which is used here. A total order multi-index set in two dimensions up to the total level of 4

$$\mathcal{S}_4 := \left\{\boldsymbol{s} \in \mathbb{N}_0^2 : |\boldsymbol{s}|_1 \leq 4\right\} , \tag{3.20}$$

combined with a simple linear growth of nodes $N_k = s$ and Gaussian quadrature ($\mathcal{E}_k\left(s\right) = 2s - 1$) has an exact set as depicted in fig. 3.3 (a).

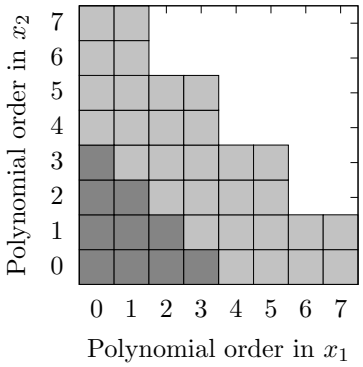

(a) level 2, linear growth

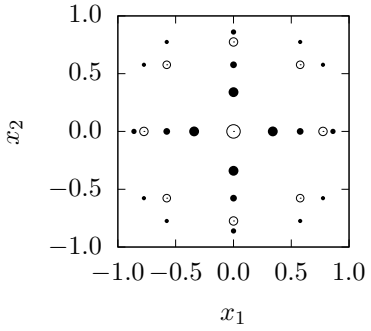

(b) nodes and weights

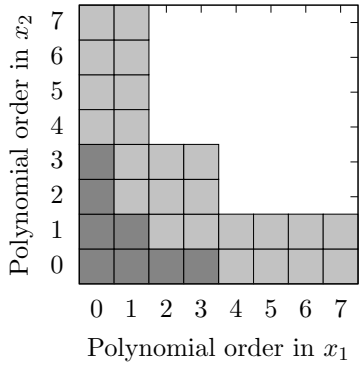

(c) level 2, exponential growth

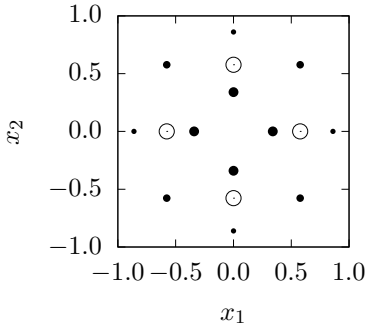

(d) nodes and weights

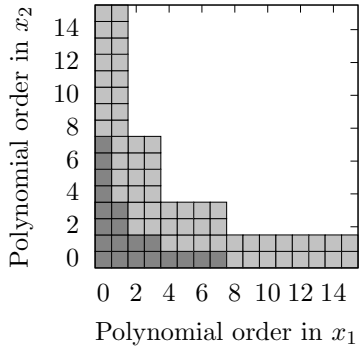

(e) level 3, exponential growth

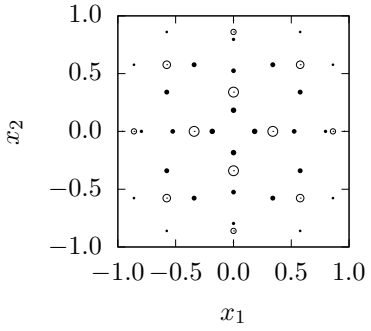

(f) nodes and weights

Figure 3.3: The graphs depict polynomial exactness, nodes and weights of Gauss-Legendre quadrature rules. Exact (light grey) and half-exact (dark grey) sets of polynomial orders are depicted for different total order level sets and growth rules in the left graphs (a), (c) and (e). On the right side (b), (d) and (f), the corresponding quadrature nodes and weights are plotted. Black dots and circles represent positive and negative weights, respectively. The size of the markers scales with the absolute weight values.

The quadrature nodes for this example are plotted in fig. 3.3 (b). Similar examples are depicted in fig. 3.3 (c), (d) and (e), (f) for an exponential growth of nodes $N_k = 2^{s-1}\,, s \geq 1$ and total levels of $|\boldsymbol{s}|_1 \leq 3$ and $|\boldsymbol{s}|_1 \leq 4$, respectively.

Smolyak pseudospectral approximation

In this section, the Smolyak algorithm from above is applied to estimate the coefficients of pseudospectral approximations. The Smolyak algorithm from section 3.2.2 can be transferred directly from univariate quadrature rules to pseudospectral approximations. The pseudospectral approximations in dimension k are defined as

$$P_{k\,s} \circ f := \sum_{l=0}^{q_k(s)} \left[\frac{1}{\langle \psi_l,\, \psi_l \rangle} Q_{N_k(s)\,\rho_k} \circ (f \psi_l) \right] \psi_l\,(x)\ , \tag{3.21}$$

where $q_k\,(s)$ is the polynomial truncation. Here, a polynomial truncation of $q_k\,(s) = \text{floor}\,((2N_k\,(s) - 1)\,/2) = N_k\,(s) - 1$ is used for Gaussian quadrature rules. Such a truncation guarantees polynomial accuracy and avoids internal aliasing (Conrad and Marzouk, 2013). Internal aliasing is an erroneous estimation of nonzero polynomial coefficients for a function within the polynomial range of the pseudospectral approximation. The Smolyak pseudospectral approximation of a function f is defined as

$$A\,(\mathcal{P},\, \mathcal{S}) \circ f = \sum_{\boldsymbol{s} \in \mathcal{S}} c_{\boldsymbol{s}} P_{\boldsymbol{s}}\,(f)\ , \tag{3.22}$$

which is constructed exactly like the Smolyak quadrature of eq. (3.18) with $\mathcal{Q}$ substituted for $\mathcal{P}$. That is, quadrature rules are substituted for pseudospectral approximations. The differential operators of pseudospectral approximations are

$$\Delta_{k\,0}\,(\mathcal{P}) := 0 \tag{3.23}$$

$$\Delta_{k\,s}\,(\mathcal{P}) := P_{k\,s} - P_{k\,(s-1)},\ s \in \mathbb{N}_1 \tag{3.24}$$

and $P_{\boldsymbol{s}}$ are full tensor approximations built around the polynomial accuracy of single full tensor quadrature rules (Conrad and Marzouk, 2013). The half-exact set of a Smolyak quadrature defines the polynomial range of the corresponding Smolyak pseudospectral approximation. A Smolyak pseudospectral approximation is exact for functions which can be expressed as a sum of polynomials within the polynomial range of the approximation. Hence, Smolyak pseudospectral approximations have no internal aliasing (Conrad and Marzouk, 2013). For example, in the figures 3.3

the Smolyak pseudospectral approximations based on the nodes in the right graphs are exact for the corresponding polynomial orders in dark grey in the left graphs.

Smolyak pseudospectral approximation example

The principles of Smolyak pseudospectral approximations are demonstrated on a simple example. Let the function of interest be $f(x_1, x_2) = 2\cos x_1 + 3\sin x_2 - 1$. The inputs x_1 and x_2 are independent random variables following a *normal* distribution with zero mean and unit variance. Hence, Gauss-Hermite quadrature rules are used in the following. For the approximation, a total order Smolyak level set $\mathcal{S}$ with maximum order of 1 and the quadrature growth rule $N(0) = 1$, $N(1) = 5$ is chosen. That is, $\mathcal{S} = \{\{0, 0\}, \{0, 1\}, \{1, 0\}\}$ and three quadrature rules, one with one node and two with five nodes each, are assigned. Again a polynomial truncation of $q_k(s) = N(s) - 1$ is used. That is a maximal polynomial order of 4 in each variable. The set of basis polynomials $\{\Psi_{0,0}, \Psi_{1,0} \ldots, \Psi_{0,4}\}$, here 9 Hermite polynom products, reads

$$\begin{aligned}
\Psi_{0,0} &= \psi_0(x_1)\,\psi_0(x_2) = 1 \\
\Psi_{1,0} &= \psi_1(x_1)\,\psi_0(x_2) = x_1 \\
\Psi_{2,0} &= \psi_2(x_1)\,\psi_0(x_2) = x_1^2 - 1 \\
\Psi_{3,0} &= \psi_3(x_1)\,\psi_0(x_2) = x_1^3 - 3x_1 \\
\Psi_{4,0} &= \psi_4(x_1)\,\psi_0(x_2) = x_1^4 - 6x_1^2 + 3 \\
&\vdots \\
\Psi_{0,4} &= \psi_0(x_1)\,\psi_4(x_2) = x_2^4 - 6x_2^2 + 3\,.
\end{aligned} \tag{3.25}$$

From the Smolyak level set, the quadrature rules and the polynomial set, the Smolyak algorithm defines the sum over the differential approximations as

$$A(\mathcal{P}, \mathcal{S}) \circ f = \sum_{\boldsymbol{s} \in \mathcal{S}} \Delta_{1\,s_1} \otimes \Delta_{2\,s_2}\,, \tag{3.26}$$

which reads in this example as

$$\begin{aligned} A\left(\mathcal{P},\,\mathcal{S}\right)\circ f = &+ \underbrace{\sum_{\boldsymbol{s}\in\mathcal{S},\,s_2=0} c_{\boldsymbol{s}}\Psi_{\boldsymbol{s}} - c_{0,\,0}\Psi_{0,\,0}}_{\Delta_{1\,2}\otimes\Delta_{2\,1}} + \\ &+ \underbrace{\sum_{\boldsymbol{s}\in\mathcal{S},\,s_1=0} c_{\boldsymbol{s}}\Psi_{\boldsymbol{s}} - c_{0,\,0}\Psi_{0,\,0}}_{\Delta_{1\,1}\otimes\Delta_{2\,2}} + \\ &+ \underbrace{c_{0,\,0}\Psi_{0,\,0} - 0}_{\Delta_{1\,1}\otimes\Delta_{2\,1}}, \end{aligned} \tag{3.27}$$

where the coefficient $c_{0,\,0}$ is computed from the central node $(0, 0)$. Hence, the Smolyak pseudospectral approximation consists of three differential terms, where each minuend and subtrahend is a pseudospectral approximation in its own right. Figure 3.4 demonstrates the composition of this example in differential terms, where the associated quadrature nodes are marked black.

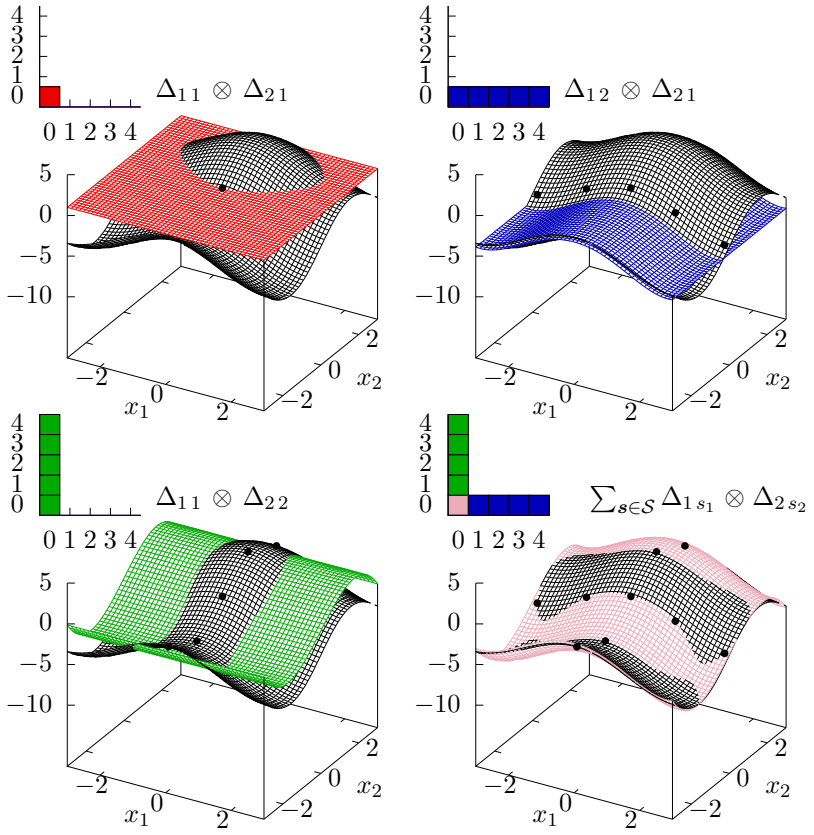

Figure 3.4: Example of a Smolyak pseudospectral approximation of the function $f = 2\cos x_1 + 3\sin x_2 - 1$. *All four graphs depict the function* f *in black. In red, the zero order approximation* ($c_{0,0}$) *estimated from one node is depicted. The differentials of the fourth and zero order approximations are depicted in blue and green for inputs* x_1 *and* x_2, *respectively. In pink, the sum of all three differential terms is depicted, this is the Smolyak pseudospectral approximation of* f. *The black markers represent the quadrature nodes of each term associated to the graphs.*

Choosing quadrature growth rules

Here, only linear growth rules are briefly investigated. Smolyak pseudospectral approximations are built around quadrature sets with certain growth rules. The growth rules determine the number of quadrature nodes and hence the range of polynomial orders of pseudospectral approximations. It is desirable to reduce the

number of nodes for a given range of polynomial orders. Burkardt and Webster (2014) proposed a Smolyak quadrature where only odd numbers of nodes are used. They do this by lifting each even number rule up to the next odd rule, this does not contradict with the Smolyak algorithm and it is efficient since odd rules usually share the midpoint node and the same nodes are used for two polynomial orders. I followed this idea and used the growth rule $N(s) = 2s + 1$ for my Smolyak pseudospectral approximations, where N is the number of nodes and s is the Smolyak level. Conrad and Marzouk (2013) also recommended to add at least two nodes for each new level in adaptive strategies (adaptive approximations are introduced in the next section). Here, a total order multi-index set up to the level of 3 is used and with the growth rule from above, the polynomial order range $\mathcal{M}$ is defined as

$$\begin{aligned} \mathcal{M}' &:= \left\{ \{2s_1, \ldots, 2s_K\} \in \mathbb{N}_0^K : |\boldsymbol{s}|_1 \leq 3 \right\} \\ \mathcal{M} &:= \left\{ n_b(\boldsymbol{m}) : \forall \boldsymbol{m} \in \mathcal{M}' \right\} \cup \mathcal{M}', \end{aligned} \tag{3.28}$$

which is the half-exact set of the associated Smolyak quadrature. $n_b(\boldsymbol{m})$ is the backward neighbourhood of $\boldsymbol{m}$ as defined in eq. (3.13).

Adaptive Smolyak pseudospectral approximation

So far, pseudospectral approximations were discussed for fixed multi-index sets. In practise, often the convergence of such approximations cannot be estimated prior to the evaluation of the function of interest. Hence it is desirable to adapt to a function and refine an approximation in subspaces, where the error is large. Conrad and Marzouk (2013) analyzed Smolyak multi-index sets and derived an error measure for terms which can be refined. Let $\mathcal{S}$ be the current multi-index set, A multi-index $\boldsymbol{s} \in \mathcal{S}$ can be refined if it has at least one admissible forward neighbour. The admissible forward neighbourhood of $\boldsymbol{s}$ is the set of forward neighbours of $\boldsymbol{s}$ which are not contained in $\mathcal{S}$ and which form again an admissible multi-index set if added to $\mathcal{S}$:

$$n_{af}(\boldsymbol{s}) := \left\{ \boldsymbol{n} \in \mathbb{N}_1^K \setminus \mathcal{S} : \boldsymbol{s} \in n_b(\boldsymbol{n}),\, n_b(\boldsymbol{s}) \subseteq \mathcal{S} \right\}. \tag{3.29}$$

Let $\boldsymbol{s}$ be a multi-index with admissible forward neighbours and

$$\mathcal{M} := \mathcal{M}' \cup \{\boldsymbol{s}\}, \tag{3.30}$$

where $\mathcal{M}$ and $\mathcal{M}'$ are admissible. Conrad and Marzouk (2013) assume that whenever $\boldsymbol{s}$ changes the Smolyak approximation strongly, it probably represents a subspace which needs further refinement. They estimate the change of Smolyak approxima-

tions due to adding $\boldsymbol{s}$ to $\mathcal{M}'$ by the triangle inequality

$$\epsilon\left(\boldsymbol{s}\right) := \left| \left[\Delta_{1\,s_1}\left(\mathcal{P}\right) \otimes \cdots \otimes \Delta_{K\,s_K}\left(\mathcal{P}\right)\right] \circ f \right|_2 \geq \left| A\left(\mathcal{P},\, \mathcal{M}\right) \circ f - A\left(\mathcal{P},\, \mathcal{M}'\right) \circ f \right|_2 . \tag{3.31}$$

Their local error estimate $\epsilon\left(\boldsymbol{s}\right)$ is efficient since it does not change as $\mathcal{M}'$ evolves and hence needs to be computed only once for each $\boldsymbol{s}$ (Conrad and Marzouk, 2013). The set of multi-indices in $\mathcal{S}$ with at least one admissible forward neighbour can be defined as

$$\mathcal{K} := \left\{ \boldsymbol{s} \in n_b\left(\boldsymbol{n}\right) : \forall \boldsymbol{n} \in \mathbb{N}_1^K \setminus \mathcal{S},\, n_b\left(\boldsymbol{n}\right) \subseteq \mathcal{S} \right\} . \tag{3.32}$$

At each adaptation, $\boldsymbol{s} \in \mathcal{K}$ is found that maximises $\epsilon\left(\boldsymbol{s}\right)$ and the admissible forward neighbours of $\boldsymbol{s}$ are added (Conrad and Marzouk, 2013). As a termination criterion, they proposed the global error indicator

$$\epsilon_g = \sum_{\boldsymbol{s} \in \mathcal{K}} \epsilon\left(\boldsymbol{s}\right) . \tag{3.33}$$

For this thesis, I decided against adaptation for a better comparability between the approximations of different functions. But for other applications, the adaptability is an important feature of Smolyak pseudospectral approximations.

3.2.3 Error estimates of spectral approximations

For the verification of spectral approximations, I define a measure which is closely related to the one described by Weise et al. (2015). Here, the relative error of an approximation $\hat{p}$ of a function $p\left(\boldsymbol{x}\right)$ is defined as

$$\epsilon_{\hat{p}} = \frac{1}{A_\Omega} \int_\Omega \frac{\left| \boldsymbol{p}\left(\vec{r}, \boldsymbol{X}\right) - \hat{\boldsymbol{p}}\left(\vec{r}, \boldsymbol{X}\right) \right|}{\left| \boldsymbol{p}\left(\vec{r}, \boldsymbol{X}\right) - \mathbb{E}\left[\boldsymbol{p}\left(\vec{r}, \boldsymbol{X}\right)\right] \right|} \mathrm{d}\Omega \,, \tag{3.34}$$

where Ω is a region of interest, A_Ω is its area. The vectors $\boldsymbol{p}$ and $\hat{\boldsymbol{p}}$ are reference solutions and its approximations for an input sample $\boldsymbol{X} = \left(\boldsymbol{x}_1, \ldots, \boldsymbol{x}_N\right)$, respectively. $\mathbb{E}\left[\boldsymbol{p}\left(\vec{r}, \boldsymbol{X}\right)\right]$ denotes the mean reference solution over N samples at location $\vec{r}$. In this thesis, the region of interest is defined by a discrete set of sources, the source locations $\vec{r}$, and hence the integral in eq. (3.34) is approximated by the sum over this set and the area by the number of sources. A disadvantage of this error computation is that additional N evaluations of $p\left(\boldsymbol{x}\right)$ are required (Weise et al., 2015).

3.2.4 Statistics from polynomial coefficients

From a stochastic spectral approximation $f(\boldsymbol{x}) \approx \hat{f}(\boldsymbol{x}) = \sum_{\boldsymbol{s}\in\mathcal{S}} \hat{f}_{\boldsymbol{s}} \Psi_{\boldsymbol{s}}(\boldsymbol{x})$, the first two moments of the output distribution of $f(\boldsymbol{x})$ can be approximated in closed form according to

$$\mathbb{E}[f(\boldsymbol{x})] \approx \mathbb{E}\left[\hat{f}(\boldsymbol{x})\right] = \hat{f}_{\boldsymbol{0}} \tag{3.35}$$

$$\mathrm{Var}[f(\boldsymbol{x})] \approx \mathrm{Var}\left[\hat{f}(\boldsymbol{x})\right] = \mathbb{E}\left[\left(\hat{f}(\boldsymbol{x}) - \mathbb{E}\left[\hat{f}(\boldsymbol{x})\right]\right)^2\right] = \sum_{\boldsymbol{s}\in\mathcal{S}\setminus\boldsymbol{0}} \hat{f}_{\boldsymbol{s}}^2 \langle \Psi_{\boldsymbol{s}}, \Psi_{\boldsymbol{s}} \rangle \tag{3.36}$$

where $\mathbb{E}[f(\boldsymbol{x})]$ is the expected value and $\mathrm{Var}[f(\boldsymbol{x})]$ is the variance of $f(\boldsymbol{x})$ (Xiu, 2009). The above relations follow from the orthogonality of the polynomials $\Psi_{\boldsymbol{s}}(\boldsymbol{x})$ when the polynomial basis is matched with the input distribution of $\boldsymbol{x}$.

3.2.5 Variance based sensitivity analysis

Provided that the input factors are statistically independent, the output variance can be decomposed into first and higher order effects. In such a decomposition, first order effects model the partial output variance due to variations of a single input factor only. The remaining variance, which cannot be explained by first order effects is due to interaction effects of two or more input factors on the output variance. For a scalar function $f(\boldsymbol{x}) = f(x_1, x_2, \ldots, x_K)$ a variance based first order effect for an input factor x_k can be expressed as

$$\mathrm{Var}_{x_k}\left[\mathbb{E}_{\boldsymbol{x}_{\not k}}[f \mid x_k]\right], \tag{3.37}$$

where $\mathrm{Var}_{x_k}[\cdot]$ is the variance computed for all x_k and $\mathbb{E}_{\boldsymbol{x}_{\not k}}[\cdot]$ is the mean computed for all other inputs while keeping x_k fixed (Saltelli et al., 2010). The associated normalized first order sensitivity index is expressed as

$$S_k[f] = \frac{\mathrm{Var}_{x_k}\left[\mathbb{E}_{\boldsymbol{x}_{\not k}}[f \mid x_k]\right]}{\mathrm{Var}[f]}. \tag{3.38}$$

S_k is normalized between zero and one and measures the additive effect of x_k on the model output (Saltelli et al., 2010). In fig. 3.5, the relation between the means and variances is demonstrated on an example function. From a pseudospectral approximation, the sensitivity indices are simply estimated from subsets of the coefficients. Each index $S_k\left[\hat{f}\right]$ is computed from the multi-index set $\mathcal{M}_k$ with non-zero indices

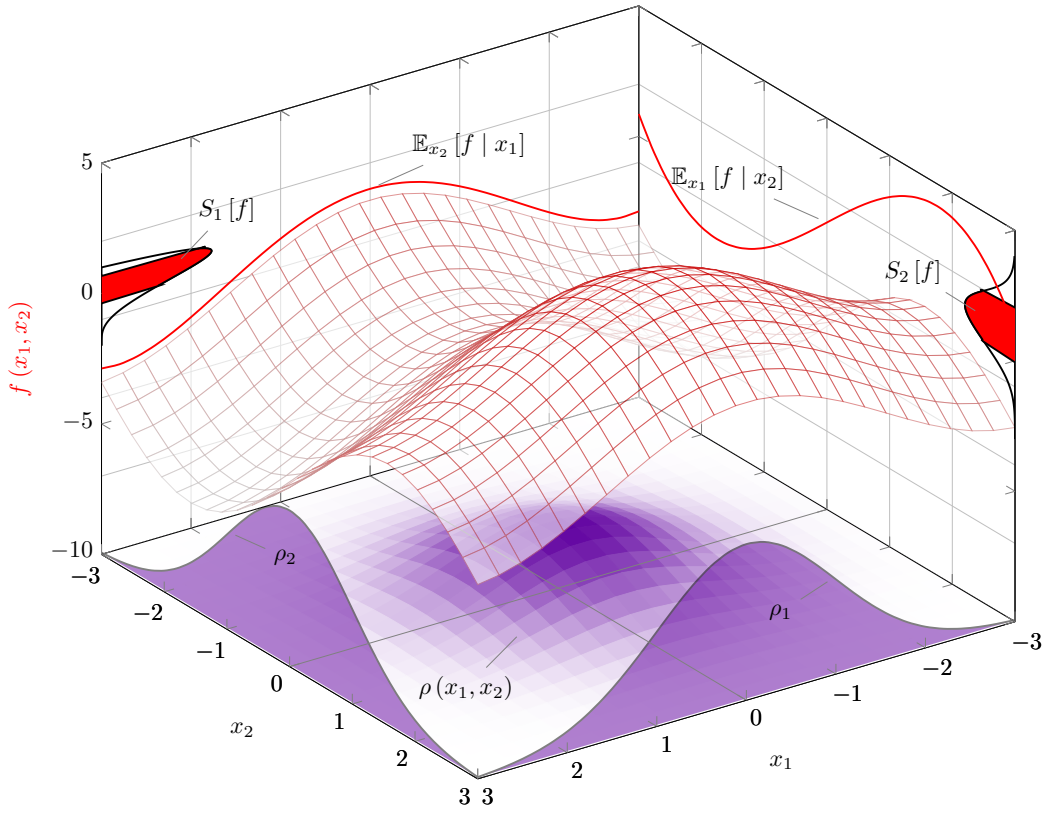

Figure 3.5: First order sensitivity indices are demonstrated on the example function $f(x_1, x_2) = 2\cos x_1 + 3\sin x_2 - 1$. *The probability density of the inputs* $\rho(x_1, x_2) = \rho_1(x_1)\,\rho_2(x_2)$ *is depicted (violet) below the function* f *(red mesh). On the planes* $f, x_1 \mid x_2 = -3$ *and* $f, x_2 \mid x_1 = -3$, *the mean functions* $\mathbb{E}_{x_1} = \mathbb{E}_{\boldsymbol{x}_2}$ *and* $\mathbb{E}_{x_2} = \mathbb{E}_{\boldsymbol{x}_1}$ *are plotted, respectively. The mean functions are computed with respect to the probability density* ρ. *That is, the function values near* $(0, 0)$ *are higher weighted compared to* f *at more distant inputs. From the distributions of the weighted* $\mathbb{E}_{x_1}$ *and* $\mathbb{E}_{x_2}$, *their variances are computed, their standard deviations are depicted by the read areas here. The sensitivity indices are computed from these variances by normalization with the variance of* f.

only for the x_k of interest (Saturnino et al., 2019):

$$S_k\left[\hat{f}\right] = \frac{1}{\mathrm{Var}\left[\hat{f}\left(\boldsymbol{x}\right)\right]} \sum_{\boldsymbol{m}\in\mathcal{M}_k} \hat{f}^2_{\boldsymbol{m}} \langle \Psi_{\boldsymbol{m}},\, \Psi_{\boldsymbol{m}} \rangle\,, \tag{3.39}$$

where $\mathrm{Var}\left[\hat{f}\left(\boldsymbol{x}\right)\right]$ is computed as in eq. (3.36). However, when a nonlinear function g is applied to $\hat{f}$, the sensitivity indices of $g \circ \hat{f}$ cannot be extracted from the polynomial coefficients of $\hat{f}$. For example, when f is a brain activity measure and its pseudospectral approximation is $\hat{f}$, then the maximum location of the brain activity can be estimated by the nonlinear maximum function g applied to $\hat{f}$. Although it is possible to expand $g \circ \hat{f}$, some disadvantages would arise, namely it would be an approximation of an approximation with larger errors and in this example the expansion needs re-computation for different magnetic fields. On the other hand, $\hat{f}$ is already computational efficient and Monte-Carlo sampling would be appropriate. An efficient sampling based approach for sensitivity indices was published by Saltelli et al. (2010). They proposed to estimate $\mathrm{Var}_{x_k}\left[\mathbb{E}_{\boldsymbol{x}_{\not k}}\left[g \circ \hat{f} \mid x_k\right]\right]$ as

$$\frac{1}{N}\sum_{l=1}^{L} g\left(\boldsymbol{A}\right)_l \cdot \left(g\left(\boldsymbol{A}_{\boldsymbol{B}}^{(\mathsf{k})}\right)_l - g\left(\boldsymbol{B}\right)_l\right) \tag{3.40}$$

where $\boldsymbol{A}$ and $\boldsymbol{B}$ are independent sampling matrices of $\hat{f}$ on $\boldsymbol{x}$ with L rows and K columns, K is the number of input factors and L is the number of computations per matrix. The k-th column of matrix $\boldsymbol{A}_{\boldsymbol{B}}^{(\mathsf{k})}$ is equal to the k-th column of $\boldsymbol{B}$ and all other columns of $\boldsymbol{A}_{\boldsymbol{B}}^{(\mathsf{k})}$ are equal to the associated columns of $\boldsymbol{A}$. In eq. (3.40), the notation $g\left(\boldsymbol{A}\right)_l$ refers to the l-th column of the evaluation matrix $g\left(\boldsymbol{A}\right)$. By using eq. (3.40) for all K sensitivity indices, $2L$ evaluations of $g \circ \hat{f}$ are computed from $\boldsymbol{A}$ and $\boldsymbol{B}$ and another $K \cdot L$ from $\boldsymbol{A}_{\boldsymbol{B}}^{(\mathsf{k})}$. In total the cost of the sensitivity indices is $L \cdot (K + 2)$ evaluations of $g \circ \hat{f}$, with L sufficiently large, 500 or higher (Saltelli et al., 2010). For this thesis $L = 10\,000$ is chosen for the estimation of sensitivity indices. The sampling of the input space is performed by Sobol' quasi-random sequences, as proposed by Saltelli (2002) and Saltelli et al. (2010). If it is not possible to extract the sensitivity indices from the polynomial coefficients, the method of Saltelli et al. (2010) is used here.

3.3 Coregistration parameter distribution

The coregistration parameters are derived from the Metropolis sampling and computed in a similar way as the TRE which is described in section 2.11. Metropolis sampling of *head-to-MRI* explicitly draws samples from the *head-to-MRI* coregistration parameter distribution. For *MEG-to-head*, the parameter covariance $\boldsymbol{C}_{\text{MEG-to-head}}$ can be inferred from linearization, as described in section 2.5.1. By assuming normal errors, *MEG-to-head* parameter samples are drawn from standard normal samples and multiplied by $\boldsymbol{C}^{1/2}_{\text{MEG-to-head}}$. Here, the distribution of interest is the combination of *MEG-to-head* and *head-to-MRI* uncertainties. The computations below are performed in head coordinates. That is, all locations in source space, volume conductor model and sensors are all given in head coordinates. *MEG-to-head* and *head-to-MRI* parameters are both sampled in centred coordinates, see section 2.10 for details. In the following, the centring effects are transformed to the uncentred head coordinates. Let $\boldsymbol{p}_k$ and $\vec{s}_k$ be the *MEG-to-head* parameters for centred and pre-registered MEG coordinates. A point $\vec{b}$ in head coordinates is derived from a point $\vec{a}$ in the MEG coordinates by adding the mean point $\bar{\vec{b}}$

$$\vec{b} = \vec{a} + \bar{\vec{b}} \tag{3.41}$$

and hence the coregistration $\boldsymbol{R}(\boldsymbol{p}_k)\,\vec{a} + \vec{s}_k$ is transformed to head coordinates as $\boldsymbol{R}(\boldsymbol{p}_k)\left(\vec{b} - \boldsymbol{R}(\boldsymbol{p}_k)\,\bar{\vec{b}}\right) + \vec{s}_k$. That is, instead of $\vec{s}_k$ the shift vector becomes $(\vec{s}_k - \bar{\vec{b}}$ For *head-to-MRI* it is necessary to account for the difference between pre-registration and maximum likelihood estimate. This is done by applying the inverse of the maximum likelihood *head-to-MRI* to rotation and shift and is denoted by $\boldsymbol{R}'$ and $\vec{t}'$:

$$\boldsymbol{R}'(\boldsymbol{q}_l) = \boldsymbol{R}^{-1}_{\mathsf{MLE}}\boldsymbol{R}(\boldsymbol{q}_l) \tag{3.42}$$

and

$$\vec{t}\,'_l = \boldsymbol{R}^{-1}_{\mathsf{MLE}}\left(\vec{t}_l - \vec{t}_{\mathsf{MLE}}\right), \tag{3.43}$$

where $\cdot_{\mathsf{MLE}}$ is the maximum likelihood estimate. Both steps together, the transformation from centred to head coordinates and accounting for the maximum likelihood estimate in *head-to-MRI* yields a sample of the *MEG-to-MRI* translation uncertainty in head coordinates as

$$\vec{h}_{k\,l} = \vec{t}\,'_l + \boldsymbol{R}'(\boldsymbol{q}_l)\left(\vec{s}_k - \boldsymbol{R}(\boldsymbol{p}_k)\,\bar{\vec{b}} + \bar{\vec{b}} - \bar{\vec{d}}\right) + \bar{\vec{d}}, \tag{3.44}$$

where $\bar{\vec{b}}$ are the $\bar{\vec{d}}$ MEG and MRI centres, respectively. The associated rotation uncertainty is not affected by centring and simply sampled as

$$\boldsymbol{g}_{k\,l} = \text{quaternion}\left[\boldsymbol{R}'\left(\boldsymbol{q}_l\right)\boldsymbol{R}\left(\boldsymbol{p}_k\right)\right] . \tag{3.45}$$

The indices k and l in eq. (2.61) refer to the k-th and l-th subsample of *MEG-to-head* and *head-to-MRI* samples, respectively. Apart from the additional indexing, the notation is adopted from eq. (2.5) and eq. (2.16), respectively (fig. 2.1).

3.4 Definition of input variables

3.4.1 Static coregistration uncertainties

The representation of random processes in section 3.2.1 is based on theoretical univariate input parameter distributions. Each input parameter is associated with a theoretical distribution and all input parameters are independent random variables. In the uncertainty assessment chapter 2 I estimated *normally* and *students-t* distributed errors for the *MEG-to-head* and *head-to-MRI* coregistrations. The parameters of the *MEG-to-MRI* coregistration are approximately *normally* distributed with non-diagonal covariance matrices. A non-diagonal covariance matrix indicates dependency between the parameters. In order to apply stochastic spectral methods, the parameter covariance is decomposed into independent components using an singular value decomposition (SVD). The rotation and translation parameters $\boldsymbol{g}$ and $\vec{h}$ of *MEG-to-MRI* are sampled as described in section 3.3. A transformation to $\left(\boldsymbol{g},\,\vec{h}\right)$ from six independent and identically distributed Gaussian random variables $\boldsymbol{x}$ with zero mean and variance 1, is found by $\boldsymbol{C}^{1/2}_{\mathsf{MEG-to-MRI}}$, with

$$\begin{aligned}
\boldsymbol{U}\,\text{diag}\left(\boldsymbol{s}\right)\boldsymbol{V}^{\mathsf{T}} &= \frac{1}{\sqrt{N-1}}\begin{pmatrix} g_{1\,1} & g_{1\,2} & g_{1\,3} & h_{1\,1} & h_{1\,2} & h_{1\,3} \\ \vdots & \vdots & \vdots & \vdots & \vdots & \vdots \\ g_{N\,1} & g_{N\,2} & g_{N\,3} & h_{N\,1} & h_{N\,2} & h_{N\,3} \end{pmatrix} \\
\boldsymbol{C}^{1/2}_{\mathsf{MEG-to-MRI}} &= \boldsymbol{V}\,\text{diag}\left(\boldsymbol{s}\right)\boldsymbol{V}^{\mathsf{T}} ,
\end{aligned} \tag{3.46}$$

where N is the sample size. With $\boldsymbol{x}$ as input variables and the transformation $\left(\boldsymbol{g},\,\vec{h}\right) \sim \boldsymbol{C}^{1/2}_{\mathsf{MEG-to-MRI}}\boldsymbol{x}$, it is possible to analyze functions of the coregistration parameters by stochastic spectral methods on the basis of Hermite polynomials.

For example the function $f\left(\boldsymbol{g}, \vec{h}\right)$ is expanded by

$$\hat{f}\left(\boldsymbol{C}_{\mathsf{MEG-to-MRI}}^{1/2}\boldsymbol{x}\right) = \sum_{\boldsymbol{s}\in\mathcal{S}} \hat{f}_{\boldsymbol{s}} \Psi_{\boldsymbol{s}}\left(\boldsymbol{x}\right) . \tag{3.47}$$

3.4.2 Head movements

So far, in chapter 2, uncertainty of coregistrations is assessed for a moment in time or for non-moving subjects. Although some methods have been developed to account for head movements during MEG recordings, the standard MEG forward models are computed for one static coregistration. Hence, head movements add further uncertainty to the *MEG-to-head* coregistration. In this section, I propose a method to assess the amount of head movements during MEG recordings by means of a covariance matrix. Further, the mean coregistration is estimated for the use in forward models. For the coregistration uncertainty at a moment in time, I found approximately normally distributed parameters. Since the head movements are added to these parameters independently and typically with a similar magnitude, in the order of a few mm, I make use of the central limit theorem and assume that the sum of static coregistration uncertainty and head movements is normally distributed.

In the laboratory the head movements are recorded by activating five head localization coils during the measurement. The MaxFilter$^{\mathrm{TM}}$ software estimates *MEG-to-head* coregistration parameters — rotation quaternions $\boldsymbol{q}_l$ and translations $\vec{t}_l$ — for each second of the recorded data from the signals of the localization coils. Markley, Cheng, et al. (2007) have shown that the average rotation $\mathbb{E}\left[\boldsymbol{q}\right]$ of unit quaternions $\boldsymbol{q}_l$ can be found by the SVD

$$\begin{aligned} \left(\boldsymbol{q}_1, \boldsymbol{q}_2, \ldots, \boldsymbol{q}_L\right) &= \boldsymbol{U}\,\mathrm{diag}\left(\boldsymbol{\sigma}\right)\boldsymbol{V}^{\mathsf{T}} \\ \mathbb{E}\left[\boldsymbol{q}\right] &= \left(u_{1\,1}, u_{1\,2}, u_{1\,3}, u_{1\,4}\right)^{\mathsf{T}} \end{aligned} \tag{3.48}$$

as the first column eigenvector, where L is the length of the data in seconds. For the estimation of rotation covariances, the inverse of the mean rotation is applied to the rotations for centering. The centered quaternions are computed from these rotations as

$$\boldsymbol{q}_l^{\mathsf{c}} = \mathrm{quaternion}\left[\boldsymbol{R}\left(\boldsymbol{q}_l\right)\boldsymbol{R}^{-1}\left(\mathbb{E}\left[\boldsymbol{q}\right]\right)\right] \tag{3.49}$$

The mean of the translation parameters is $\mathbb{E}\left[\vec{t}\right] = \sum_{l=1}^{L}\vec{t}_l$. For the translation covariances, the methods of chapter 2 are used and the MEG coordinate system origin is initially shifted to the mean of the localization coil positions $\mathbb{E}\left[\vec{a}\right]$, which is computed from $\mathbb{E}\left[\boldsymbol{q}\right]$ and $\mathbb{E}\left[\vec{t}\right]$. Let the point $\vec{a}^{\mathsf{MEG}}$ be a point in MEG coordinates,

which is aligned in head coordinates by *MEG-to-head* as

$$\vec{a}^{\,\mathsf{head}} = \boldsymbol{R}\left(\boldsymbol{q}_l\right)\vec{a}^{\,\mathsf{MEG}} + \vec{t}_l\,. \tag{3.50}$$

The shift of the MEG origin to $\mathbb{E}\left[\vec{a}\right]$ can be expressed as

$$\vec{a}^{\,\mathsf{head}} = \boldsymbol{R}\left(\boldsymbol{q}_l\right)\left(\vec{a}^{\,\mathsf{MEG}} - \mathbb{E}\left[\vec{a}\right]\right) + \vec{t}_l + \boldsymbol{R}\left(\boldsymbol{q}_l\right)\mathbb{E}\left[\vec{a}\right] \tag{3.51}$$

and the shifted translation vector is defined as

$$\vec{t}_{l\,o} = \vec{t}_l + \boldsymbol{R}\left(\boldsymbol{q}_l\right)\mathbb{E}\left[\vec{a}\right]\,. \tag{3.52}$$

The covariance matrix of the *MEG-to-head* coregistration parameters due to head movements is estimated as

$$\begin{aligned} \boldsymbol{C}_{movement} &= \frac{1}{L-1}\boldsymbol{M}\boldsymbol{M}^{\mathsf{T}} \\ \boldsymbol{M} &= \begin{pmatrix} \boldsymbol{q}_1^{\mathsf{c}} & \cdots & \boldsymbol{q}_L^{\mathsf{c}} \\ \vec{t}_{1\,o} - \mathbb{E}\left[\vec{t}_o\right] & \cdots & \vec{t}_{L\,o} - \mathbb{E}\left[\vec{t}_o\right] \end{pmatrix}. \end{aligned} \tag{3.53}$$

Because a static *MEG-to-head* coregistration uncertainty with covariance matrix $\boldsymbol{C}_{static}$ is independent from head movements, the total *MEG-to-head* covariance matrix for head movements and coil localization errors is

$$\boldsymbol{C}_{dynamic} = \boldsymbol{C}_{movement} + \boldsymbol{C}_{static}\,. \tag{3.54}$$

3.4.3 Target registration error

By using the transformation of the coregistration parameters from section 3.4.1 it is straightforward to sample the TRE $\vec{\phi}$ at a point $\vec{a}$ in the head coordinate system. Let $\boldsymbol{C}^{1/2}_{\mathsf{MEG-to-MRI}}$ be the transformation matrix from six independent and identically distributed standard Gaussian random variables $\boldsymbol{x}$ to the *MEG-to-MRI* coregistration parameters $\left(\boldsymbol{g},\,\vec{h}\right)$. A sample of coregistration parameters is obtained as

$$\left(g_{l\,1},\,g_{l\,2},\,g_{l\,3},h_{l\,1},\,h_{l\,2},\,h_{l\,3}\right)^{\mathsf{T}} = \boldsymbol{C}^{1/2}_{\mathsf{MEG-to-MRI}}\boldsymbol{x}_l\,. \tag{3.55}$$

The TRE at $\vec{a}$ is sampled accordingly as

$$\vec{\psi}\left(\boldsymbol{g}_l,\,\vec{h}_l\right) = \boldsymbol{R}\left(\boldsymbol{g}_l\right)\vec{a} + \vec{h}_l\,. \tag{3.56}$$

For a set of M points the mean RMS of TRE at these points is defined by

$$\mathbb{E}\left[\mathrm{RMS}\left(\mathbf{\Psi}\right)\right] = \frac{1}{L}\sum_{l=1}^{L}\sqrt{\frac{1}{M}\sum_{m=1}^{M}|\vec{\psi}_m\left(\boldsymbol{g}_l, \vec{h}_l\right)|^2}\,, \tag{3.57}$$

where L is the sample size of the mean estimation.

3.5 Forward modeling

3.5.1 Source space

In MEG forward computations, the magnetic flux is computed for given source configurations. That is, each source is defined by its dipole location, orientation and strength. A source space defines the space of dipole locations and dependent on the modeling it can constrain dipole orientations, for example to surface normals. Here, the dipole locations are defined by the vertices of the white matter triangulation from the *FreeSurfer* software. Figure 3.6 depicts the *FreeSurfer* white matter triangulation. Here, the triangulation is based on the topology of a recursively subdivided icosahedron with 5 subdivisions. This is done separately for left and right hemispheres and results in 10 242 sources per hemisphere. Sources with a distance smaller than 5 mm to the closest volume conductor boundary are excluded from the source space.

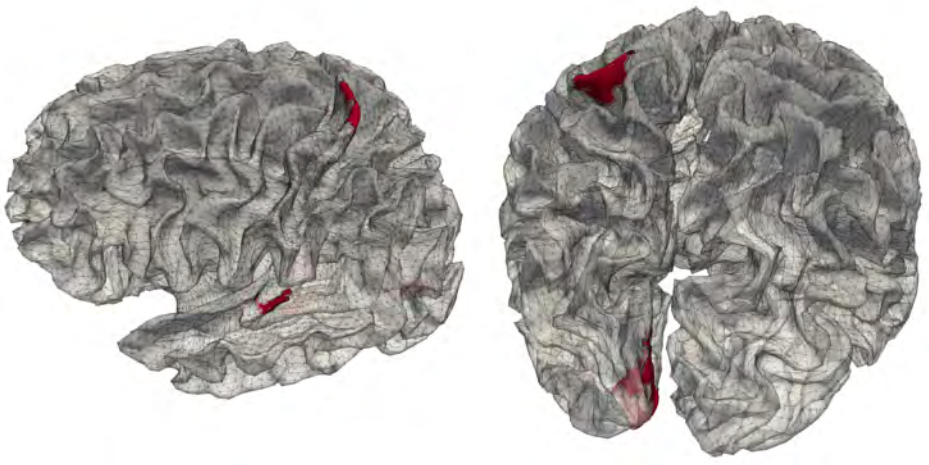

(a) (b)

Figure 3.6: Source space triangulation from (a) saggital and (b) coronal view. The sources are located at the vertices of the triangulation. Three red areas indicate the test patches of auditory, visual and somatosensory sources.

The red patches in the left auditory, visual and somatosensory regions are used for forward computations below. Source normal orientations are derived from a finer *FreeSurfer* surface triangulation compared to the source space in fig. 3.6 by using cortical patch statistics (F.-H. Lin et al., 2006). The normal orientations are used to constrain the source estimates in sections 3.6.2 and 3.6.3.

3.5.2 Regions of interest

Many MEG studies are based on the stimulation of certain functional brain regions, for example auditory stimuli are presented which are supposed to activate primarily auditory regions. Hence, often also the source analysis is restricted to functional regions of interest. Here, three regions of interest are defined, namely auditory, visual and somatosensory regions. The definition of each region is derived from the human cerebral cortex parcellation of Glasser et al. (2016). In table 3.1 parcellation labels are listed for each region and left/right refers to the left/right brain hemispheres.

Table 3.1: Definition of auditory, visual and somatosensory regions of interests from parcellation labels.

auditory	visual	somatosensory
• left broadman area (BA) 52 • left primary auditory cortex (A1) • left auditory 4 complex (A4) • left auditory 5 complex (A5) • left lateral belt complex (LBelt) • left medial belt complex (MBelt) • left para-belt complex (PBelt) • left para-insular area (PI) • left retro-insular cortex (RI) • left dorsal bank of superior temporal sulcus posterior (STSdp) • left anterior superior temporal area TA2 (Economo and Koskinas, 1925) (TA2)	• left primary visual cortex (V1) • left second visual area (V2) • right V1	• left BA 1 • left BA 2 • left BA 3a • left BA 3b

For the visual region, I decided to include the right V1 label. Figure 3.7 depicts the result of the region of interest definitions for one subject.

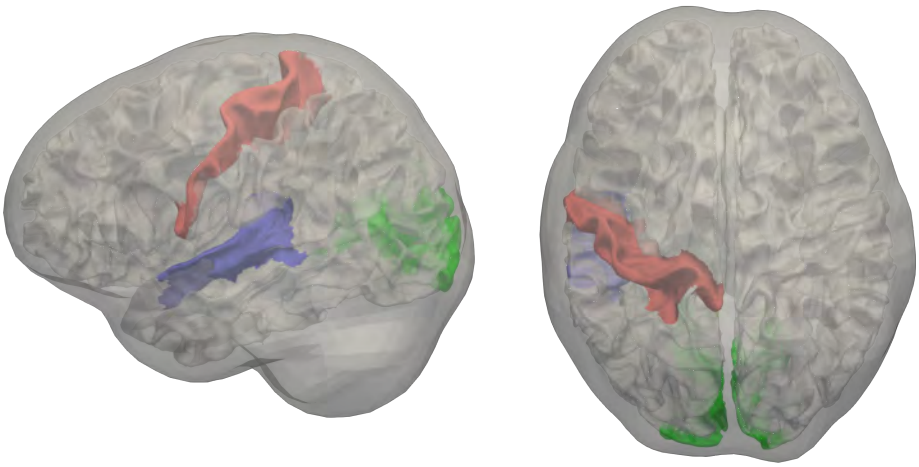

(a) (b)

Figure 3.7: The inner skull compartment and source space is shown from (a) saggital and (b) axial views. Regions of interest are coloured in blue, green and red for the auditory, visual and somatosensory regions, respectively.

3.5.3 Volume conductor and boundary element method

Bioelectrical effects due to brain activity are characterized by the second order elliptic partial differential equation

$$\nabla \cdot \left(\sigma\left(\vec{r}\right) \nabla \phi\left(\vec{r}\right)\right) = \boldsymbol{j}\left(\vec{r}_p\right) \,, \tag{3.58}$$

where $\sigma\left(\vec{r}\right)$ is the specific electric conductivity of the tissue, $\phi\left(\vec{r}\right)$ is the electric potential and $\boldsymbol{j}\left(\vec{r}_p\right)$ is the primary current density at source position $\vec{r}_p$ (Stenroos, Mäntynen, and Nenonen, 2007). Let the primary current density be described by an equivalent current dipole, with dipole moment $\boldsymbol{p}$. From the Biot Savart law follows the primary magnetic flux density $\boldsymbol{b}_\infty$ of a current dipole inside infinite vacuum space as

$$\boldsymbol{b}_\infty\left(\vec{r}\right) = \frac{\mu_0}{4\pi} \frac{\boldsymbol{p} \times \left(\vec{r} - \vec{r}_p\right)}{\left|\vec{r} - \vec{r}_p\right|^3} \,, \tag{3.59}$$

where $\left(\vec{r}\right)$ is the sensor position and μ_0 is the magnetic permeability of the vacuum. Primary current dipoles inside a conductive volume like the brain cause a secondary magnetic flux density $\boldsymbol{b}_{vol}$ which is caused by the ohmic currents inside the volume conductor. From the divergence theorem follows the expression of the secondary

magnetic flux density as

$$\boldsymbol{b}_{vol}\left(\vec{r}\right) = -\frac{\mu_0}{4\pi}\sum_{l=1}^{L}\left(\sigma_{l-} - \sigma_{l+}\right)\int_{\partial\Omega_l}\phi\left(\vec{r}\,'\right)\mathrm{d}\vec{s}\,' \times \frac{\vec{r} - \vec{r}\,'}{|\vec{r} - \vec{r}\,'|^3}\,, \tag{3.60}$$

where σ_{l-} and σ_{l+} are the specific electric conductivities inside and outside of a homogeneous compartment l with boundary surface $\partial\Omega_l$ and ϕ is the electric potential at the boundary surfaces (Geselowitz, 1970; Stenroos, Mäntynen, and Nenonen, 2007). For this thesis, only one compartment, namely the inner skull comparment, is used for volume conductor modeling and the secondary magnetic flux density reads as

$$\boldsymbol{b}_{vol}\left(\vec{r}\right) = -\frac{\mu_0\sigma_{skull-}}{4\pi}\int_{\partial\Omega}\phi\left(\vec{r}\,'\right)\mathrm{d}\vec{s}\,' \times \frac{\vec{r} - \vec{r}\,'}{|\vec{r} - \vec{r}\,'|^3}\,. \tag{3.61}$$

The total magnetic flux density $\boldsymbol{b}$ at sensor position $\vec{r}$ due to a current dipole $\boldsymbol{p}$ at $\vec{r}_p$ is the sum of primary and secondary flux density

$$\boldsymbol{b}\left(\vec{r}\right) = \boldsymbol{b}_{\infty}\left(\vec{r}\right) + \boldsymbol{b}_{vol}\left(\vec{r}\right)\,. \tag{3.62}$$

In the computations for this thesis, the surface potential ϕ is computed by using the Helsinki BEM library (Stenroos, Mäntynen, and Nenonen, 2007). The surface integral in eq. (3.61) is computed analytically over the triangulation of the inner skull surface, where the element integrals are solved for the linear potential approach (Ferguson, Xu Zhang, and Stroink, 1994). For source estimation it is convenient to write the normal magnetic flux density $b_k = \boldsymbol{b}\left(\vec{r}_k\right)\cdot\boldsymbol{n}_k$ at the MEG sensor positions $\vec{r}_k$, with sensor orientation $\boldsymbol{n}_k$ in terms of the matrix equation

$$\begin{pmatrix} b_1 \\ b_2 \\ b_3 \\ \vdots \\ b_N \end{pmatrix} = \boldsymbol{L}\begin{pmatrix} p_{1\,x} \\ p_{1\,y} \\ p_{1\,z} \\ \vdots \\ p_{M\,z} \end{pmatrix}\,, \quad \boldsymbol{L} \in \mathbb{R}^{N\times 3M}\,, \tag{3.63}$$

where $\boldsymbol{L}$ is referred to as leadfield matrix and $p_{m\,x}$ is the x-component of a dipole moment at source position $\vec{r}_{p\,m}$ and so on for y and z.

3.5.4 Expansion of forward operators

Since both $\boldsymbol{b}_{\infty}$ and $\boldsymbol{b}_{vol}$ depend on the sensor position relative to the source and volume conductor position, both terms also depend on the *MEG-to-MRI* coregis-

tration. The leadfield matrix from the previous section, which is also referred to as forward operator, is the sum of primary and secondary magnetic flux density per unit dipole moment:

$$\boldsymbol{L} = \boldsymbol{L}_{\infty} + \boldsymbol{L}_{vol}\,. \tag{3.64}$$

The effects of coregistration uncertainty on the forward operator are separately analyzed for $\boldsymbol{L}_{\infty}$ and $\boldsymbol{L}_{vol}$. Only uncertainties in the translations in x, y and z-direction (h_x, h_y, h_z) are analyzed. In this analysis, h_x, h_y and h_z are independent random variables following a Gaussian distribution with zero mean and standard deviation of 2 mm. The elements of the forward operator are expanded as

$$\begin{aligned}
l_{\infty\, n\, m}\,(h_x,\, h_y,\, h_z) &\approx \sum_{\boldsymbol{s}\in\mathcal{S}} \hat{l}_{\infty\, n\, m\, \boldsymbol{s}}\, \Psi_{\boldsymbol{s}} \left(\frac{h_x}{2\,\mathrm{mm}},\, \frac{h_y}{2\,\mathrm{mm}},\, \frac{h_z}{2\,\mathrm{mm}} \right) \\
l_{vol\, n\, m}\,(h_x,\, h_y,\, h_z) &\approx \sum_{\boldsymbol{s}\in\mathcal{S}} \hat{l}_{vol\, n\, m\, \boldsymbol{s}}\, \Psi_{\boldsymbol{s}} \left(\frac{h_x}{2\,\mathrm{mm}},\, \frac{h_y}{2\,\mathrm{mm}},\, \frac{h_z}{2\,\mathrm{mm}} \right) \\
l_{n\, m}\,(h_x,\, h_y,\, h_z) &\approx \sum_{\boldsymbol{s}\in\mathcal{S}} \left(\hat{l}_{\infty\, n\, m\, \boldsymbol{s}} + \hat{l}_{vol\, n\, m\, \boldsymbol{s}} \right) \Psi_{\boldsymbol{s}} \left(\frac{h_x}{2\,\mathrm{mm}},\, \frac{h_y}{2\,\mathrm{mm}},\, \frac{h_z}{2\,\mathrm{mm}} \right) .
\end{aligned} \tag{3.65}$$

In this thesis, the expansions eq. (3.65) are used to approximate the forward operator efficiently for a profound uncertainty and sensitivity analysis.

3.5.5 Error of forward computations

For the comparison of approximations with reference solutions at the sensors, the relative difference measure (RDM) and the magnification (MAG) were introduced (Meijs et al., 1989). The RDM measures differences in the field topography and is not affected by scalings of the global field strength by positive factors. A minimal RDM of zero indicates no topography differences between two fields. And a maximal RDM of two is reached when one field is a negative multiplication of the other. The MAG measures the error of global scaling between two fields, where a MAG of one indicates no scaling error and MAGs of zero and infinity indicate maximal scaling

errors. Both measures are defined according to

$$\begin{aligned} RDM &= \sqrt{\sum_{n=1}^{N}\left(\frac{b_n}{\sqrt{\sum_{n=1}^{N} b_n^2}} - \frac{\hat{b}_n}{\sqrt{\sum_{n=1}^{N} \hat{b}_n^2}}\right)^2} \in [0,2] \\ MAG &= \sqrt{\frac{\sum_{n=1}^{N} \hat{b}_n^2}{\sum_{n=1}^{N} b_n^2}} \geq 0\,, \end{aligned} \tag{3.66}$$

where b_n and $\hat{b}_n$ denote the reference and approximation field values at sensor n and N is the number of sensors.

3.6 MEG source estimation

3.6.1 Introduction

For the estimation of locations and time courses of neural activity from MEG data, a variety of different methods exist. Source estimators can be classified into three main branches, dipole search methods, scanning methods and estimators of distributed sources. All classes of methods are based on the idea, that sensor data $\boldsymbol{d}$ of measured brain activity can be expressed by the sum of fields from dipolar sources in the brain plus noise. In the context of scanning and distributed inversion methods, source estimates are estimates of dipole moments for given sensor data. The dipole moments, representing brain activity, are denoted by $\boldsymbol{p}$ and together with the leadfield matrix from above, the sensor data read

$$\boldsymbol{d} = \boldsymbol{L}\boldsymbol{p} + \boldsymbol{\nu}\,. \tag{3.67}$$

Normally, it is assumed that the sensor noise $\boldsymbol{\nu}$ follows a multivariate Gaussian distribution with zero mean and its covariance matrix $\boldsymbol{C}_\nu$ is estimated from the data. For the formulation of source estimators, it is convenient to introduce a whitening matrix $\boldsymbol{C}_\nu^{-1/2}$, whitened data and leadfield as

$$\begin{aligned} \tilde{\boldsymbol{d}} &= \boldsymbol{C}_\nu^{-1/2}\boldsymbol{d} \\ \tilde{\boldsymbol{L}} &= \boldsymbol{C}_\nu^{-1/2}\boldsymbol{L}\,. \end{aligned} \tag{3.68}$$

The purpose of this transformation is apparent when it is applied to eq. (3.67) because $\boldsymbol{C}_{\nu}^{-1/2}\boldsymbol{\nu}$ follows a Gaussian distribution where the covariance matrix is equal to the identity matrix $\boldsymbol{I}$ (Hämäläinen, F. H. Lin, and Mosher, 2010).

3.6.2 Beamformer

From the class of scanning methods, a vector beamformer is implemented for this thesis. The LCMV beamformer is known to have the solution

$$\boldsymbol{W}^{\mathsf{T}}\left(\vec{r}\right) = \left(\boldsymbol{L}^{\mathsf{T}}\left(\vec{r}\right)\boldsymbol{C}_{d}^{-1}\boldsymbol{L}\left(\vec{r}\right)\right)^{-1}\boldsymbol{L}^{\mathsf{T}}\left(\vec{r}\right)\boldsymbol{C}_{d}^{-1} \tag{3.69}$$

at source location $\vec{r}$, where $\boldsymbol{C}_{d}^{-1}$ is the inverse of the data covariance matrix and $\boldsymbol{L}$ is the leadfield matrix (Van Veen et al., 1997). Following Hillebrand and Barnes (2003), an unfocussed beamformer is used in this thesis, where the data covariance matrix is a scaled identity matrix $\boldsymbol{C}_{d} = \sigma^{2}\boldsymbol{I}$ and the beamformer weights become

$$\boldsymbol{W}^{\mathsf{T}}\left(\vec{r}\right) = \left(\boldsymbol{L}^{\mathsf{T}}\left(\vec{r}\right)\boldsymbol{L}\left(\vec{r}\right)\right)^{-1}\boldsymbol{L}^{\mathsf{T}}\left(\vec{r}\right) . \tag{3.70}$$

In contrast to Hillebrand and Barnes (2003), the leadfield $\boldsymbol{L}\left(\vec{r}\right)$ is not a column vector, it consists of three columns $\boldsymbol{L}\left(\vec{r}\right) = \left(\boldsymbol{l}_{t1}\left(\vec{r}\right), \boldsymbol{l}_{t2}\left(\vec{r}\right), \boldsymbol{l}_{n}\left(\vec{r}\right)\right)$, where the indices $t1$, $t2$ and n decode the two cortical tangential and one cortical normal dipole orientation, respectively. In order to be comparable with the distributed source estimator, I decided to introduce a loose orientation parameter θ which is implemented in a prior source covariance matrix $\boldsymbol{R}$, where

$$\boldsymbol{R}^{1/2} = \begin{pmatrix} \theta & 0 & 0 \\ 0 & \theta & 0 \\ 0 & 0 & 1 \end{pmatrix} . \tag{3.71}$$

The loose orientation parameter can take values from zero to one, where a value of zero results in a completely orientation constrained beamformer and a value of one results in an unconstrained beamformer. That is, in the constrained case only the cortical normal dipole component is estimated and the cortical tangential components are zero. In the unconstrained case, the dipole orientation is free and it is linearly optimized in the least squares sense. The whitened beamformer with incorporated prior source covariance matrix reads

$$\tilde{\boldsymbol{W}}_{\theta}^{\mathsf{T}}\left(\vec{r}\right) = \boldsymbol{R}^{1/2}\left(\boldsymbol{R}^{1/2}\tilde{\boldsymbol{L}}^{\mathsf{T}}\left(\vec{r}\right)\tilde{\boldsymbol{L}}\left(\vec{r}\right)\boldsymbol{R}^{1/2}\right)^{-1}\boldsymbol{R}^{1/2}\tilde{\boldsymbol{L}}^{\mathsf{T}}\left(\vec{r}\right) . \tag{3.72}$$

A solution to eq. (3.72) is found by the following SVD

$$\begin{aligned} \boldsymbol{U}\,\mathrm{diag}\,(\boldsymbol{\sigma})\,\boldsymbol{V}^{\mathsf{T}} &= \tilde{\boldsymbol{L}}\,(\vec{r})\,\boldsymbol{R}^{1/2} \\ \tilde{\boldsymbol{W}}_{\theta}^{\mathsf{T}}\,(\vec{r}) &= \boldsymbol{R}^{1/2}\boldsymbol{V}\,\mathrm{diag}\,(1/\sigma_1,\,1/\sigma_2,\,1/\sigma_3)\,\boldsymbol{U}^{\mathsf{T}} \end{aligned} \tag{3.73}$$

For better numerical stability, eq. (3.73) is regularized by using the truncated SVD

$$\tilde{\boldsymbol{W}}_{\theta,\,trunc}^{\mathsf{T}}\,(\vec{r}) = \boldsymbol{R}^{1/2}\boldsymbol{V}\,\mathrm{diag}\,(1/s_1,\,1/s_2,\,0)\,\boldsymbol{U}^{\mathsf{T}}\,, \quad s_l = \begin{cases} \sigma_l & \sigma_l > \sigma_1 \cdot \epsilon \\ 0 & \sigma_l \leq \sigma_1 \cdot \epsilon \end{cases}, \tag{3.74}$$

where ϵ is the machine precision. The third singular value is set to zero because the MEG is only sensitive to two source orientations, which are associated to the two first singular values. Finally, a noise normalized beamformer $\tilde{\boldsymbol{Z}}$ is computed as

$$\tilde{\boldsymbol{Z}}^{\mathsf{T}}\,(\vec{r}) = \tilde{\boldsymbol{W}}_{\theta,\,trunc}^{\mathsf{T}} \Big/ \sqrt{\mathrm{tr}\left\{\tilde{\boldsymbol{W}}_{\theta,\,trunc}^{\mathsf{T}}\,(\vec{r})\,\tilde{\boldsymbol{W}}_{\theta,\,trunc}\,(\vec{r})\right\}}\,. \tag{3.75}$$

This beamformer is related to the Borgiotti–Kaplan beamformer (Sekihara et al., 2001). Since $\tilde{\boldsymbol{Z}}^{\mathsf{T}}\,(\vec{r})$ is a function of the leadfield matrix, it is also a function of the coregistration parameters $\boldsymbol{x}$ and can be expressed as $\tilde{\boldsymbol{Z}}^{\mathsf{T}}\,(\vec{r},\,\boldsymbol{x})$.

3.6.3 sLORETA

From distributed source estimators, the standardized low resolution brain electromagnetic tomography (sLORETA) is implemented for this thesis. It is based on the widely used minimum norm estimate (MNE), where the dipole moments are estimated as

$$\boldsymbol{s}^{\mathsf{MNE}} = \boldsymbol{R}\tilde{\boldsymbol{L}}^{\mathsf{T}}\left(\tilde{\boldsymbol{L}}\boldsymbol{R}\tilde{\boldsymbol{L}}^{\mathsf{T}} + \lambda^2\boldsymbol{I}\right)^{-1}\tilde{\boldsymbol{d}} = \tilde{\boldsymbol{\Lambda}}\tilde{\boldsymbol{d}}, \quad \tilde{\boldsymbol{\Lambda}} \in \mathbb{R}^{3M\times N}\,, \tag{3.76}$$

where M is the number of source positions and N is the number of sensors and λ is a regularization parameter. In contrast to the beamformer, the leadfield of the entire source space

$$\boldsymbol{L} = (\boldsymbol{l}_{t1}\,(\vec{r}_1)\,,\ \boldsymbol{l}_{t2}\,(\vec{r}_1)\,,\boldsymbol{l}_n\,(\vec{r}_1)\,,\ \ldots,\ \boldsymbol{l}_{t1}\,(\vec{r}_m)\,,\boldsymbol{l}_{t2}\,(\vec{r}_m)\,,\boldsymbol{l}_n\,(\vec{r}_m)) \in \mathbb{R}^{N\times 3M} \tag{3.77}$$

is involved and the prior source covariance matrix $\boldsymbol{R}$ is a square diagonal matrix of size $3M$, it is constructed from the loose parameter θ as

$$\boldsymbol{R}^{1/2} = \begin{pmatrix} \theta & 0 & 0 & \dots & 0 \\ 0 & \theta & 0 & \dots & 0 \\ 0 & 0 & 1 & \dots & 0 \\ \vdots & \vdots & \vdots & \ddots & \vdots \\ 0 & 0 & 0 & \dots & 1 \end{pmatrix}. \tag{3.78}$$

The loose orientation constraint was previously used by F.-H. Lin et al. (2006), where they defined the loose parameter as sine of the angle to the cortical normal orientation. It has been shown, that it is reasonable to choose $\lambda^2 = \frac{1}{\xi^2} \operatorname{tr}\left(\tilde{\boldsymbol{L}}\boldsymbol{R}\tilde{\boldsymbol{L}}^{\mathsf{T}}\right)/N$, where ξ^2 is the power signal-to-noise ratio (SNR) of the whitened data. I fixed $\xi^2 = 10$ in the style of the default value of 9 in the MNE software (Hämäläinen, 2010). In order to be comparable with other functional imaging methods (fMRI, PET) and the noise normalized beamformer of this thesis, the sLORETA noise normalization is applied to $\boldsymbol{s}^{\mathsf{MNE}}$. The sLORETA method defines resolution matrix diagonal elements as

$$n_l = \frac{1}{\lambda^2}\left(\tilde{\boldsymbol{\Lambda}}\left(\tilde{\boldsymbol{L}}\boldsymbol{R}\tilde{\boldsymbol{L}}^{\mathsf{T}} + \lambda^2\boldsymbol{I}\right)\tilde{\boldsymbol{\Lambda}}^{\mathsf{T}}\right)_{ll} \tag{3.79}$$

for noise normalization (Pascual-Marqui, 2002). In this thesis the sLORETA activity estimate is computed for source position k as

$$\boldsymbol{s}_k^{\mathsf{sLORETA}} = \frac{\left(s^{\mathsf{MNE}}_{3(k-1)+1},\, s^{\mathsf{MNE}}_{3(k-1)+2},\, s^{\mathsf{MNE}}_{3(k-1)+3}\right)^{\mathsf{T}}}{\sqrt{\sum_{l=1}^{3} n_{(3k-1)+l}}} = \tilde{\boldsymbol{Z}}^{\mathsf{sLORETA}}(\vec{r}_k)\,\tilde{\boldsymbol{d}}\,. \tag{3.80}$$

The sLORETA operator is a function of source position $\vec{r}$ and coregistration parameters $\boldsymbol{x}$ and it can be expressed as $\tilde{\boldsymbol{Z}}^{\mathsf{sLORETA}}(\vec{r}, \boldsymbol{x})$.

3.6.4 Expansion of source estimators

Both estimators, the proposed beamformer and sLORETA can be expressed as functions of the coregistration parameters and approximated by polynomial expansions. Let me therefore introduce a general matrix operator $\boldsymbol{\Gamma}$ of size $3M \times N$, where M is the number of source positions and N is the number of sensors. For this thesis, $\boldsymbol{\Gamma}$ can take four different forms, namely beamformer and sLORETA operator, each with fixed orientation ($\theta = 0$) or loose parameter $\theta = 0.2$. In any case, $\boldsymbol{\Gamma}$ is a function of

the six coregistration parameters $\boldsymbol{x}$. The matrix elements of $\boldsymbol{\Gamma}$ are denoted by $\gamma_{m\,n}$ and a stochastic spectral approximation of Γ reads

$$\gamma_{m\,n}\left(\boldsymbol{x}\right) \approx \sum_{\boldsymbol{s}\in\mathcal{S}} \hat{\gamma}_{m\,n\,\boldsymbol{s}} \Psi_{\boldsymbol{s}}\left(\boldsymbol{x}\right) . \tag{3.81}$$

Source estimates $\boldsymbol{s}$ for given sensor data $\boldsymbol{d}$ are computed by the matrix multiplication $\boldsymbol{s} = \boldsymbol{\Gamma}\boldsymbol{d}$ and its stochastic spectral approxmiation is

$$\begin{aligned} s_m\left(\boldsymbol{x}\right) &\approx \sum_{n}^{N} \left[d_n \sum_{\boldsymbol{s}\in\mathcal{S}} \hat{\gamma}_{m\,n\,p} \Psi_{\boldsymbol{s}}\left(\boldsymbol{x}\right) \right] = \sum_{\boldsymbol{s}\in\mathcal{S}} \hat{s}_{m\,\boldsymbol{s}} \Psi_{\boldsymbol{s}}\left(\boldsymbol{x}\right) \\ \hat{s}_{m\,\boldsymbol{s}} &= \sum_{n=1}^{N} d_n \hat{\gamma}_{m\,n\,\boldsymbol{s}} . \end{aligned} \tag{3.82}$$

That is, the polynomial coefficients of source estimates are obtained by a weighted sum of the polynomial coefficients of the estimator, where the weights are the sensor data. Hence, the coefficients of source estimators Γ are computed only once and used to efficiently compute the coefficients of source estimates $\boldsymbol{s}$ for different sensor data.

3.6.5 Verification

Expansions of source estimators are applied to testing data, which consist of simulated brain activity from three regions of interest and additive noise of three different levels. For the computations, test patches were defined as subregions of the regions of interest in the left auditory, visual and somatosensory cortex. More precisely, the parcellation labels *left PBelt*, *left 1* and *left V1* were devided by using *FreeSurfer* into 3, 6 and 8 divisions, respectively. The second, fourth and second division define the auditory, visual and somatosensory test patches, respectively. Test patches contain the test sources as vertices and are visualized red in fig. 3.6 at the source space triangulation.

In order to avoid an inverse crime in source estimation, the positions of the test sources are shifted away from the original source space by a random vector following a Gaussian distribution with zero mean and 1 mm standard deviation in x, y and z-direction. Each source was simulated as a fixed dipole with orientation normal to the cortex and a dipole moment of 1 nA m. For the additive sensor noise, a noise covariance matrix $\boldsymbol{C}_{\nu}$ was estimated from empty room measurements and a noise

sample $\boldsymbol{\nu}$ was simulated as

$$\boldsymbol{\nu} = \frac{1}{a} \cdot \boldsymbol{C}^{1/2} \boldsymbol{\epsilon}\,, \quad \boldsymbol{\epsilon} \sim \mathcal{N}\left(\mathbf{0},\, \boldsymbol{I}\right)\,, \tag{3.83}$$

where a is proportional to the amplitude SNR and for this thesis, values of 2, 10 and 50 are used.

3.6.6 Source amplitude maximum distribution

A distribution of source amplitude maximum locations is found by Monte Carlo simulation of source estimates from a distribution of coregistration parameters. Here, the domain of maximum locations is the discrete space of source locations in a region of interest. A maximum location is defined by the maximal source strength within the region Ω as

$$\vec{r}_{max} = \underset{\vec{r}}{\operatorname{argmax}} |\boldsymbol{s}\left(\vec{r}\right)|\,, \quad \vec{r} \in \Omega\,, \tag{3.84}$$

where $\boldsymbol{s}\left(\vec{r}\right)$ is the vector source estimate at $\vec{r}$. Since the maximum location is a function of coregistration parameters, a sample $(\vec{r}_{max\,1},\, \vec{r}_{max\,2}, \ldots \vec{r}_{max\,M})$ of its distribution is sampled by Monte Carlo simulation from a sample of the coregistration parameters. The spatial distribution of the maximum is modeled by the mean $\bar{\vec{r}}_{max}$ and standard deviations σ_1, σ_2, σ_3 on its three SVD-main axes:

$$\frac{1}{\sqrt{M-1}} \left(\vec{r}_{max\,1} - \bar{\vec{r}}_{max}, \ldots \vec{r}_{max\,M} - \bar{\vec{r}}_{max}\right) = \left(\vec{u}_1,\, \vec{u}_2,\, \vec{u}_3\right) \operatorname{diag}\left(\sigma_1,\, \sigma_2,\, \sigma_3\right) \boldsymbol{v}\,, \tag{3.85}$$

where the vectors $\vec{u}_l$ are normalized oriented along the main axes.

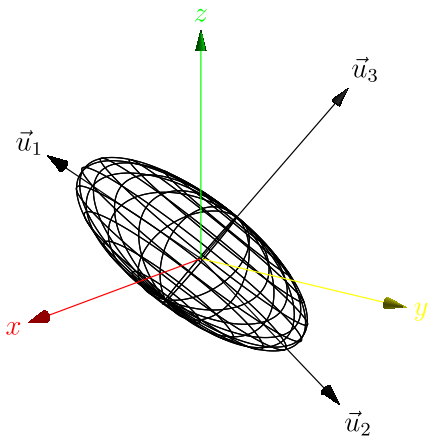

Figure 3.8: The ellipsoid represents a spatial confidence interval, where the surface intersects with the u_1, u_2 and u_3 axes at $\pm\sigma_1$, $\pm\sigma_2$ and $\pm\sigma_3$, respectively.

Figure 3.8 depicts the surface of a spatial one standard deviation confidence interval for an example maximum distribution. In the results section 4.3.2, the maximum distribution is depicted by such wire frame surfaces in the source space. As a measure of source localization errors, the absolute element-wise differences between $\vec{\bar{r}}_{max}$ and the center of the test patch are computed and denoted by $\vec{\delta} = (\delta_x, \delta_y, \delta_z)^\mathsf{T}$ in the results section. These localization error elements are expressed as

$$\delta_x = |\bar{r}_{max\,x} - \bar{r}_{patch\,x}|\,, \tag{3.86}$$

here exemplarily for the x axis, where $\bar{r}_{patch\,x}$ is the average x-location of the source patch.

Chapter 4

Results

4.1 Errors and residuals

4.1.1 MEG-to-Head

The smallest value for the maximal deviation measured by the Kolmogorov–Smirnov statistics (see eq. (2.57)), between the points and theoretical distributions was found for the *generalized normal* distribution with shape $\lambda = 1.7$ and which estimated to $D_{\tilde{\delta}} = 4.5 \times 10^{-3} \pm 0.6 \times 10^{-3}$. The maximal Kolmogorov–Smirnov-value for the *normal* distribution with scale $\sigma_{\hat{\epsilon}} = 1.05\,\mathrm{mm}$ was only slightly larger: $D_{\hat{\delta}} = 6.2 \times 10^{-3} \pm 0.8 \times 10^{-3}$. The *normal* distribution is the special case of the *generalized normal* distribution with shape $\lambda = 2$. Hence, I decided to approximate the error distribution of ϵ using the commonly used *normal* distribution. The probability density of the error estimate $\hat{\epsilon}$ was therefore defined as

$$\pi_{\hat{\epsilon}}(x) = \frac{1}{\sigma_{\hat{\epsilon}}\sqrt{2\pi}} \exp\left[-\frac{x^2}{2\sigma_{\hat{\epsilon}}^2}\right]. \tag{4.1}$$

This choice provided control over the approximations, since closed form solutions are available under the precondition of the *normal* distribution for the relation between variances (error, residual, and parameter) in a least squares estimation (Fitzpatrick, 2009). The ratio between the variances of errors and residuals was found to be $\sigma_{\hat{\epsilon}}^2/\sigma_{\hat{\delta}}^2 = 1.65 \approx 5/3$, which is approximately the ratio of the number of data points and the number of data points minus the degrees of freedom of the least squares fit, namely $3M/(3M-6) = M/(M-2)$.

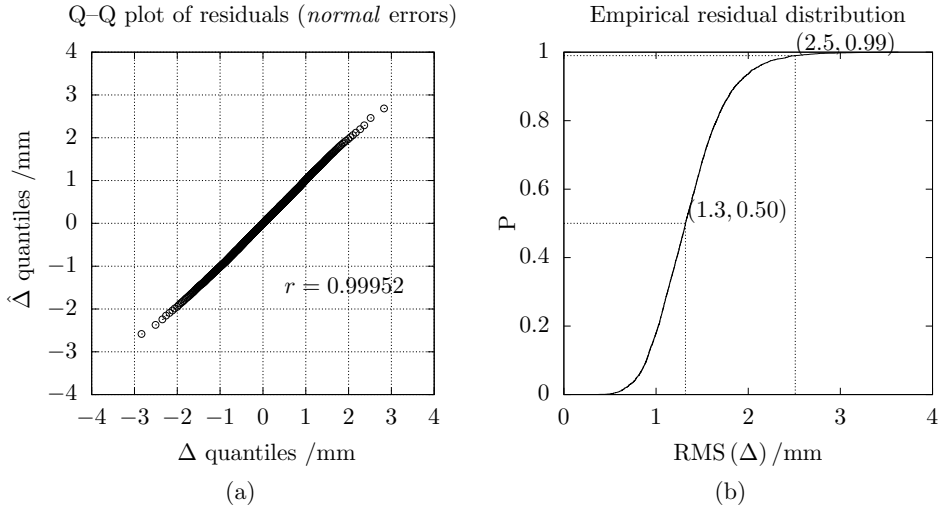

Figure 4.1: The MEG-to-head residuals Q–Q plot (a) depicts every 100*th data point of the* $\hat{\Delta}$*-quantiles over the* Δ*-quantiles. The* r*-value is the correlation coefficient between the paired sample quantiles. The empirical distribution function of RMS of observed MEG-to-head residuals is depicted in (b).*

Figure 4.1a demonstrates the distribution-wise similarity between $\hat{\Delta}$ and Δ using a Q–Q plot, where $\hat{\epsilon} \sim \mathcal{N}\left(0,\, (1.05\,\mathrm{mm})^2\right)$. If both distributions were identical, the Q–Q plot would show a straight diagonal. Divergence from linearity at both ends show that the deviations between the two distributions were mainly observed with respect to the tails. The residuals $\hat{\Delta}$ and Δ were distributed between -3 to 3 mm, with approximately zero median and mean. In fig. 4.1b, the distribution of observed RMS of residuals is plotted for the 5 544 *MEG-to-head* data sets. One RMS value is calculated over the 5 residual vectors $\vec{\delta}_m$ of the coil positions. Figure 4.1b shows that RMS values were smaller or equal to 2.5 mm for 99 % of the *MEG-to-head* data sets. The RMS values were distributed between 0.4 to 3.6 mm, with a median of 1.3 mm.

4.1.2 Head-to-MRI

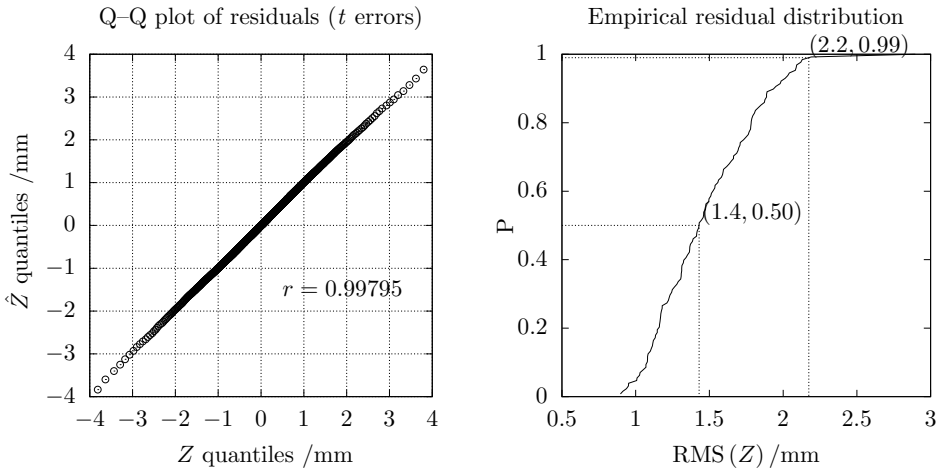

Figure 4.2: The Head-to-MRI residuals Q–Q plot (a) depicts every 100th data point of the $\hat{Z}$-quantiles over the Z-quantiles, where $\hat{\eta}$ follows the t-distribution with shape 4 and scale 1.1 mm. *The r-value is the correlation coefficient between the paired sample quantiles. The empirical distribution function of RMS of observed head-to-MRI residuals is depicted in (b).*

The smallest $D_{\tilde{\zeta}}$ was found for a *Student's* t-distribution with shape $\lambda = 4$ and scale $\tau = 1.1\,\text{mm}$ with $D_{\hat{\zeta}} = 5 \times 10^{-3} \pm 1 \times 10^{-3}$. Hence, the probability density of the error estimate $\hat{\eta}$ is expressed efficiently as

$$\pi_{\hat{\eta}}(x) \propto \left(1 + \frac{x^2}{\tau^2 \lambda}\right)^{-(\lambda+1)/2}, \tag{4.2}$$

directly proportional to a normalization constant. A ratio between the variances of errors and residuals of $\sigma_{\hat{\eta}}^2/\sigma_{\zeta}^2 = \left(\lambda\tau^2/(\lambda-2)\right)/\sigma_{\zeta}^2 = 2.87$ was found. The Q–Q plot in fig. 4.2a demonstrates the similarity between $\hat{Z}$ and Z in distribution, where $\hat{\eta}$ follows the t-distribution with shape 4 and scale 1.1 mm. Residual values of $\hat{Z}$ and Z were in the range of -4 to 4 mm, as indicated in fig. 4.2a, with approximately zero median and mean. The best fit *normal* error distribution yielded substantially worse *head-to-MRI* residuals with a Kolmogorov–Smirnov statistic of $D_{\hat{\zeta}} = 9 \times 10^{-3} \pm 7 \times 10^{-4}$. In fig. 4.2b, the distribution of observed RMS of residuals is plotted for the 128 *head-to-MRI* data sets. One RMS value is calculated over the head shape point residuals $\vec{\zeta}_n$ for each data set. An RMS of up to 2.2 mm was not exceeded for

99 % of the *head-to-MRI* data sets. The RMS values were between 0.8 to 2.9 mm, with a median of 1.4 mm.

4.2 Parameter-distribution sampling

4.2.1 MEG-to-Head and head-to-MRI

The MLEs and spreads of the coregistration parameters from the Metropolis algorithm samples were averaged over the data sets in table 4.1. The first row in table 4.1 demonstrates accurate estimates of the Metropolis algorithm with no differences compared to the least squares estimates. For the *MEG-to-head* data sets I found sample spreads of the Metropolis algorithm results of 0.6 to 0.9 mm for the scaled quaternion parameters and 0.5 mm for the translations.

The spreads of *MEG-to-head* parameters in table 4.1 are identical, up to the first decimal place, to the theoretical estimate of eq. (2.12) and eq. (2.13):

$$200\,\mathrm{mm}\cdot\sigma_\epsilon\cdot\sqrt{\mathrm{diag}\left[\left(4\sum_{m=1}^{M}\left(|\hat{\vec{b}}_m^{\mathsf{c}}|^2\boldsymbol{I}-\hat{\vec{b}}_m^{\mathsf{c}}\hat{\vec{b}}_m^{\mathsf{c}\,\mathsf{T}}\right)\right)^{-1}\right]}=\begin{pmatrix}0.8\pm0.1\\0.9\pm0.1\\0.6\end{pmatrix}\mathrm{mm}$$

$$\sigma_\epsilon/\sqrt{M}=0.5\,\mathrm{mm}\,,$$

where $\sigma_\epsilon = 1.05\,\mathrm{mm}$ and $M = 5$. The numbers on the right hand side of the equation refer to sample means and standard deviations over the 5 544 data sets. This comparison provides a quality check of the Metropolis algorithm.

The results of the sample spreads, of the *head-to-MRI* coregistration parameters in table 4.1, are similar to the results of *MEG-to-head*, with slightly larger values in the scaled quaternion part of 0.6 to 1.0 mm and smaller values in the translation part of 0.2 to 0.4 mm. Contrarily, the sample MLEs of *head-to-MRI* in table 4.1 show deviations up to several millimeters. This indicates considerable difference between the pre-registration of the ICP and the subsequent registration of the Metropolis algorithm. A mean absolute difference of the ICP compared to the Metropolis algorithm results of $(1.9 \pm 1.5)^\circ$ in the rotations and (1.1 ± 0.9) mm in translations was found. The respective paired differences of RMS of residuals were tested. According to the t-statistic, RMS computed by the Metropolis MLE were significantly smaller than RMS computed by the ICP fit with $t = 3.04$ and two-sided $p < 0.01$. However, the difference of the means was only in the order of 0.02 mm.

In order to test the correlation of RMS $(\boldsymbol{\Psi})$ and RMS of residuals, I computed these measures separately for *MEG-to-head* and *head-to-MRI* data sets. RMS $(\boldsymbol{\Psi})$

Table 4.1: Statistics of the Metropolis algorithm parameter results in mm.

MEG-to-head	$2R \cdot p_1$	$2R \cdot p_2$	$2R \cdot p_3$	s_1	s_2	s_3
MLE	0.0	0.0	0.0	0.0	0.0	0.0
Spread	0.8 ± 0.1	0.9 ± 0.1	0.6	0.5	0.5	0.5
Head-to-MRI	$2R \cdot q_1$	$2R \cdot q_2$	$2R \cdot q_3$	t_1	t_2	t_3
MLE	0.6 ± 3.3	0.4 ± 2.4	-0.2 ± 1.3	0.1 ± 0.7	-0.2 ± 1.2	0.1 ± 0.3
Spread	0.8 ± 0.3	0.9 ± 0.3	0.6 ± 0.1	0.3 ± 0.1	0.3 ± 0.1	0.2

and RMS of residuals were computed separately over coil positions of *MEG-to-head* and head shape points of *head-to-MRI*. Correlation coefficients were determined accordingly over the 5 544 and 128 data sets. Correlation coefficients of 0.017 and -0.116 for *MEG-to-head* and *head-to-MRI* were found, respectively.

4.2.2 MEG-to-MRI

126 out of the 128 *head-to-MRI* data sets have a corresponding *MEG-to-head*, taking into account the selection criteria of section 2.6.1. If more than one *MEG-to-head* data set corresponded to a given *head-to-MRI*, which occurred if more than one MEG measurement block existed for a given session, only the first *MEG-to-head* block was used. Figure 4.3 depicts the estimated RMS of TRE, denoted as $\mathrm{RMS}\,(\mathbf{\Psi})$, by the number of head shape points for these data sets.

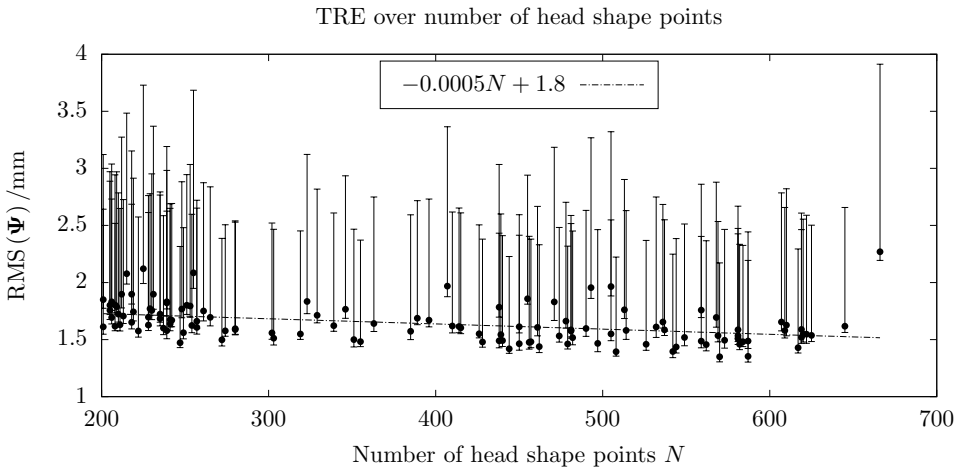

Figure 4.3: The estimated RMS (**Ψ**) *is plotted over the number of head shape points N.* **Ψ** *is computed at each head shape point. Data points indicate the mean over the samples of* RMS (**Ψ**) *and the dash-dotted line was fit to these points. The error bars show the* 50*th to* 95*th percentiles over the samples of the measure.*

The estimation of TRE is based on drawing subsamples from corresponding *MEG-to-head* and *head-to-MRI* Metropolis samples. The size of the subsamples is the effective sample size of the respective Metropolis sample. Utilizing these subsamples, the respective samples of the RMS (**Ψ**) were computed over the head shape points according to eq. (2.63). In a few cases there are multiple TRE data per head shape point numbers in fig. 4.3 due to coincidental digitization with the same number of points. The error bars reflect the range, from the median to the 95th percentile, over the samples of RMS (**Ψ**) whereas the points indicate the respective means. I regard the 95th percentile as an upper bound of the RMS (**Ψ**) confidence interval. The data sets show a mean RMS (**Ψ**) of 1.3 to 2.3 mm and an upper bound of 2.1 to 4.0 mm. Overall, both the mean and the upper bound decrease with the number of head shape points. This TRE measure serves as a quality criterion for *MEG-to-MRI* coregistrations and allows thresholding, for example, 2 mm.

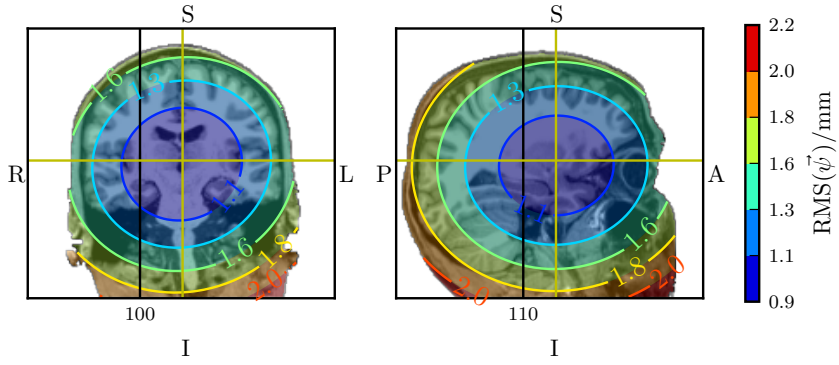

Figure 4.4: Estimates of TRE plotted as overlay onto the corresponding MRI slices. The RMS of TRE is computed for all samples of all grid points. Black lines indicate the slices in Freesurfer-MRI coordinates. The yellow crosshairs indicate the estimated minimum of TRE. In the plots, A refers to anterior, P to posterior, I to inferior, S to superior, R to right and L to left. On the left and right side, the coronal and sagittal cuts at slice 110 and 100 are plotted, respectively.

Figure 4.4 shows the estimated TRE at a fine grid on the MRI of one data set. Analogue to TRE, the coregistration rotation error is estimated by the RMS of $\sqrt{q_1^2 + q_2^2 + q_3^2}$ for the *MEG-to-MRI* rotation, which is easily sampled from the Metropolis algorithm results and does not depend on the position in space. The angular approximation of this rotation error, estimated for each subject, is between 0.8 to 1.8°, with the upper bound 95th percentile between 1.3 to 3.1°. The mean of the rotation error, across subjects, gives an angular approximation of $(1.1 \pm 0.2)°$.

4.3 Effects of coregistration uncertainties

4.3.1 Forward computation

The forward computation of a total magnetic field at the sensors is decomposed as sum of primary $\boldsymbol{b}_\infty$ and secondary $\boldsymbol{b}_{vol}$ field here. In this section, effects of coregistration uncertainties on primary, secondary and total magnetic fields are presented. The following figures show source orientations in x, y and z direction on the abscissa. The distributions are sampled over auditory, visual and somatosensory sources of 20 subjects. Standard deviations of magnetic fields (see fig. 4.5) measure the change in amplitude over the sensors. The median of the standard deviations, here over subjects and sources, is smaller for the total field compared to the primary field since primary and secondary currents are opposed to each other. For the x source orientation (from left to right) in auditory regions, the deviations of primary and

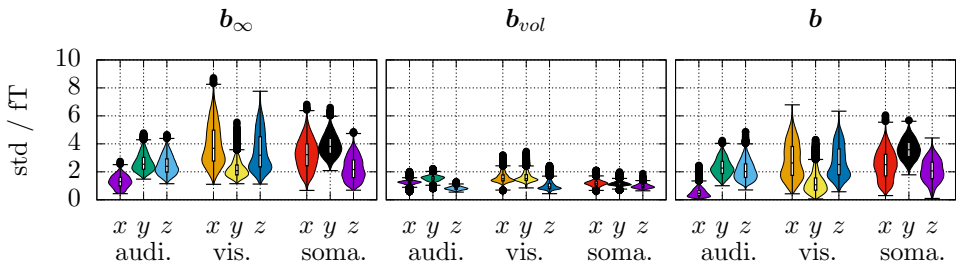

Figure 4.5: Standard deviations of magnetic fields over all magnetometers. The distributions are sampled over sources of 20 *subjects and three cortical regions. Fields are decomposed into three orthogonal source orientations (x, y and z direction). The boxes are drawn around the region between the first and third quartiles, with a horizontal line at the median value. Whiskers extend from the box to the most distant values within* 1.5 *times the interquartile range. Points that lie outside these limits are drawn separately as in black. The coloured violin plots depict the probability density of the data, smoothed by a kernel density estimator. On the abscissa of the graphs, the regions of interest, auditory, visual and somatosensory are denoted by audi., vis. and soma., respectively.*

secondary fields almost cancel each other out in the total magnetic field. This can be explained when the volume conductor is compared to a sphere with origin at (0, 0, 0) where the auditory cortex is on the x axis. In this case, a source orientation in x direction is radial and it is known from analytic solutions for spherical volume conductors that the primary and secondary field of radial sources cancel each other out outside of the sphere (Sarvas, 1987). For visual and somatosensory regions, the approximately radial orientations are y and z respectively and their suppression is confirmed in fig. 4.5. The RDMs depicted in fig. 4.6 are computed over all magnetometers. RDMs and MAGs are computed for a Gaussian sample of shifts in x, y and z, see section 3.5.4, against the reference solution at zero shift. Mean and standard deviation of RDMs and MAGs are computed over the sample of shifts. Secondary fields from sources in z orientation show the largest RDM means and standard deviations with medians of approximately 0.13 and 0.06, respectively. For the total magnetic field, RDMs have a mean and standard deviation of approximately 0.07 and 0.03. Primary and secondary fields contribute approximately equally to the RDMs of the total field.

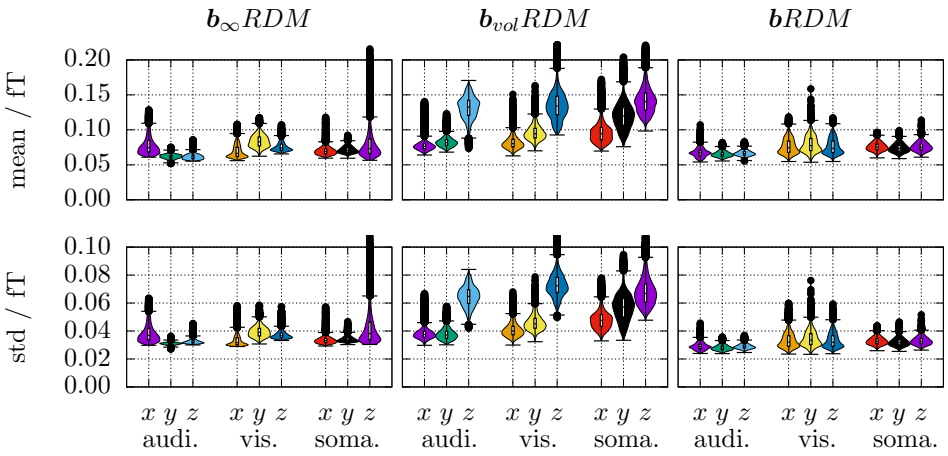

Figure 4.6: Mean (upper row) of magnetometer RDMs and corresponding standard deviation (lower row) over a sample of shift parameters. The distributions are sampled over sources of 20 *subjects and three cortical regions. The boxes are drawn around the region between the first and third quartiles, with a horizontal line at the median value. Whiskers extend from the box to the most distant values within* 1.5 *times the interquartile range. Points that lie outside these limits are drawn separately as in black. The coloured violin plots depict the probability density of the data, smoothed by a kernel density estimator. On the abscissa of the graphs, the regions of interest, auditory, visual and somatosensory are denoted by audi., vis. and soma., respectively.*

First order sensitivity indices, as defined in section 3.2.5, in fig. 4.7 reveal smaller sensitivity for the RDMs if source orientation and shift direction match. This cannot be observed for total fields of the approximately radial source orientations (auditory x, visual y and somatosensory z) because they produce small outside fields.

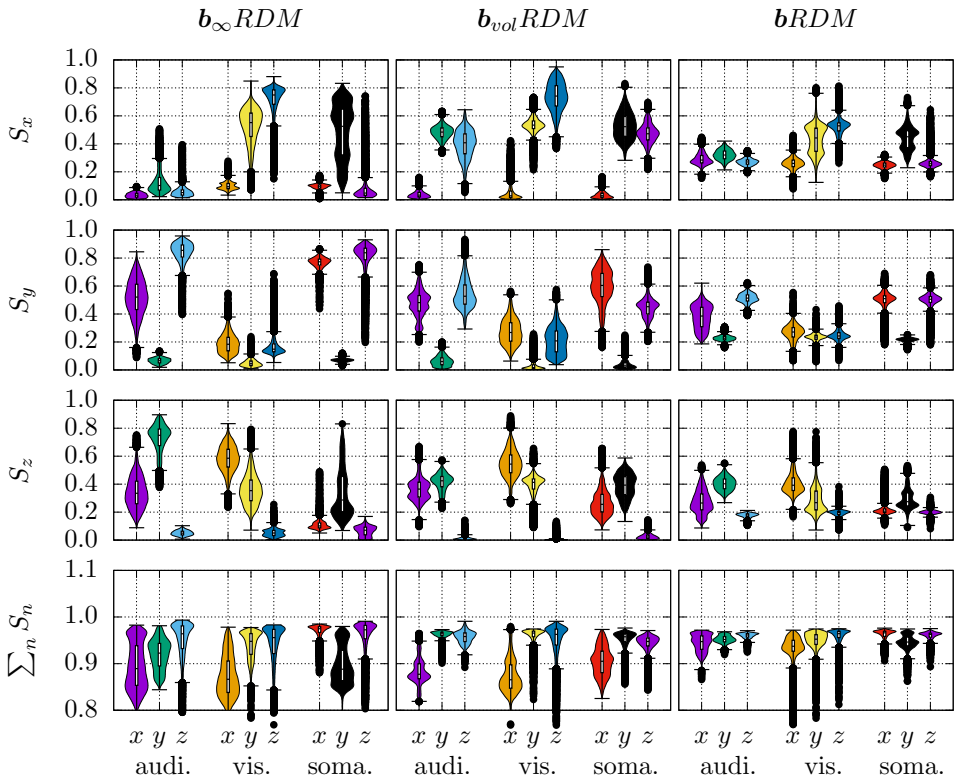

Figure 4.7: First order sensitivity indices are plotted for the RDM-function of shifts in x, y and z direction, where S_k is the index for the effect of shifts in k on the variance of the RDM. The distributions are sampled over sources of 20 *subjects and three cortical regions. The boxes are drawn around the region between the first and third quartiles, with a horizontal line at the median value. Whiskers extend from the box to the most distant values within* 1.5 *times the interquartile range. Points that lie outside these limits are drawn separately as in black. The coloured violin plots depict the probability density of the data, smoothed by a kernel density estimator. On the abscissa of the graphs, the regions of interest, auditory, visual and somatosensory are denoted by audi., vis. and soma., respectively.*

The sums of the RDM sensitivity indices in fig. 4.7 indicate that approximately 0.95 of the RDM variance can be explained by the first order indices.

Figure 4.8 depicts the means and standard deviations of magnification errors (MAGs) over the sample of shift parameters. Secondary fields from sources in z orientation show the largest MAGs with means and standard deviations distributed around 1.01 and 0.06. For the total field, MAGs have a mean and standard deviation of approximately 1.003 and 0.04.

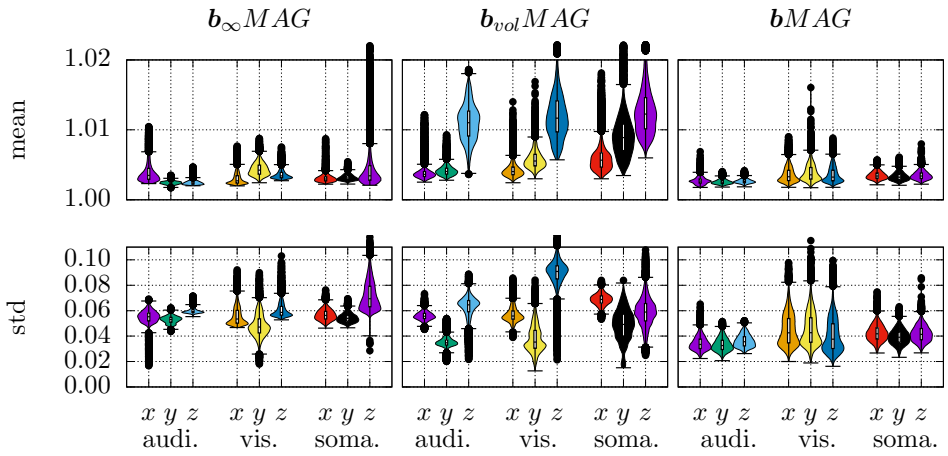

Figure 4.8: The mean (upper row) and standard deviation (lower row) of magnetometer MAGs over a sample of shift parameters. The distributions are sampled over sources of 20 *subjects and three cortical regions. The boxes are drawn around the region between the first and third quartiles, with a horizontal line at the median value. Whiskers extend from the box to the most distant values within* 1.5 *times the interquartile range. Points that lie outside these limits are drawn separately as in black. The coloured violin plots depict the probability density of the data, smoothed by a kernel density estimator. On the abscissa of the graphs, the regions of interest, auditory, visual and somatosensory are denoted by audi., vis. and soma., respectively.*

There are bigger MAGs of the total fields for visual sources (see fig. 4.8). This effect can be caused by the small distance between sensors and sources in visual regions. The subjects lean with the back of their heads on the helmet of the MEG. This head position achieves nearly minimal distances between visual sources and the sensors, which is clearly not the case for auditory (left) sources. For somatosensory (cranial) sources, small distances to the sensors can also be achieved since the subjects are told to touch the MEG helmet with the cranial part of their heads. This is also confirmed by the results of the total fields in fig. 4.8, where similar median values are found for somatosensory and visual sources.

4.3.2 Source estimates

Target registration errors

Below, results of the propagation of coregistration uncertainties to source estimates are reported for 20 subjects. The extent of the uncertainties is quantified here by

the mean RMS of the TRE, denoted as $\mathbb{E}[\mathrm{RMS}(\mathbf{\Psi})]$ as in section 3.4.3. At the head shape points a $\mathbb{E}[\mathrm{RMS}(\mathbf{\Psi})]$ of $(1.9 \pm 0.7)\,\mathrm{mm}$ (mean $\pm$ standard deviation over subjects) was found. Head movements were taken into account in this analysis.

Field topographies

The fieldmaps in fig. 4.9 (upper row) show typical forward computation magnetometer topographies of the corresponding source patches, namely the primary auditory, visual and somatosensory cortices in that order from left to right. The fieldmaps in fig. 4.9 (lower row) show three different noise levels which are later combined with the error-free forward computations of the upper row to simulate realistic scenarios. The sum of forward computation and noise results in three amplitude SNRs which are from here on refered to as small, medium and large SNR. The SNR of the visual

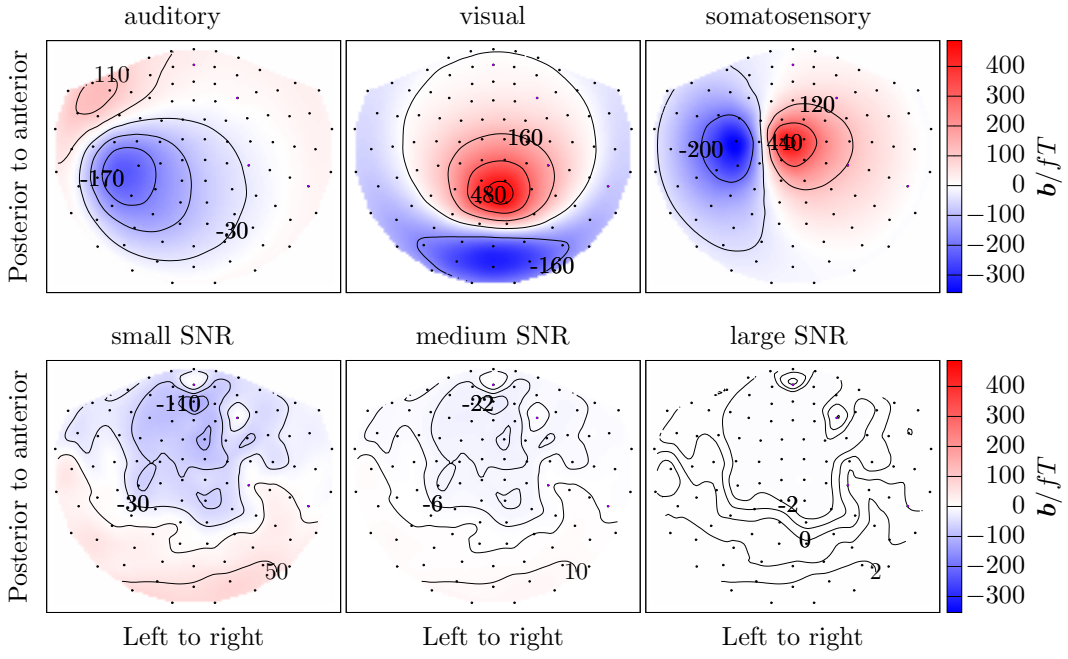

Figure 4.9: Upper row: Magnetic field topographies (forward model) of auditory, visual and somatosensory source patches. Lower row: Topographies of different noise levels - large, medium and small. Adding these noise topographies to the forward model leads to small, medium and large SNR.

and somatosensory fields is higher compared to the SNRs of the auditory fields. This

effect is caused by the distance of sources to the closest sensors, which is normally greater for the auditory source patch compared to visual and somatosensory sources. The weaker field strength for the auditory sources is already visible in fig. 4.9 (upper row).

Source amplitudes

Below, topographies in the source space are depicted on the surfaces of the regions of interest. The polynomial expansions were focused on the regions of interest and therefore the results are not available for the whole brain. Figure 4.10 shows the position and orientation of these regions in the brain. In fig. 4.11, the axes of the head coordinate system are depicted. From the polynomial expansion of sLORETA, the

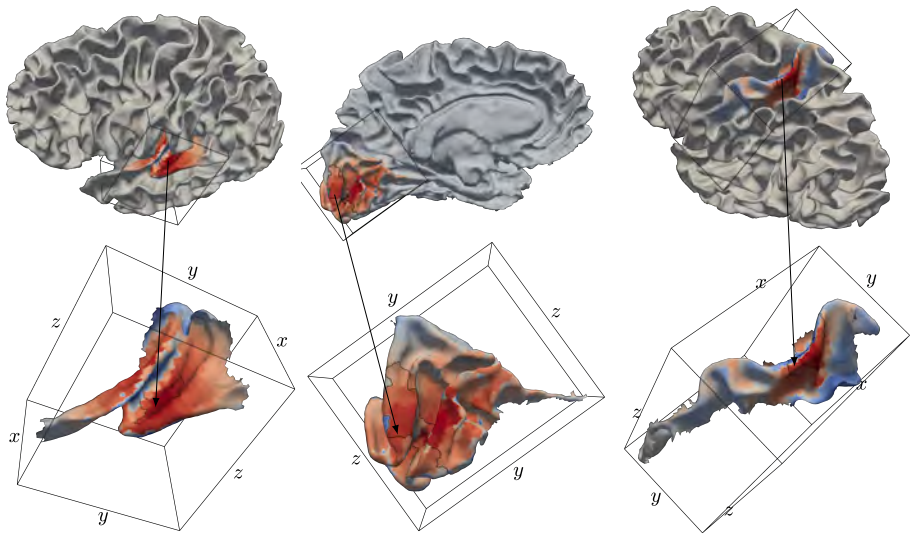

Figure 4.10: Regions of interest are encircled and zoomed in. The black border strips inside the regions of interest mark the source patches. As an example, an sLORETA source estimate is depicted in the regions of interest.

mean, mean divided by standard deviation and the sum of the first order sensitivity indices are depicted in fig. 4.12 for auditory sources. The figure shows sLORETA results for medium SNR and loose parameter of 0. Statistics are visualized for the dynamic distribution of coregistrations, see section 3.4.2 for a detailed description. The sLORETA estimate, fig. 4.12 (a), is smooth in the auditory region and the maximum is located within the source patch. Figure 4.12 (b) depicts the mean estimate devided by its standard deviation. In fig. 4.12 (c), the sum of the sLORETA

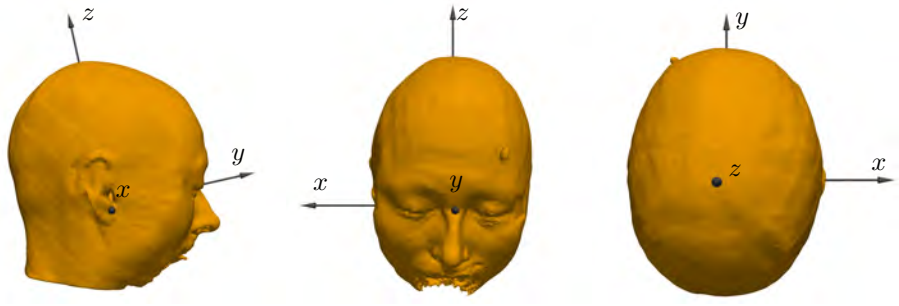

Figure 4.11: The head coordinate system is depicted for one subject from three viewpoints. From left to right, the images show sagittal, coronal and axial views. The coordinate system can be described by its axes orientations as right (x), anterior (y) and superior (z). In the figures below, axes are always aligned in this coordinate system.

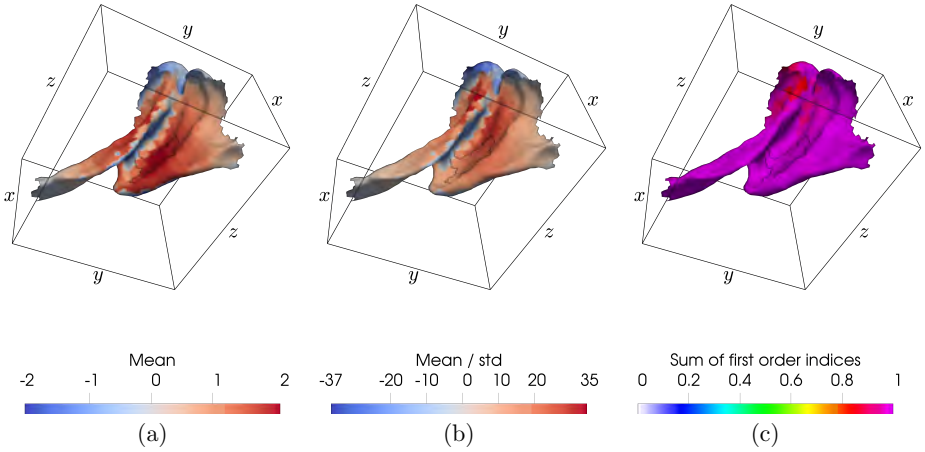

Figure 4.12: (a) Mean sLORETA estimate for the auditory region. The mean was computed over the distribution of sLORETA estimates. Positive (red) and negative (blue) values reveal outward and inward oriented sources on the white matter (source space) triangulation, respectively.
(b) Estimate of (a) divided by the corresponding standard deviation.
(c) Total first order sensitivity index of the auditory region. The total first order sensitivity index is computed as the sum over six coregistration indices. This total indicex sums up to values not greater than one.
The renderings are shaded, which results in darker colours in some regions.

first order sensitivity indices is depicted. This sum is the normalized fraction of the source amplitude variance which can be traced back to first order effects, that is to each coregistration parameter alone. The difference of one minus that fraction is explained by higher order interactions of these parameters. Here, outside of the source patch at least 80% of the variance and within the patch more than 90% is explained by first order effects. Figure 4.13 shows all sLORETA first order sensitivity indices in the auditory region. The rotation and shift indices are depicted for the axes x, y and z from left to right in the upper and lower row, respectively.

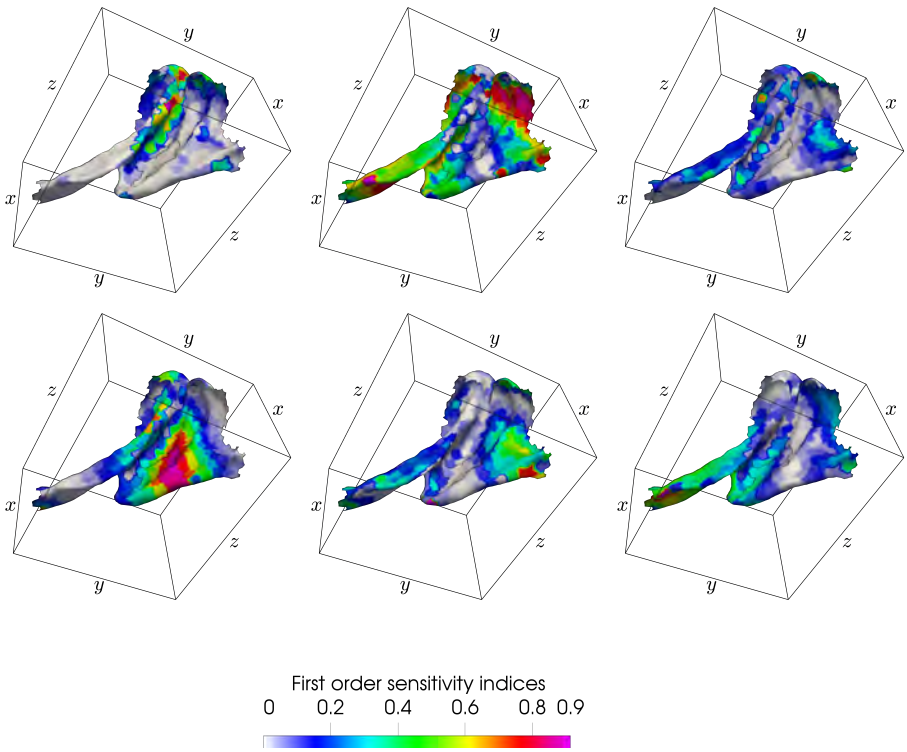

Figure 4.13: First order sensitiviy indices of the sLORETA estimate are depicted for each coregistration parameter in the auditory region. In the upper row the indices of rotation parameters are shown for rotation axes x, y and z from left to right. The lower row shows the indices of shift parameters in x, y and z from left to right. All indices are normalized on each source position separately. The indices are computed from the coefficients of the polynomial expansion.

A profound assessment of the results in fig. 4.13 is only possible when the results of fig. 4.12 are taken into account. Within the auditory source patch and in its vicinity, more than 90 % of the variance is explained by the first order effects, see

fig. 4.12 (c). Hence, the first order sensitivity indices in fig. 4.13 provide detailed information about the main source of variance. The sum of the 6 topographies in fig. 4.13 yields fig. 4.12 (c). Since the sensitivity indices are normalized, it is important to take a look at the topography of the absolute variance. Additionally, only regions with large source activity are of interest here. Both, information about the variance and the source activity is encoded in fig. 4.12 (a) and (b). The region of large source activity is in the vicinity of the source patch where source orientations are similar to the patch, see fig. 4.12 (a). Source location with large absolute values in fig. 4.12 (a) and small absolute values in fig. 4.12 (b) are locations with large variance, this is the case for the source patch, especially for the shallow part (closer to the sensors) of the source patch. Within the source patch, highest sensitivity indices are found for the shift in x, with a maximum value of approximately 0.9, see fig. 4.13. This can be explained by the relation of auditory sources and the closest sensors where only a shift in x direction changes the distance of sources to sensors effectively. The other parameters move the sources approximately parallel to the sensors. The triangular topography of the x-shift sensitivity index converges in the deeper region of the auditory cortex. That is the expected result, since the shallow sources are more affected by a change in distance between sources and sensors.

Source amplitude maximum distribution

By using polynomial expansions of the beamformer and sLORETA operators, the amplitude maximum of source estimates was efficiently sampled for different coregistrations. The sample of coregistration parameters follows the assessment of *MEG-to-MRI* as described in section 3.4.1. Standard deviations of the spatial maximum distribution were computed for the three main axes as singular values and denoted as σ_1, σ_2 and σ_3. Figure 4.14 shows these maximum location standard deviations in the shape of an ellipsoid for the auditory, visual and somatosensory regions. The probabilities of the maximum location are colour-coded at the cortical surface. This figure (4.14) is an example for the sLORETA maximum distributions of one subject with a medium SNR and the loose parameter set to 0. Localization errors were computed as spatial differences between the maximum of a source estimate and the mean location of the associated source patch. The absolute means over these differences for the coregistration sample are denoted by δ_x, δ_y, δ_z in fig. 4.15 and fig. 4.16 for a loose parameter of 0 and 0.2, respectively. In fig. 4.14 the mean maximum location is at the center of the ellipsoids. Details about the computation of the δ-values are described in section 3.6.6. For a loose parameter of 0, beamformer and sLORETA had similar localization errors with media δ-values up to 5 mm on each axis. The

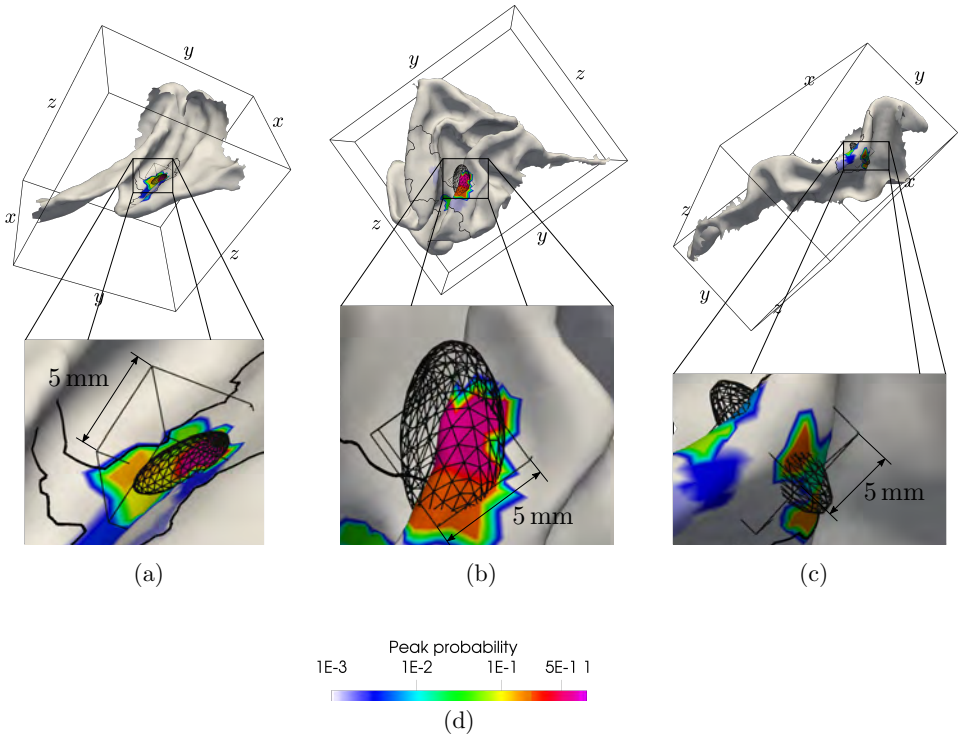

Figure 4.14: SLORETA maximum location probability plotted for the auditory, visual and somatosensory region (a), (b) and (c) respectively. Medium SNR and a loose parameter set to 0 *were used. The maximum location probability is colour-coded according to the colourbar in (d). The wire frame ellipsoids depict the standard deviations at the main axes of the probability distribution, centred at the mean location. A wire frame cube with side length* 5 mm*, aligned in* x*,* y *and* z *is placed at the location of the ellipsoid as a spatial reference.*

smallest localization errors were achieved in auditory regions, especially for medium SNR where all errors were below 5 mm. For a loose parameter of 0.2, the beamformer had larger localization errors compared to a loose parameter of 0. Especially in auditory regions, the differences are large, for example median δ-values of between 5 to 10 mm were found for the x-axis. SLORETA had very similar localization errors for loose parameters of 0 and 0.2.

Figures 4.17 and 4.18 depict spatial standard deviations of maximum locations of 20 subjects with different SNRs and loose parameters. In these figures, σ_1, σ_2, σ_3 denote the main axes of the maximum distribution ellipsoids, as described in section 3.6.6. The strongest effect of coregistration uncertainties is observed in

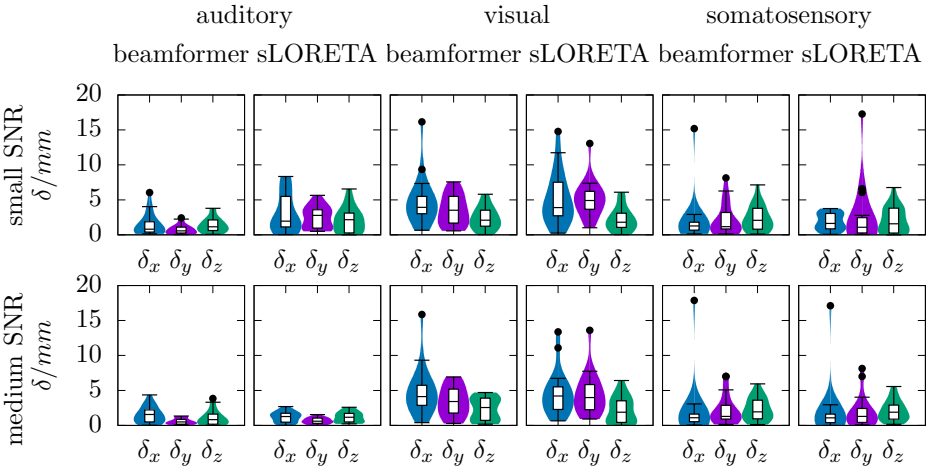

Figure 4.15: Violine plots of localization errors in auditory, visual and somatosensory regions for small and medium SNRs and loose parameter of 0. *The distributions are sampled over* 20 *subjects. Boxes are drawn around the region between the first and third quartiles, with a horizontal line at the median value. Whiskers extend from the box to the most distant values within* 1.5 *times the interquartile range. Points that lie outside these limits are drawn separately as in black. The coloured violin plots depict the probability density of the data, smoothed by a kernel density estimator.*

beamformer estimates with loose parameter set to 0.2. Here, median values of approximately 4 mm to 7 mm are obtained for the maximum location standard deviation on the first main axis (σ_1). The sLORETA results show almost no difference between loose parameters set to 0 or set to 0.2. For a loose parameter of 0, the beamformer and sLORETA results are similar, with a median σ_1 value between 2 and 4 mm. Different SNRs values have resulted in small changes of maximum dis-

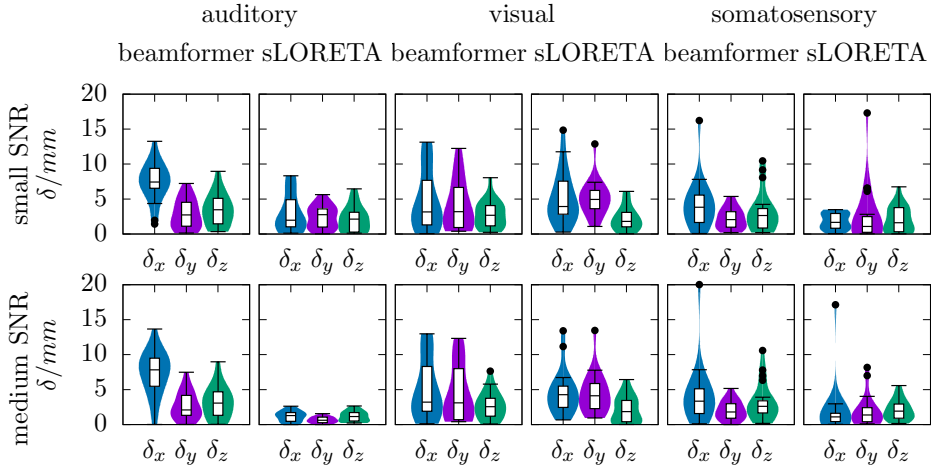

Figure 4.16: Violine plots of localization errors in auditory, visual and somatosensory regions for small and medium SNRs and loose parameter of 0.2. *See fig. 4.15 for details on statistics, boxes and violin plots.*

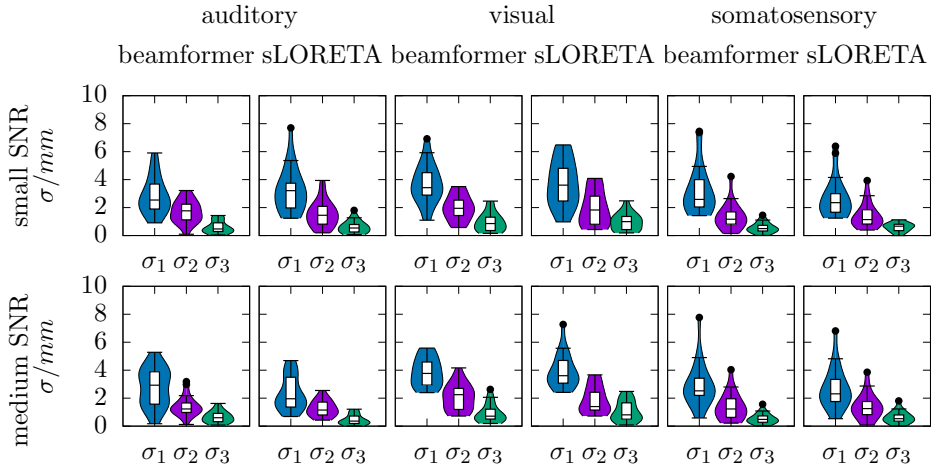

Figure 4.17: Violine plots of maximum location statistics in auditory, visual and somatosensory regions for small and medium SNRs and loose parameter of 0. *See fig. 4.15 for details on statistics, boxes and violin plots.*

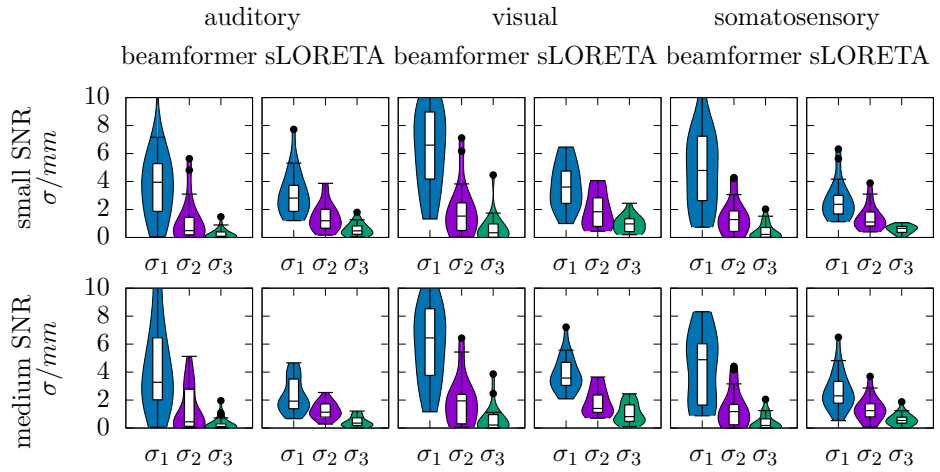

Figure 4.18: Violine plots of maximum locatioon distribution statistics in auditory, visual and somatosensory regions for small and medium SNRs and loose parameter of 0.2. *See fig. 4.15 for details on statistics, boxes and violin plots.*

tributions only. The beamformer results with loose parameter of 0 tend to yield smaller σ_1 for small SNR compared to medium SNR. Higher than medium SNR do not result in further improvements with respect to coregistration uncertainties.

4.3.3 Error estimates

Error estimates of the polynomial expansions were conducted, following the procedure of Weise et al. (2015). For this purpose, 1 000 evaluations of the polynomial expansion were compared against exact computations of the beamformer and sLORETA solutions in the regions of interest. For one subject, errors of a beamformer estimate are depicted on the regions of interest in fig. 4.19. The topographies of fig. 4.19 (a), (b) and (c) reveal the spiky characteristic of the relative error measure and care must be taken by interpreting the results. Large relative errors can occur where the variance of the source estimates, due to coregistration uncertainties, is small. The relative error measure was used in this thesis in order to compare the results to Weise et al. (2015). Below the average over the regions of interest is computed to obtain a global error measure for the regions. Figure 4.20 depicts error statistics from 20 subjects for different SNRs, loose parameters and regions of interest. The sLORETA errors are considerably larger than the beamformer errors. Largest errors are observed in the visual and auditory regions while the errors in

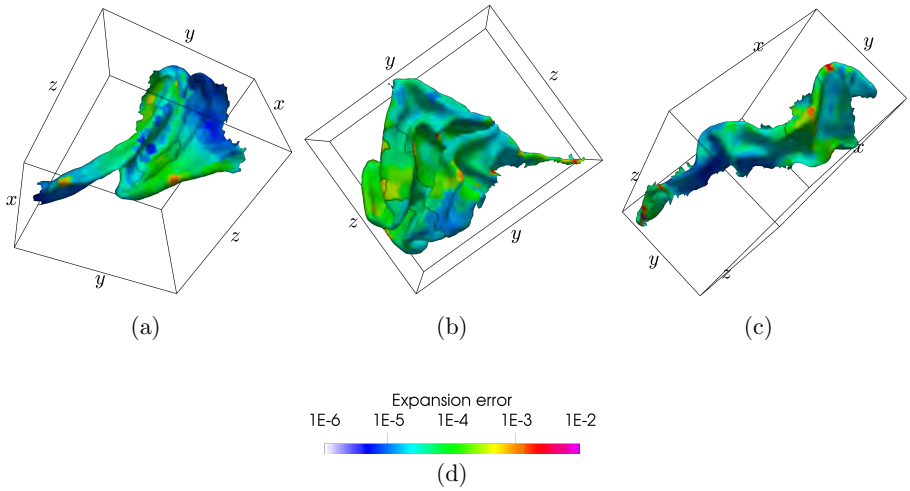

Figure 4.19: Error of the polynomial expansion of the beamformer estimate compared to exact solutions shown for the auditory (a), visual (b) and somatosensory (c) region. The values decode the relative error measure $\frac{\left|\boldsymbol{p}(\vec{r},\boldsymbol{X})-\hat{\boldsymbol{p}}(\vec{r},\boldsymbol{X})\right|}{\left|\boldsymbol{p}(\vec{r},\boldsymbol{X})-\mathbb{E}[\boldsymbol{p}(\vec{r},\boldsymbol{X})]\right|}$*. In the statistics below, the means of this measure over the regions of interest are reported (see eq.* (3.34)*). Medium SNR and a loose parameter set to* 0 *were used.*

somatosensory regions are clearly smaller. Overall, the third quartiles of the errors are not greater than 0.005. Small SNR causes larger sLORETA errors compared to medium SNR. The beamformer expansion errors were larger when setting the loose parameter to 0.2 compared to 0. Larger SNRs are not depicted in the figures because the results were almost identical to medium SNR. Weise et al. (2015) found relative errors between 0.1 to 1 % for three inputs and an order 7 polynomial expansion. They used the order 7 polynomial expansion as reference and found errors of the derived statistics, namely mean, standard deviation and derivative-based sensitivity indices below 1 % for an order 4 polynomial expansion. The errors of the statistics of the order 4 polynomial expansion were interpreted as acceptable. They also reported relative errors of the 4 polynomial expansion of approximately 3 %. In this thesis, order 6 polynomial expansions were used and maximal relative errors of 1.8 % were found for the sLORETA estimate in visual regions for medium SNR.

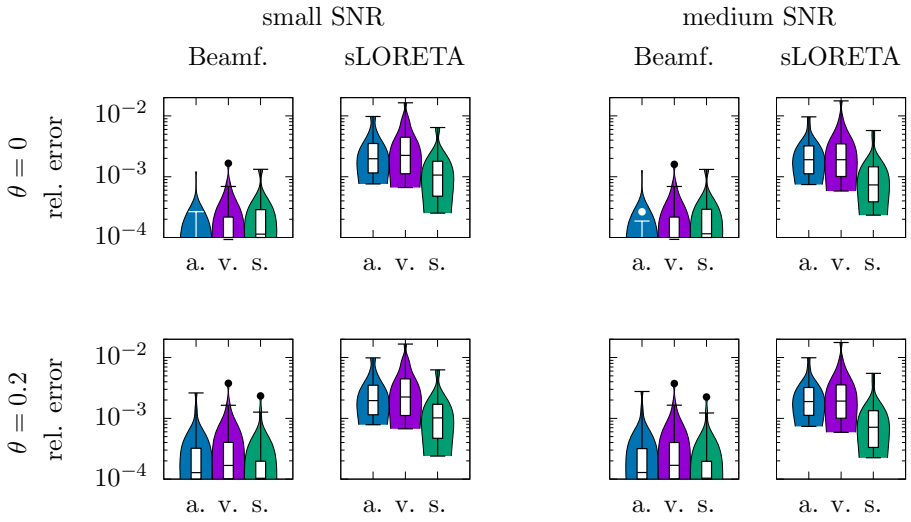

Figure 4.20: Statistics of the relative error measure eq. (3.34) *over* 20 *subjects for loose parameters of* 0 *and* 0.2 *in the upper and lower row, respectively. On the abscissa of the graphs, the regions of interest, auditory, visual and somatosensory are denoted by a., v. and s., respectively. Boxes are drawn around the region between the first and third quartiles, with a horizontal line at the median value. Whiskers extend from the box to the most distant values within* 1.5 *times the interquartile range. Points that lie outside these limits are drawn separately as in black. The coloured violin plots depict the probability density of the data, smoothed by a kernel density estimator.*

Chapter 5

Discussion and conclusions

5.1 Quality assessment of MEG-to-MRI coregistrations

5.1.1 Findings

Using an adaptive Metropolis algorithm to sample the six-dimensional coregistration parameter space, and subsequent MLE, I was able to confirm the results of the least squares approach to *MEG-to-head* coregistrations and further, to improve the results of the ICP algorithm for *head-to-MRI* coregistrations. Interestingly, the Metropolis algorithm provides parameter sets with ergodic properties that allow estimating confidence intervals of the coregistration parameters. Target registration error (TRE), for instance, is a function of the coregistration parameters at any point in space. Statistical indices of TRE can be derived via the proposed Metropolis sampling.

I found that it is possible to approximate the empirical distributions of residuals in *MEG-to-head* and *head-to-MRI* coregistrations by replacing the point errors with samples from *normal* and *Student's t*-distributions, respectively. The empirical distributions indicated that 99 % of the data sets yielded RMS of residuals not larger than 2.5 mm for *MEG-to-head* and 2.2 mm for *head-to-MRI* coregistrations. Thus, dependent on the MEG lab, RMS values larger than these thresholds may indicate a problem in the measurement procedure. However, this provides only a preliminary assessment where the given thresholds are exceeded in about 1 % of the data sets. Further, RMS of residuals are not well suited as a quality measure for coregistration, as they do not correlate with the actual errors i.e. TRE (Fitzpatrick, 2009). This was confirmed in the present study where very small correlation coefficients, of 0.017 and −0.116, were observed over the 5 544 *MEG-to-head* and 128 *head-to-MRI* data sets. An adaptive Metropolis algorithm was used to sample the probability density of

the coregistration parameters for each data set. For the *MEG-to-head* data sets, the MLEs of the Metropolis algorithm were equal to the least squares estimates. This was the expected result as I used the probability density of a *normal* distribution for the errors and in this case the least squares estimate is equal to the MLE (Press et al., 1992, equation 15.1.3). For the *head-to-MRI* data sets, the Metropolis algorithm computed different MLE coregistration parameters compared to the ICP algorithm. RMS of residuals were significantly reduced by the Metropolis algorithm compared to the ICP. This may be explained by the fact that the ICP algorithm finds a local minimum dependent on the initial state of the iteration (Besl and McKay, 1992). Optimizations of the *head-to-MRI* coregistration have to deal with the difficulty that the underlying data of both modalities does not match, only a subset of points of one modality matches points of the other. Such optimizations depend on both the initial rotation and translation, and are also referred to as local shape-matching (Besl and McKay, 1992). And although Besl and McKay (1992) propose sampling the initial rotation and translation parameters for the local shape matching using the ICP algorithm, this method is not common practice in MEG labs, nor is it implemented in commonly used packages such as *MNE* or *mne-python*. Compared to ICP, the Metropolis algorithm searches more globally and it is less dependent on its initial state. Samples can be drawn from the complete parameter distribution. Variance and higher moments can be estimated from the Metropolis samples because of the correct ergodic properties (Haario, Saksman, and Tamminen, 2001). However, these advantages are achieved at much higher computational costs compared to ICP. A standard desktop computer (random-access memory (RAM): 15.58 gigabyte (GB), MIPS Technologies, Incorporation (MIPS): 4x6 784, central processing units (CPUs): Core trademark (TM) i7-2600K 3.40 GHz) takes approximately 50 minutes of computation to run a *head-to-MRI* Metropolis algorithm with 296 500 steps (593 head shape points).

For the translation parameter estimates, the *head-to-MRI* yielded smaller variances compared to the *MEG-to-head* coregistrations. The high accuracy of the *head-to-MRI* translation parameters can be explained by the larger number of data points compared to the *MEG-to-head* coregistrations. Interestingly, rotation parameters were similar between *MEG-to-head* and *head-to-MRI*. This may be explained by the spherical nature of the head; spheres are rotation invariant in the *head-to-MRI* coregistration problem.

For the investigated data sets, an average RMS of TRE at the head surface of 1.7 mm was observed. An average RMS of the rotation errors of 1.1° was found, which was well predicted by the root of the sum over the squared quaternion spreads

from table 4.1. Hillebrand and Barnes (2003) found a TRE threshold of 2 mm at the cortical surface for anatomically constrained beamformers. They suggest that the use of anatomical constraints with beamformers is only beneficial if the *MEG-to-MRI* coregistration and segmentation errors are smaller than 2 mm and 10° at the cortex. This result was later confirmed by Hillebrand and Barnes (2011) for the estimation of the source extent. The findings of this thesis showed, on average, a smaller TRE than the critical 2 mm value reported by Hillebrand and Barnes (2003) and Hillebrand and Barnes (2011), but 2 mm was still completely within the range of the TRE distributions. However, with respect to rotations, the results of this thesis were consistently below the critical threshold of 10°. I found an upper 95th percentile of the coregistration rotation error of 3.1° at maximum. That is, the measurements described in this thesis are sufficiently accurate to practically avoid rotation errors greater than 4°. On the other hand do orientations of the cortical surface also depend on the segmentation, which may result in source orientation errors in the order of 10°. In contrast to Hillebrand and Barnes (2003) and Hillebrand and Barnes (2011), I did not assess TRE at the cortical surface but at head shape points because of the availability of this surface without conducting further segmentation. However, using the Metropolis sampling of the coregistration parameters, I am able to compute TRE at any point in space. For source reconstruction, TRE can be estimated at various points of interest in the source space or at the entire cortical surface. For example, fig. 4.4 shows TRE computed on a coronal and sagittal slice. The sagittal grid on the right side of the figure shows a small TRE in frontal regions of the brain. These regions were close to the centre of the coil positions, where the *MEG-to-head* produces the smallest TRE, and also close to the face, where the digitization provides more specific coregistration information compared to occipital regions.

Several studies have addressed the improvement in coregistration error stemming from particular measurement steps. Singh et al. (1997) aimed to reduce the fiducial localization error effects using a bite bar. They evaluated their strategy using Monte Carlo simulations and were able to substantially improve the stability of their coregistrations, in comparison to the pure fiducial-based method. At the time of Singh et al. (1997), tracking of head position and rotation, during head shape digitization, had not been established and, thus, the bite bar was essential to stabilise the head relative to the digitization reference. A similar bite bar system was also proposed by Adjamian et al. (2004) which, reduced the fiducial localization error by approximately a factor of two. They also reported that the bite bar can cause discomfort and introduces artifacts for some subjects. In the laboratory, coils are placed freely on the anterior, upper part of the subject's head surface, independent of anatom-

ical landmarks. To compensate for head movement during 3D-digitization, head position and rotation are tracked using an additional reference, mounted on special glasses, which is common practice in present day MEG laboratories. No additional mechanical hardware, for example, bite bars or individual head casts, are used to restrict the movement of the subject's head. The methods of assessing coregistration errors suggested in the current report are not affected by mechanical hardware, although, if individual head casts are used a different approach for the assessment of the *head-to-MRI* coregistration is needed. Meyer et al. (2017) suggested the use of head casts that fit to the reconstructed surface of the MRI of individual subjects. They estimated a maximal coregistration error of 1.2 mm by using such head casts. Depending on the shape of the subjects head, there was some flexibility in the positioning of the head, relative to the cast, which was tracked by a reference coil on the subject's nose, in addition to the coils in the cast. They report a predominant uncertainty of about 1.2 mm standard deviation of the head position relative to the cast in the z-axis (superiorly oriented head coordinate). However, potential movement of the subject's head, in a head cast, presents a problem that was not addressed by the assessments of this thesis.

Besides coregistration, head movement during data acquisition or between measurement blocks are related sources of error in MEG source reconstructions. Uutela, Taulu, and Hämäläinen (2001) compared two methods, a correction of sensor signals by alignment of minimum norm estimates and a correction of forward calculations. They found that both methods can efficiently reduce the effect of head movement in typical MEG studies. Later, an alternative method of sensor signal correction, based on multipole expansions, was proposed by Taulu and Kajola (2005) which is nowadays widely used with *Neuromag* devices. All of these methods rely on the accurate estimation of head positions during the MEG measurement. Hence, their accuracy is intrinsically limited by the error of *MEG-to-head* coregistrations. The magnitude of head movements is often greater than the errors of *MEG-to-head* coregistrations especially between measurement blocks and in studies with children. For example, Wehner et al. (2008) reported an average head position displacement of 12 mm from the beginning to the end of the experiment. Compared to other sources of error, such as sensor noise and head movement, the *MEG-to-MRI* coregistration error provides an absolute limit to the accuracy of source localization, which, cannot be reduced by longer measurements or sophisticated head movement corrections.

5.1.2 Practical recommendations

To facilitate a straightforward implementation of the proposed Metropolis algorithm for *head-to-MRI* coregistration in different laboratories, I recommend the estimation of error variance from the residuals according to the ratio $\sigma_{\hat{\eta}}^2/\sigma_{\zeta}^2 = 2.87 \approx 3$, which was found in the present study. For the acquisition of σ_{ζ}^2, I suggest the use of existing procedures from the respective laboratories (e.g. the ICP). From this starting point, the estimation of error variance can be validated by error simulations and subsequent head shape matchings. I recommend starting with variations of *normal* or *Student's* t-distributions. As soon as a theoretical error distribution is found, with satisfying Kolmogorov–Smirnov statistics and a satisfying Q–Q plot of simulated and observed residuals, Metropolis sampling of the log-likelihood eq. (2.59) can be started. For *MEG-to-head* coregistration the Metropolis algorithm is not required in the case of approximately *normally* distributed errors, of similar size as reported in the present study. Assuming the latter conditions are met, parameter samples of *MEG-to-head* can be generated by using $\sigma_{\epsilon}^2 \cdot \left(\boldsymbol{J}^{\mathsf{T}}\boldsymbol{J}\right)^{-1}$ of eq. (2.11) as the covariance matrix and a standard *normal* random number generator. The *MEG-to-head* error variance σ_{ϵ}^2 can be estimated from residuals as $\sigma_{\epsilon}^2 = \sigma_{\delta}^2 M/(M-2)$. This is the theoretical ratio for linear least squares fits (Björck, 2015, page 214) of rotation and translation parameters, where M is the number of coils. Optimal coregistration parameters are found in closed form for *MEG-to-head* and from the maximum likelihood estimate of the Metropolis sample for *head-to-MRI*. For corresponding parameter samples of *MEG-to-head* and *head-to-MRI*, TRE is estimated by computation of eq. (2.61), eq. (2.62) and eq. (2.63).

For the digitization of the *head-to-MRI* data sets a large number of head shape points was used and facial features, (e.g. bridge of nose) were emphasized. Hence, it is difficult to determine the exact contributions, to TRE, of the sheer number of points involved and the number of facial features used. Taking into account the spatial distribution of TRE, in fig. 4.4, I suggest it might also be beneficial to acquire more head shape points in areas with the highest errors, such as the inion, which tends to have unique spatial features. A similar argument can be made for coil placement. The hair complicates the attachment of the coils at occipital regions, which is the reason for a more frontal coil placement in the laboratory. If possible, I recommend attaching at least one coil to an occipital location. I recommend using a large number of head shape points, about 600 yielded the smallest TRE in the current study, emphasis on facial features as well as the inion. However, the sheer number of head shape points is not a guarantee for good coregistration. As seen in fig. 4.3, the largest number of head shape points resulted, accidentally, in the

largest TRE. Therefore, and in agreement with Hillebrand and Barnes (2003) and Hillebrand and Barnes (2011), I recommend checking that the mean RMS of TRE is not greater than 2 mm at the head surface.

Computations of TRE, like in fig. 4.4, are useful for coil placement and head shape digitization optimizations in EEG applications as well. For example, for accurate reconstructions of brain activity in the visual cortex it is beneficial to refine the head shape digitization at occipital regions. In this case, TRE at the visual cortex is the measure of interest. Coregistrations for EEG only involve the *head-to-MRI* problem although head shape digitization is more challenging due to the electrode cap, compared to the MEG procedure. As a result of the electrode cap, the number of head shape points is usually smaller in the EEG coregistration compared to the equivalent procedure in MEG. For this reason, the uncertainties of the fit are likely to be higher for EEG compared to the results of the present study. I believe that the availability of TRE at regions of interest would be useful for the digitization optimization in EEG.

5.1.3 Conclusion

Quality assessment of *MEG-to-MRI* coregistrations can be achieved by using the Metropolis sampling algorithm of the coregistration parameters and subsequently evaluating TRE. Further, I propose establishing this assessment procedure in EEG and MEG laboratories and suggest reporting TRE in the study publications, especially if source estimates are reported. I recommend the application of the Metropolis algorithm to achieve higher accuracy when estimating the parameters of the *head-to-MRI* problem. Due to the superior results compared to the ICP, and the availability of parameter distribution samples and derived measures like TRE, I suggest the Metropolis algorithm also for EEG coregistration fits.

5.2 Effects of coregistration uncertainty on forward computations

The BEM forward computations were decomposed into primary and secondary fields. Both components produce magnetic field standard deviations in the same order of magnitude, for example between approximately 1 and 4 fT for auditory sources of 1 nA m. The effect of coregistration on topography and amplitude changes is similar between primary and secondary fields.

For the total magnetic field, a Gaussian coregistration uncertainty with standard deviation of 2 mm in each axis relates to median RDMs and MAGs of approximately 0.07 ± 0.02 and 1.00 ± 0.04, respectively.

The RDMs are less sensitive to a shift along the direction of the source orientation compared to orthogonal shifts. This can be explained by the relation of source orientation and sensor topography. A source orientation parallel to the y-axis is related to a magnetic field zero-crossing along the y-axis and a small shift in y produces a smaller difference in topography than shifts in x or z, because the strongest gradient is parallel to x and x-shifts move the topography along this gradiant while z-shifts modify it. In a similar setup, Zetter et al. (2018) investigated the effect of coregistration uncertainties on forward computations and source reconstructions for on-scalp MEG (by simulating optically pumped magnetometers). As opposed to this thesis, their translation uncertainties were added independently to each sensor position. They sampled their translation uncertainties from uniform distributions within centered spheres. For different error levels, the radii of the spheres were defined according to their RMS position errors of 2, 4 and 6 mm. Their error level of 2 mm RMS is most comparable to the uncertainties observed and discussed in this thesis. For this error level, they found a mean correlation coefficent (CC) of 0.997 in sensor topographies for shallow sources. The CC is defined as

$$CC = \frac{(\boldsymbol{b} - \mathbb{E}[\boldsymbol{b}]) \cdot \left(\hat{\boldsymbol{b}} - \mathbb{E}[\hat{\boldsymbol{b}}]\right)^{\mathsf{T}}}{\left|\boldsymbol{b} - \mathbb{E}[\boldsymbol{b}]\right| \cdot \left|\hat{\boldsymbol{b}} - \mathbb{E}[\hat{\boldsymbol{b}}]\right|}, \tag{5.1}$$

where $\boldsymbol{b}$ is the reference topography and $\hat{\boldsymbol{b}}$ is the topography from the displaced sensors. It follows from the definition of the RDM that $RDM^2 \approx 2\,(1 - CC)$. This is a good conversion if the means over the topographies are small compared their standard deviations and it converges when the means approach zero. Hence, Zetter et al. (2018) have found an RDM of 0.077 transforming their ($CC = 0.997$), which is in fine agreement with the results of this thesis (median RDMs of 0.07 ± 0.02).

MAGs depend mainly on the distance between sources and sensors and hence larger MAGs are found for visual and somatosensory sources compared to auditory sources. The reported mean MAGs were always greater than 1. This result is explained by the distribution of the $1/r^2$ characteristic of the magnetic field amplitude, where r is the distance between source and sensor. The mean of two MAGs resulting from an increase and decrease of the distance by δ_r is

$$\frac{r^2}{2\left(r-\delta_r\right)^2}+\frac{r^2}{2\left(r+\delta_r\right)^2}=\frac{r^2\left(r+\delta_r\right)^2+r^2\left(r-\delta_r\right)^2}{2\left(r^2-\delta_r^2\right)^2}=\frac{r^2\left(2r^2+2\delta_r^2\right)}{2\left(r^2-\delta_r^2\right)^2},$$

where the first fraction on the left hand side is expanded by $\left(r+\delta_r\right)^2$ and the second one by $\left(r-\delta_r\right)^2$. The result is obviously greater than 1 for $\delta_r^2 < 3r^2$. Hence, for symmetrical distributions of reasonably small increases and decreases of the distance between sources and sensors, the mean MAG is greater than one.

By using polynomial expansions of the BEM forward computation, the computation time was reduced by a factor of approximately 40 compared to sheer Monte Carlo sampling on a standard desktop machine (RAM: 15.58 GB, MIPS: 4x6 784, CPUs: Core TM i7-2600K 3.40 GHz). However, the BEM computation is already very efficient for different coregistrations because only the surface integrals over the precomputed potentials at the boundary surfaces add a computational burden. When FEM forward computations are involved, the computation of the magnetic field for different coregistrations is computationally more expensive. Hence, polynomial expansions of FEM computations can achieve a higher speed up here compared to BEM.

From the forward computation results, it can be concluded:

1. It is not possible to accurately approximate the coregistration effects by using primary or secondary fields alone.

2. The effects of coregistration uncertainty on RDMs are small and hence, only small effects on source localization errors are expected.

3. The effects on MAGs are very small and only affect the amplitudes, not the topographies, in the source space.

4. BEM forward computations are efficient for different coregistrations and polynomial expansions reduced computation times by a factor of approximately 40.

5.3 Effects of coregistration uncertainty on source estimates

The propagation of coregistration uncertainty to source estimates was performed by using Smolyak pseudospectral approximations of beamformer and sLORETA. This approach was tested for auditory, visual and somatosensory brain activity with different SNRs and loose parameters on datasets of 20 subjects. The mean RMS of TRE at the head shape points of these subjects was (1.9 ± 0.7) mm (mean $\pm$ standard deviation over subjects). By using pseudospectral approximations as efficient surrogates of inverse operators, the distribution of the source estimate maximum was sampled for 50 000 coregistrations. For this purpose, the sampling of coregistrations was built on the results of the assessment part of this thesis. The efficient polynomial surrogate of the source estimates reduced the computation times by a factor of either approximately 10 000 for beamformer or approximately 50 000 for sLORETA compared to the exact reference computations. These large reductions of computation times are possible because the computation of forward solutions plus whitening, SVD, noise normalization et cetera were replaced by polynomial evaluation and a matrix product. The size of the matrices is the number of polynomials in the expansion (here 377) times the number of sources in the region of interest (here between hundred and thousand) times 3 (for dipole triplets). The greater reduction of the sLORETA compared to the beamformer can be explained by the fact that sloreta is based on the entire source space. In contrary, the beamformer can be computed for each source independently, which is beneficial when only regions of interest are analyzed. The computation times were estimated from 1 000 evaluations on a standard desktop machine (RAM: 15.58 GB, MIPS: 4x6 784, CPUs: Core TM i7-2600K 3.40 GHz).

The approximation errors had in the worst case (sLORETA in visual regions) an upper 95 percentile of less than 1 % which indicates high accuracy (Weise et al., 2015). Compared to sLORETA, the beamformer approximation errors are clearly smaller. This is due to the lesser degrees of freedom for the beamformer compared to sLORETA. SLORETA includes a coupling of different sources in its pseudoinverse which may result in higher order polynomial terms.

By using the polynomial expansion coefficients of source estimates, statistics and sensitivity indices were computed in closed form for source amplitudes. This analysis revealed for example, that auditory sLORETA amplitudes were most sensitive to the coregistration parameters which mainly affected the distance between sources and closest sensors. In MEG analysis, however, the source estimation amplitudes itself

are not as informative as its spatial and temporal distribution. Hence, the polynomial expansions were used to efficiently sample the spatial maximum distribution of the estimates for uncertain coregistrations. In such cases, where the expansion is used as efficient approximation, it is not as important to use an orthogonal polynomial basis as in cases where the statistics are directly derived from the coefficients. That is, for the distribution of the maximum location a non-orthogonal basis could be used providing even more efficient approximations. However, when the Smolyak pseudospectral approximation is used, adaptation can also provide more accurate and more efficient approximations compared to the fixed polynomial set of this thesis. The fixed polynomial sets were used for a better comparability of the expansion errors, for between beamformer and sLORETA or between loose parameter of 0 and 0.2.

In this thesis, the results for dynamic coregistration uncertainties were reported, that is, head movements are included in the uncertainties. When I compared the results with the static uncertainties for one single head position, I found only negligible differences to the dynamic ones. This is related to the observation, that the subjects moved their heads only a few millimeters at maximum. The MEG recordings were conducted with adults, who are able to keep their heads well at one position for several minutes. This would be different with children since they move their heads much more during recordings (Wehner et al., 2008).

The effect of coregistration on the maximum location was similar between beamformer and sLORETA with fixated orientations (a loose parameter of 0). On the main axis, the median location standard deviation was between 2 and 4 mm, dependent on the region, SNR and method, where the median was computed over subjects. For slightly variable orientations (loose parameter of 0.2), the beamformer maximum showed larger spatial deviations. Hence, when using orientation constraints, I recommend to use a strictly fixated (loose parameter of 0) surface normal constraint for beamformers. In this thesis, localization errors were computed as spatial differences between the mean maximum location (centre of the ellipsoids) and the centre of the source patches. Compared the standard deviation of the maximum location, similar localization errors are found with median values almost always smaller then 5 mm per axis. This is in contrast to the results of Zetter et al. (2018), who reported similar localization errors but smaller effects of coregistration uncertainty on the localization errors. Zetter et al. (2018) investigated the effect of coregistration uncertainty on source estimates in on-scalp MEG. They found that sensor position errors of less than 4 mm increase any of their source estimation error metrics by no more than 8 %. On the one hand, this could be explained by the different error metric. They

reported the effect on the localization errors while in this thesis the effect on the maximum location itself was computed. On the other hand they used a different definition of coregistration uncertainty. In on-scalp MEG, each sensor is localized individually with respect to the head. This changes the nature of coregistration uncertainties: in this thesis (sensors inside the MEG helmet), the uncertainties are systematic shifts or rotations of the whole sensor array, while in on-scalp MEG, the dominant uncertainty is sensor-wise (Zetter et al., 2018). Sensor localization uncertainties are likely to cancel each other out to a certain extent, depending on the number of sensors. This may explain the smaller localization errors found by Zetter et al. (2018). Concerning the forward solutions, Zetter et al. (2018) found comparable difference measures on the field topographies as found in this thesis. This may reveal that it is not straightforward to link localization errors and measures of field topography differences like the RDM if the sensor arrays are different. When sensor-wise errors yield similar RDMs as systematic shifts or rotations of the whole sensor array, it is likely to find smaller effects on the source localization errors for sensor-wise errors.

The head position measurements, which were assessed in this thesis, were conducted according to the following MEG guidelines. Bagić et al. (2011) recommend to use at least three localization coils, the data reported in this thesis was measured with five localization coils. Hence, I recommend using at least five localization coils in order to achieve the accuracy reported in this thesis. It is recommended that the coil positions are covered by the sensor array (Gross et al., 2013) which was fulfilled for the data reported in section 4.3. Bagić et al. (2011) and Hari et al. (2018) further recommend to continuously measure head positions during recordings which was done for the data of all 20 subjects reported in section 4.3. In section 3.4.2, a method is proposed to incorporate continuously measured head positions in the distribution of coregistration parameters. This method was used in all uncertainty analyses reported in section 4.3.2. All coregistrations of this thesis were visually inspected as recommended by Gross et al. (2013). The MRIs used in this thesis follows the recommendation of 1 mm slice thickness and skin to skin MRI head coverage for proper coregistration (Burgess et al., 2011). Burgess et al. (2011) recommend the digitization of at least 100 head shape points for coregistration. The number of head shape points of the 20 subjects was between 475 and 857 in this thesis. For reporting on spatial coordinates, Keil et al. (2014) recommend detailed methods for obtaining these parameters and providing a measure of spatial variability or measurement error. In this thesis, source localization errors, confidence ellipsoids of source locations and the TREs are provided.

For compensation of head movements or as general noise reduction, the signal space separation (SSS) (Taulu and Kajola, 2005) is commonly used as an early pre-processing step in the MEG analysis. The compensation of head movements requires continuous recording of the localization coil signals which typically operate close the upper frequency band limit of the recording. These coil signals need to be removed before MEG analysis by low pass filtering which effectively reduces the bandwidth of the data. This compromise between head positions and bandwidth is usually decided in favor of head positions, which is also the recommendation of clinical MEG guidelines (Bagić et al., 2011; Hari et al., 2018). When the SSS is applied, a linear combination of harmonic components is fitted to the MEG data. The harmonic components are grouped into internal and external ones. SSS discards the external ones and reconstructs cleaner MEG data by backprojecting the internal components only (Garcés et al., 2017). For the internal components, an expansion origin needs to be chosen inside the head volume. The effect of the position of that origin on forward solutions and source estimates could be investigated by polynomial expansions according to the methods of this thesis. Since the SSS reduces the dimensionality and especially limits the spatial frequency of the data (Garcés et al., 2017), it affects source estimates. Besides the origin, the number of internal and external components as well as the regularization is variable in the SSS method. Hence, the methods proposed in this thesis could be applied to SSS and sensitivities of source estimates to individual variables could be investigated.

By using the uncertainty propagation methods of this thesis, it is possible to analyse the effects on source estimation amplitudes and maximum locations. Such an analysis can assist the decision whether a movement compensation, for example via a signal space separation (Taulu and Kajola, 2005), should be used. The maximum location confidence ellipsoid can also be used to decide whether a measurement block should be excluded or not.

From the uncertainty analysis of source estimates, it can be concluded:

1. It is possible to apply stochastic spectral methods to MEG source estimation with high accuracy.

2. The investigated effects of coregistration uncertainties on source estimates are small, typically the maximum location varied within a range of 5 mm. This is in the range of the localization errors. That is, high accuracy in source estimation was achieved for TREs of approximately 2 mm.

3. Polynomial expansions of the source estimates reduced computation times considerably by a factor of approximately 10 000 for beamformer and 50 000 for

sLORETA compared to the exact original computations. This speedup enabled the Monte Carlo simulations of this thesis.

References

Adjamian, P. et al. (Mar. 2004). "Co-registration of magnetoencephalography with magnetic resonance imaging using bite-bar-based fiducials and surface-matching". In: *Clinical Neurophysiology* 115.3, pp. 691–698.

Ahlfors, Seppo P. and Risto J Ilmoniemi (1989). "Magnetometer position indicator for multichannel MEG". In: *Advances in Biomagnetism*. Ed. by Samuel J Williamson et al. Boston, MA: Springer US, pp. 693–696.

Bagić, Anto I. et al. (2011). "American Clinical MEG Society (ACMEGS) Clinical Practice Guideline (CPG) #1 (ACMEGS CPG#1): Recording And Analysis Of Spontaneous Cerebral Activity". In: *Journal of clinical neurophysiology* 28.4, pp. 348–354.

Baysal, Uğur and Gökhan Şengül (Apr. 2010). "Single camera photogrammetry system for EEG electrode identification and localization". In: *Annals of Biomedical Engineering* 38.4, pp. 1539–1547.

Besl, P.J. and Neil D. McKay (Feb. 1992). "A method for registration of 3-D shapes". In: *IEEE Transactions on Pattern Analysis and Machine Intelligence* 14.2, pp. 239–256.

Björck, Åke (2015). "Linear Least Squares Problems". In: *Numerical Methods in Matrix Computations*. Cham: Springer International Publishing, pp. 211–430.

Brendemühl, Astrid et al. (2007). "Intensity-Modulated Radiation Therapy — Quality Assurance with the Mutual Information Index (MI)". In: *Advances in Medical Engineering*. Ed. by Thorsten M Buzug et al. Berlin, Heidelberg: Springer Berlin Heidelberg, pp. 205–210.

Burgess, Richard C. et al. (2011). "American clinical magnetoencephalography society clinical practice guideline 2: Presurgical functional brain mapping using magnetic evoked fields". In: *Journal of Clinical Neurophysiology* 28.4, pp. 355–361.

Burkardt, John and Clayton Webster (2014). "Slow Growth for Gauss Legendre Sparse Grids". In: pp. 1–6.

Chen, C.S., M.A. Golberg, and Y.C. Hon (July 1998). "Numerical justification of fundamental solutions and the quasi-Monte Carlo method for Poisson-type equations". In: *Engineering Analysis with Boundary Elements* 22.1, pp. 61–69.

Cheveigné, Alain de and Dorothée Arzounian (2018). "Robust detrending, rereferencing, outlier detection, and inpainting for multichannel data". In: *NeuroImage* 172, pp. 903–912.

Conrad, Patrick R. and Youssef M. Marzouk (Jan. 2013). "Adaptive Smolyak Pseudospectral Approximations". In: *SIAM Journal on Scientific Computing* 35.6, A2643–A2670.

De Staelen, R. H. et al. (2013). *Bayesian inference in the uncertain EEG problem including local information and a sensor correlation matrix*.

Economo, C. von and G.N. Koskinas (1925). *Die Cytoarchitektonik der Hirnrinde des Erwachsenen Menschen: Textband und Atlas*. Wien: Springer.

Elekta Neuromag data acquisition user's manual (2007).

Escudero, Javier et al. (Nov. 2007). "Artifact Removal in Magnetoencephalogram Background Activity With Independent Component Analysis". In: *IEEE Transactions on Biomedical Engineering* 54.11, pp. 1965–1973.

Evans, A.C. et al. (1993). "3D statistical neuroanatomical models from 305 MRI volumes". In: *1993 IEEE Conference Record Nuclear Science Symposium and Medical Imaging Conference*. IEEE, pp. 1813–1817.

Ferguson, A.S., Xu Zhang, and G Stroink (May 1994). "A complete linear discretization for calculating the magnetic field using the boundary element method". In: *IEEE Transactions on Biomedical Engineering* 41.5, pp. 455–460.

Fitzpatrick, J Michael (2009). "Fiducial registration error and target registration error are uncorrelated". In: *Proc. SPIE*. Vol. 7261, pp. 1–12.

Fuchs, Manfred et al. (Apr. 1995). "Coordinate system matching for neuromagnetic and morphological reconstruction overlay". In: *IEEE Transactions on Biomedical Engineering* 42.4, pp. 416–420.

Garcés, Pilar et al. (Dec. 2017). "Choice of Magnetometers and Gradiometers after Signal Space Separation". In: *Sensors* 17.12, p. 2926.

Geselowitz, D. (June 1970). "On the magnetic field generated outside an inhomogeneous volume conductor by internal current sources". In: *IEEE Transactions on Magnetics* 6.2, pp. 346–347.

Ghanem, Roger G. and Pol D. Spanos (1991). *Stochastic Finite Elements: A Spectral Approach*. New York, NY: Springer New York, p. 222.

Glasser, Matthew F et al. (July 2016). "A multi-modal parcellation of human cerebral cortex". In: *Nature* 536, p. 171.

Gramfort, Alexandre (2013). “MEG and EEG data analysis with MNE-Python”. In: *Frontiers in Neuroscience* 7.12, pp. 1–13.

Gross, Joachim et al. (2013). “Good practice for conducting and reporting MEG research”. In: *NeuroImage* 65, pp. 349–363.

Haario, Heikki, Marko Laine, et al. (Dec. 2006). “DRAM: efficient adaptive MCMC”. In: *Statistics and Computing* 16.4, pp. 339–354.

Haario, Heikki, Eero Saksman, and Johanna Tamminen (Apr. 2001). “An adaptive Metropolis algorithm”. In: *Bernoulli* 7.2, pp. 223–242.

Hämäläinen, Matti S. (2010). *MNE software User's Guide*. 11.

Hämäläinen, Matti S., Fa Hsuan Lin, and John C. Mosher (2010). “Anatomically and Functionally Constrained Minimum-Norm Estimates”. In: *MEG: An Introduction to Methods*, pp. 1–31.

Hansen, Peter C., Morten L. Kringelbach, and Riitta Salmelin (2010). *MEG: An Introduction to Methods*.

Hari, Riitta et al. (2018). “IFCN-endorsed practical guidelines for clinical magnetoencephalography (MEG)”. In: *Clinical Neurophysiology* 129.8, pp. 1720–1747.

Hillebrand, Arjan and Gareth R. Barnes (Dec. 2003). “The use of anatomical constraints with MEG beamformers.” In: *NeuroImage* 20.4, pp. 2302–2313.

— (Feb. 2011). “Practical constraints on estimation of source extent with MEG beamformers”. In: *NeuroImage* 54.4, pp. 2732–2740.

Hironaga, Naruhito et al. (Dec. 2014). “Proposal for a new MEG–MRI coregistration: a 3D laser scanner system”. In: *Clinical Neurophysiology* 125.12, pp. 2404–2412.

Huppertz, H.-J et al. (May 1998). “Estimation of the accuracy of a surface matching technique for registration of EEG and MRI data”. In: *Electroencephalography and Clinical Neurophysiology* 106.5, pp. 409–415.

Keil, Andreas et al. (2014). “Committee report: Publication guidelines and recommendations for studies using electroencephalography and magnetoencephalography”. In: *Psychophysiology* 51.1, pp. 1–21.

Koessler, L., T. Cecchin, et al. (Mar. 2011). “EEG–MRI co-registration and sensor labeling using a 3D laser scanner”. In: *Annals of Biomedical Engineering* 39.3, pp. 983–995.

Koessler, L., L. Maillard, et al. (Apr. 2007). “Spatial localization of EEG electrodes”. In: *Neurophysiologie Clinique/Clinical Neurophysiology* 37.2, pp. 97–102.

Küstner, T et al. (2018). “A machine-learning framework for automatic reference-free quality assessment in MRI”. In: *Magnetic Resonance Imaging* 53, pp. 134–147.

Lin, Fa-Hsuan et al. (Jan. 2006). "Distributed current estimates using cortical orientation constraints". In: *Human Brain Mapping* 27.1, pp. 1–13.

Lin, Yicong et al. (2018). "Lateralization value of low frequency band beamformer magnetoencephalography source imaging in temporal lobe epilepsy". In: *Frontiers in Neurology* 9.10.

Loh, Wei Liem (1996). "On latin hypercube sampling". In: *Annals of Statistics* 24.5, pp. 2058–2080.

Markley, F. Landis, Yang Cheng, et al. (2007). "Quaternion Averaging". In: *NASA Goddard Space Flight Center*, pp. 1–10.

Markley, F. Landis and Daniele Mortari (2000). "New developments in quaternion estimation from vector observations". In: *Advances in the Astronautical Sciences* 106, pp. 373–393.

Meijs, Jan W. H. et al. (1989). "Method". In: *10* 36.10, pp. 1038–1049.

Meyer, Sofie S. et al. (Jan. 2017). "Flexible head-casts for high spatial precision MEG". In: *Journal of Neuroscience Methods* 276, pp. 38–45.

Milde, Thomas et al. (2009). "Modelling of cortical and thalamic 600Hz activity by means of oscillatory networks". In: *Journal of Physiology-Paris* 103.6, pp. 342–347.

Mulugeta, Lealem et al. (2018). "Credibility, Replicability, and Reproducibility in Simulation for Biomedicine and Clinical Applications in Neuroscience". In: *Frontiers in Neuroinformatics* 12.

Nolte, G. and Matti S. Hämäläinen (Nov. 2001). "Partial signal space projection for artefact removal in MEG measurements: a theoretical analysis". In: *Physics in Medicine and Biology* 46.11, pp. 2873–2887.

Papadelis, Christos et al. (2009). "MEG's ability to localise accurately weak transient neural sources". In: *Clinical Neurophysiology* 120.11, pp. 1958–1970.

Parno, Matthew, Andrew Davis, and Patrick R. Conrad (2017). *MIT Uncertainty Quantification Library (MUQ)*. https://bitbucket.org/mituq/muq.

Pascual-Marqui, R. D. (2002). "Standardized low resolution brain electromagnetic tomography (sLORETA)". In: *Methods & Findings in Experimental & Clinical Pharmacology* 24, pp. 5–12.

Pedregosa, Fabian et al. (Jan. 2012). "Scikit-learn: machine learning in Python". In: *The Journal of Machine Learning Research* 12, pp. 2825–2830.

Polhemus (2012). *3SPACE FASTRAK User Manual*. 6.

Pratt, John W and Jean D Gibbons (1981). "Kolmogorov-Smirnov Two-Sample Tests". In: *Concepts of Nonparametric Theory*. New York, NY: Springer New York, pp. 318–344.

Press, William H et al. (1992). *Numerical recipes in C: the art of scientific computing.* 2nd ed. New York, NY, USA: Cambridge University Press.

Qian, Shuo and Yang Sheng (Nov. 2011). "A single camera photogrammetry system for multi-angle fast localization of EEG electrodes". In: *Annals of Biomedical Engineering* 39.11, pp. 2844–2856.

Saltelli, Andrea (May 2002). "Making best use of model evaluations to compute sensitivity indices". In: *Computer Physics Communications* 145.2, pp. 280–297.

Saltelli, Andrea et al. (Feb. 2010). "Variance based sensitivity analysis of model output. Design and estimator for the total sensitivity index". In: *Computer Physics Communications* 181.2, pp. 259–270.

Sarvas, J. (Jan. 1987). "Basic mathematical and electromagnetic concepts of the biomagnetic inverse problem". In: *Physics in Medicine and Biology* 32.1, pp. 11–22.

Saturnino, Guilherme B. et al. (Mar. 2019). "A principled approach to conductivity uncertainty analysis in electric field calculations". In: *NeuroImage* 188.12, pp. 821–834.

Schmidt, Christian et al. (2014). "Impact of Uncertain Head Tissue Conductivity in the Optimization of Transcranial Direct Current Stimulation for an Auditory Target". In:

Schwartz, D. et al. (Dec. 1996). "Registration of MEG/EEG data with 3D MRI: methodology and precision issues". In: *Brain Topography* 9.2, pp. 101–116.

Sekihara, Kensuke et al. (2001). "Reconstructing spatio-temporal activities of neural sources using an MEG vector beamformer technique". In: *IEEE Transactions on Biomedical Engineering* 48.7, pp. 760–771.

Singh, K. D et al. (Feb. 1997). "Evaluation of MRI-MEG / EEG co-registration strategies using Monte Carlo simulation". In: *Electroencephalography and Clinical Neurophysiology* 2.102, pp. 81–85.

Stenroos, Matti, V. Mäntynen, and J. Nenonen (Dec. 2007). "A Matlab library for solving quasi-static volume conduction problems using the boundary element method". In: *Computer Methods and Programs in Biomedicine* 88.3, pp. 256–263.

Taguchi, Katsuyuki et al. (2018). "Spatio-energetic cross-talk in photon counting detectors: Numerical detector model (PcTK) and workflow for CT image quality assessment". In: *Medical Physics* 45.5, pp. 1985–1998.

Taulu, Samu and Matti Kajola (June 2005). "Presentation of electromagnetic multichannel data: The signal space separation method". In: *Journal of Applied Physics* 97.12, p. 124905.

Troebinger, Luzia et al. (Feb. 2014). “High precision anatomy for MEG”. In: *NeuroImage* 86, pp. 583–591.

Uutela, K, Samu Taulu, and Matti S. Hämäläinen (Dec. 2001). “Detecting and Correcting for Head Movements in Neuromagnetic Measurements”. In: *NeuroImage* 14.6, pp. 1424–1431.

Van Veen, B.D. et al. (1997). “Localization of brain electrical activity via linearly constrained minimum variance spatial filtering”. In: *IEEE Transactions on Biomedical Engineering* 44.9, pp. 867–880.

Wagner, Michael and Manfred Fuchs (2001). “Integration of functional MRI, structural MRI, EEG, and MEG”. In: *International Journal of Bioelectromagnetism* 3.1, pp. 1–15.

Wehner, Daniel T. et al. (Apr. 2008). “Head movements of children in MEG: Quantification, effects on source estimation, and compensation”. In: *NeuroImage* 40.2, pp. 541–550.

Weise, Konstantin et al. (July 2015). “Uncertainty Analysis in Transcranial Magnetic Stimulation Using Nonintrusive Polynomial Chaos Expansion”. In: *IEEE Transactions on Magnetics* 51.7, pp. 1–8.

Weppler, Sarah et al. (2018). “Framework for the quantitative assessment of adaptive radiation therapy protocols”. In: *Journal of Applied Clinical Medical Physics* 19.6, pp. 26–34.

Wheeler, Mark D. and Katsushi Ikeuchi (1995). “Iterative Estimation of Rotation and Translation using the Quaternion”. In:

Wiener, Norbert (1938). “The Homogeneous Chaos”. In: 60.4, pp. 897–936.

Xiu, Dongbin (2009). “Fast Numerical Methods for Stochastic Computations : A Review”. In: *Communications in Computational Physics* 5.2, pp. 242–272.

Xiu, Dongbin and Jan S. Hesthaven (Jan. 2005). “High-Order Collocation Methods for Differential Equations with Random Inputs”. In: *SIAM Journal on Scientific Computing* 27.3, pp. 1118–1139.

Xiu, Dongbin and George Em Karniadakis (Jan. 2002). “The Wiener–Askey Polynomial Chaos for Stochastic Differential Equations”. In: *SIAM Journal on Scientific Computing* 24.2, pp. 619–644.

— (May 2003). “Modeling uncertainty in flow simulations via generalized polynomial chaos”. In: *Journal of Computational Physics* 187.1, pp. 137–167.

Zetter, Rasmus et al. (Nov. 2018). “Requirements for Coregistration Accuracy in On-Scalp MEG”. In: *Brain Topography* 31.6, pp. 931–948.

List of Figures

List of Tables

Erklärung

Ich versichere, dass ich die vorliegende Arbeit ohne unzulässige Hilfe Dritter und ohne Benutzung anderer als der angegebenen Hilfsmittel angefertigt habe. Die aus anderen Quellen direkt oder indirekt übernommenen Daten und Konzepte sind unter Angabe der Quelle gekennzeichnet. Bei der Auswahl und Auswertung folgenden Materials haben mir die nachstehend aufgeführten Personen in der jeweils beschriebenen Weise unentgeltlich geholfen:

1. Hilfe bei der Beschreibung der Methoden in Kapitel 3.2.

   Dr.-Ing. Konstantin Weise
   Postdoc (in Kooperation mit TU Ilmenau)
   Methoden- und Entwicklungsgruppe „MEG und EEG – Kortikale Netzwerke und Kognitive Funktionen“
   Max-Planck-Institut für Kognitions- und Neurowissenschaften,
   Leipzig, Deutschland

2. Hilfe bei der Implementierung numerischer Feldberechnungsmethoden in Kapitel 3.5.3 durch Bereitstellung einer BEM-Software-Bibliothek.

   PhD Matti Stenroos
   Senior University Lecturer
   Department of Neuroscience and Biomedical Engineering
   Aalto University, Helsinki, Finnland

3. Hilfe bei Interpretation von Ergebnissen und bei der Projektplanung der gesamten Arbeit.

   Dr. Burkhard Maeß
   Gruppenleiter
   Methoden- und Entwicklungsgruppe „MEG und EEG – Kortikale Netzwerke und Kognitive Funktionen“
   Max-Planck-Institut für Kognitions- und Neurowissenschaften,
   Leipzig, Deutschland

   Prof. Dr.-Ing. habil. Jens Haueisen
   Institutsleiter und Fachgebietsleiter Biomedizinische Technik
   Institut für Biomedizinische Technik und Informatik
   Technische Universität Ilmenau, Ilmenau, Deutschland

Weitere Personen waren an der inhaltlich-materiellen Erstellung der vorliegenden Arbeit nicht beteiligt. Insbesondere habe ich hierfür nicht die entgeltliche Hilfe

von Vermittlungs- bzw. Beratungsdiensten (Promotionsberater oder anderer Personen) in Anspruch genommen. Niemand hat von mir unmittelbar oder mittelbar geldwerte Leistungen für Arbeiten erhalten, die im Zusammenhang mit dem Inhalt der vorgelegten Dissertation stehen. Die Arbeit wurde bisher weder im In- noch im Ausland in gleicher oder ähnlicher Form einer Prüfungsbehörde vorgelegt. Ich bin darauf hingewiesen worden, dass die Unrichtigkeit der vorstehenden Erklärung als Täuschungsversuch bewertet wird und gemäß § 7 Abs. 10 der Promotionsordnung den Abbruch des Promotionsverfahrens zur Folge hat.

Leipzig, 2. Mai 2019

MPI Series in Human Cognitive and Brain Sciences:

1 Anja Hahne
Charakteristika syntaktischer und semantischer Prozesse bei der auditiven Sprachverarbeitung: Evidenz aus ereigniskorrelierten Potentialstudien

2 Ricarda Schubotz
Erinnern kurzer Zeitdauern: Behaviorale und neurophysiologische Korrelate einer Arbeitsgedächtnisfunktion

3 Volker Bosch
Das Halten von Information im Arbeitsgedächtnis: Dissoziationen langsamer corticaler Potentiale

4 Jorge Jovicich
An investigation of the use of Gradient- and Spin-Echo (GRASE) imaging for functional MRI of the human brain

5 Rosemary C. Dymond
Spatial Specificity and Temporal Accuracy in Functional Magnetic Resonance Investigations

6 Stefan Zysset
Eine experimentalpsychologische Studie zu Gedächtnisabrufprozessen unter Verwendung der funktionellen Magnetresonanztomographie

7 Ulrich Hartmann
Ein mechanisches Finite-Elemente-Modell des menschlichen Kopfes

8 Bertram Opitz
Funktionelle Neuroanatomie der Verarbeitung einfacher und komplexer akustischer Reize: Integration haemodynamischer und elektrophysiologischer Maße

9 Gisela Müller-Plath
Formale Modellierung visueller Suchstrategien mit Anwendungen bei der Lokalisation von Hirnfunktionen und in der Diagnostik von Aufmerksamkeitsstörungen

10 Thomas Jacobsen
Characteristics of processing morphological structural and inherent case in language comprehension

11 Stefan Kölsch
Brain and Music
A contribution to the investigation of central auditory processing with a new electrophysiological approach

12 Stefan Frisch
Verb-Argument-Struktur, Kasus und thematische Interpretation beim Sprachverstehen

13 Markus Ullsperger
The role of retrieval inhibition in directed forgetting – an event-related brain potential analysis

14 Martin Koch
Measurement of the Self-Diffusion Tensor of Water in the Human Brain

15 Axel Hutt
Methoden zur Untersuchung der Dynamik raumzeitlicher Signale

16 Frithjof Kruggel
Detektion und Quantifizierung von Hirnaktivität mit der funktionellen Magnetresonanztomographie

17 Anja Dove
Lokalisierung an internen Kontrollprozessen beteiligter Hirngebiete mithilfe des Aufgabenwechselparadigmas und der ereigniskorrelierten funktionellen Magnetresonanztomographie

18 Karsten Steinhauer
Hirnphysiologische Korrelate prosodischer Satzverarbeitung bei gesprochener und geschriebener Sprache

19 Silke Urban
Verbinformationen im Satzverstehen

20 Katja Werheid
Implizites Sequenzlernen bei Morbus Parkinson

21 Doreen Nessler
Is it Memory or Illusion? Electrophysiological Characteristics of True and False Recognition

22 Christoph Herrmann
Die Bedeutung von 40-Hz-Oszillationen für kognitive Prozesse

23 Christian Fiebach
Working Memory and Syntax during Sentence Processing.
A neurocognitive investigation with event-related brain potentials and functional magnetic resonance imaging

24 Grit Hein
Lokalisation von Doppelaufgabendefiziten bei gesunden älteren Personen und neurologischen Patienten

25 Monica de Filippis
Die visuelle Verarbeitung unbeachteter Wörter. Ein elektrophysiologischer Ansatz

26 Ulrich Müller
Die katecholaminerge Modulation präfrontaler kognitiver Funktionen beim Menschen

27 Kristina Uhl
Kontrollfunktion des Arbeitsgedächtnisses über interferierende Information

28 Ina Bornkessel
The Argument Dependency Model: A Neurocognitive Approach to Incremental Interpretation

29 Sonja Lattner
Neurophysiologische Untersuchungen zur auditorischen Verarbeitung von Stimminformationen

30 Christin Grünewald
Die Rolle motorischer Schemata bei der Objektrepräsentation: Untersuchungen mit funktioneller Magnetresonanztomographie

31 Annett Schirmer
Emotional Speech Perception: Electrophysiological Insights into the Processing of Emotional Prosody and Word Valence in Men and Women

32 André J. Szameitat
Die Funktionalität des lateral-präfrontalen Cortex für die Verarbeitung von Doppelaufgaben

33 Susanne Wagner
Verbales Arbeitsgedächtnis und die Verarbeitung ambiger Wörter in Wort- und Satzkontexten

34 Sophie Manthey
Hirn und Handlung: Untersuchung der Handlungsrepräsentation im ventralen prämotorischen Cortex mit Hilfe der funktionellen Magnet-Resonanz-Tomographie

35 Stefan Heim
Towards a Common Neural Network Model of Language Production and Comprehension: fMRI Evidence for the Processing of Phonological and Syntactic Information in Single Words

36 Claudia Friedrich
Prosody and spoken word recognition: Behavioral and ERP correlates

37 Ulrike Lex
Sprachlateralisierung bei Rechts- und Linkshändern mit funktioneller Magnetresonanztomographie

38 Thomas Arnold
Computergestützte Befundung klinischer Elektroenzephalogramme

39 Carsten H. Wolters
Influence of Tissue Conductivity Inhomogeneity and Anisotropy on EEG/MEG based Source Localization in the Human Brain

40 Ansgar Hantsch
Fisch oder Karpfen? Lexikale Aktivierung von Benennungsalternative bei der Objektbenennung

41 Peggy Bungert
Zentralnervöse Verarbeitung akustischer Informationen Signalidentifikation, Signallateralisation und zeitgebundene Informationsverarbeitung bei Patienten mit erworbenen Hirnschädigungen

42 Daniel Senkowski
Neuronal correlates of selective attention: An investigation of electrophysiological brain responses in the EEG and MEG

43 Gert Wollny
Analysis of Changes in Temporal Series of Medical Images

S 1 Markus Ullsperger & Michael Falkenstein
Errors, Conflicts, and the Brain Current Opinions on Performance Monitoring

44 Angelika Wolf
Sprachverstehen mit Cochlea-Implantat: EKP-Studien mit postlingual ertaubten erwachsenen CI-Trägern

45 Kirsten G. Volz
Brain correlates of uncertain decisions: Types and degrees of uncertainty

46 Hagen Huttner
Magnetresonanztomographische Untersuchungen über die anatomische Variabilität des Frontallappens des menschlichen Großhirns

47 Dirk Köster
Morphology and Spoken Word Comprehension: Electrophysiological Investigations of Internal Compound Structure

48 Claudia A. Hruska
Einflüsse kontextueller und prosodischer Informationen in der auditorischen Satzverarbeitung: Untersuchungen mit ereigniskorrelierten Hirnpotentialen

49 Hannes Ruge
Eine Analyse des raum-zeitlichen Musters neuronaler Aktivierung im Aufgabenwechselparadigma zur Untersuchung handlungssteuernder Prozesse

50 Ricarda I. Schubotz
Human premotor cortex: Beyond motor performance

51 Clemens von Zerssen
Bewusstes Erinnern und falsches Wiedererkennen: Eine funktionelle MRT Studie neuroanatomischer Gedächtniskorrelate

52 Christiane Weber
Rhythm is gonna get you.
Electrophysiological markers of rhythmic processing in infants with and without risk for Specific Language Impairment (SLI)

53 Marc Schönwiesner
Functional Mapping of Basic Acoustic Parameters in the Human Central Auditory System

54 Katja Fiehler
Temporospatial characteristics of error correction

55 Britta Stolterfoht
Processing Word Order Variations and Ellipses: The Interplay of Syntax and Information Structure during Sentence Comprehension

56 Claudia Danielmeier
Neuronale Grundlagen der Interferenz zwischen Handlung und visueller Wahrnehmung

57 Margret Hund-Georgiadis
Die Organisation von Sprache und ihre Reorganisation bei ausgewählten, neurologischen Erkrankungen gemessen mit funktioneller Magnetresonanztomographie – Einflüsse von Händigkeit, Läsion, Performanz und Perfusion

58 Jutta L. Mueller
Mechanisms of auditory sentence comprehension in first and second language: An electrophysiological miniature grammar study

59 Franziska Biedermann
Auditorische Diskriminationsleistungen nach unilateralen Läsionen im Di- und Telenzephalon

60 Shirley-Ann Rüschemeyer
The Processing of Lexical Semantic and Syntactic Information in Spoken Sentences: Neuroimaging and Behavioral Studies of Native and Non-Native Speakers

61 Kerstin Leuckefeld
The Development of Argument Processing Mechanisms in German. An Electrophysiological Investigation with School-Aged Children and Adults

62 Axel Christian Kühn
Bestimmung der Lateralisierung von Sprachprozessen unter besondere Berücksichtigung des temporalen Cortex, gemessen mit fMRT

63 Ann Pannekamp
Prosodische Informationsverarbeitung bei normalsprachlichem und deviantem Satzmaterial: Untersuchungen mit ereigniskorrelierten Hirnpotentialen

64 Jan Derrfuß
Functional specialization in the lateral frontal cortex: The role of the inferior frontal junction in cognitive control

65 Andrea Mona Philipp
The cognitive representation of tasks – Exploring the role of response modalities using the task-switching paradigm

66 Ulrike Toepel
Contrastive Topic and Focus Information in Discourse – Prosodic Realisation and Electrophysiological Brain Correlates

67 Karsten Müller
Die Anwendung von Spektral- und Waveletanalyse zur Untersuchung der Dynamik von BOLD-Zeitreihen verschiedener Hirnareale

68 Sonja A.Kotz
The role of the basal ganglia in auditory language processing: Evidence from ERP lesion studies and functional neuroimaging

69 Sonja Rossi
The role of proficiency in syntactic second language processing: Evidence from event-related brain potentials in German and Italian

70 Birte U. Forstmann
Behavioral and neural correlates of endogenous control processes in task switching

71 Silke Paulmann
Electrophysiological Evidence on the Processing of Emotional Prosody: Insights from Healthy and Patient Populations

72 Matthias L. Schroeter
Enlightening the Brain – Optical Imaging in Cognitive Neuroscience

73 Julia Reinholz
Interhemispheric interaction in object- and word-related visual areas

74 Evelyn C. Ferstl
The Functional Neuroanatomy of Text Comprehension

75 Miriam Gade
Aufgabeninhibition als Mechanismus der Konfliktreduktion zwischen Aufgabenrepräsentationen

76 Juliane Hofmann
Phonological, Morphological, and Semantic Aspects of Grammatical Gender Processing in German

77 Petra Augurzky
Attaching Relative Clauses in German – The Role of Implicit and Explicit Prosody in Sentence Processing

78 Uta Wolfensteller
Habituelle und arbiträre sensomotorische Verknüpfungen im lateralen prämotorischen Kortex des Menschen

79 Päivi Sivonen
Event-related brain activation in speech perception: From sensory to cognitive processes

80 Yun Nan
Music phrase structure perception: the neural basis, the effects of acculturation and musical training

81 Katrin Schulze
Neural Correlates of Working Memory for Verbal and Tonal Stimuli in Nonmusicians and Musicians With and Without Absolute Pitch

82 Korinna Eckstein
Interaktion von Syntax und Prosodie beim Sprachverstehen: Untersuchungen anhand ereigniskorrelierter Hirnpotentiale

83 Florian Th. Siebörger
Funktionelle Neuroanatomie des Textverstehens: Kohärenzbildung bei Witzen und anderen ungewöhnlichen Texten

84 Diana Böttger
Aktivität im Gamma-Frequenzbereich des EEG: Einfluss demographischer Faktoren und kognitiver Korrelate

85 Jörg Bahlmann
Neural correlates of the processing of linear and hierarchical artificial grammar rules: Electrophysiological and neuroimaging studies

86 Jan Zwickel
Specific Interference Effects Between Temporally Overlapping Action and Perception

87 Markus Ullsperger
Functional Neuroanatomy of Performance Monitoring: fMRI, ERP, and Patient Studies

88 Susanne Dietrich
Vom Brüllen zum Wort – MRT-Studien zur kognitiven Verarbeitung emotionaler Vokalisationen

89 Maren Schmidt-Kassow
What's Beat got to do with ist? The Influence of Meter on Syntactic Processing: ERP Evidence from Healthy and Patient populations

90 Monika Lück
Die Verarbeitung morphologisch komplexer Wörter bei Kindern im Schulalter: Neurophysiologische Korrelate der Entwicklung

91 Diana P. Szameitat
Perzeption und akustische Eigenschaften von Emotionen in menschlichem Lachen

92 Beate Sabisch
Mechanisms of auditory sentence comprehension in children with specific language impairment and children with developmental dyslexia: A neurophysiological investigation

93 Regine Oberecker
Grammatikverarbeitung im Kindesalter: EKP-Studien zum auditorischen Satzverstehen

94 Şükrü Barış Demiral
Incremental Argument Interpretation in Turkish Sentence Comprehension

95 Henning Holle
The Comprehension of Co-Speech Iconic Gestures: Behavioral, Electrophysiological and Neuroimaging Studies

96 Marcel Braß
Das inferior frontale Kreuzungsareal und seine Rolle bei der kognitiven Kontrolle unseres Verhaltens

97 Anna S. Hasting
Syntax in a blink: Early and automatic processing of syntactic rules as revealed by event-related brain potentials

98 Sebastian Jentschke
Neural Correlates of Processing Syntax in Music and Language – Influences of Development, Musical Training and Language Impairment

99 Amelie Mahlstedt
The Acquisition of Case marking Information as a Cue to Argument Interpretation in German
An Electrophysiological Investigation with Pre-school Children

100 Nikolaus Steinbeis
Investigating the meaning of music using EEG and fMRI

101 Tilmann A. Klein
Learning from errors: Genetic evidence for a central role of dopamine in human performance monitoring

102 Franziska Maria Korb
Die funktionelle Spezialisierung des lateralen präfrontalen Cortex: Untersuchungen mittels funktioneller Magnetresonanztomographie

103 Sonja Fleischhauer
Neuronale Verarbeitung emotionaler Prosodie und Syntax: die Rolle des verbalen Arbeitsgedächtnisses

104 Friederike Sophie Haupt
The component mapping problem: An investigation of grammatical function reanalysis in differing experimental contexts using eventrelated brain potentials

105 Jens Brauer
Functional development and structural maturation in the brain's neural network underlying language comprehension

106 Philipp Kanske
Exploring executive attention in emotion: ERP and fMRI evidence

107 Julia Grieser Painter
Music, meaning, and a semantic space for musical sounds

108 Daniela Sammler
The Neuroanatomical Overlap of Syntax Processing in Music and Language - Evidence from Lesion and Intracranial ERP Studies

109 Norbert Zmyj
Selective Imitation in One-Year-Olds: How a Model's Characteristics Influence Imitation

110 Thomas Fritz
Emotion investigated with music of variable valence – neurophysiology and cultural influence

111 Stefanie Regel
The comprehension of figurative language: Electrophysiological evidence on the processing of irony

112 Miriam Beisert
Transformation Rules in Tool Use

113 Veronika Krieghoff
Neural correlates of Intentional Actions

114 Andreja Bubić
Violation of expectations in sequence processing

115 Claudia Männel
Prosodic processing during language acquisition: Electrophysiological studies on intonational phrase processing

116 Konstanze Albrecht
Brain correlates of cognitive processes underlying intertemporal choice for self and other

117 Katrin Sakreida
Nicht-motorische Funktionen des prämotorischen Kortex: Patientenstudien und funktionelle Bildgebung

118 Susann Wolff
The interplay of free word order and pro-drop in incremental sentence processing: Neurophysiological evidence from Japanese

119 Tim Raettig
The Cortical Infrastructure of Language Processing: Evidence from Functional and Anatomical Neuroimaging

120 Maria Golde
Premotor cortex contributions to abstract and action-related relational processing

121 Daniel S. Margulies
Resting-State Functional Connectivity fMRI: A new approach for assessing functional neuroanatomy in humans with applications to neuroanatomical, developmental and clinical questions

122 Franziska Süß
The interplay between attention and syntactic processes in the adult and developing brain: ERP evidences

123 Stefan Bode
From stimuli to motor responses: Decoding rules and decision mechanisms in the human brain

124 Christiane Diefenbach
Interactions between sentence comprehension and concurrent action: The role of movement effects and timing

125 Moritz M. Daum
Mechanismen der frühkindlichen Entwicklung des Handlungsverständnisses

126 Jürgen Dukart
Contribution of FDG-PET and MRI to improve Understanding, Detection and Differentiation of Dementia

127 Kamal Kumar Choudhary
Incremental Argument Interpretation in a Split Ergative Language: Neurophysiological Evidence from Hindi

128 Peggy Sparenberg
Filling the Gap: Temporal and Motor Aspects of the Mental Simulation of Occluded Actions

129 Luming Wang
The Influence of Animacy and Context on Word Order Processing: Neurophysiological Evidence from Mandarin Chinese

130 Barbara Ettrich
Beeinträchtigung frontomedianer Funktionen bei Schädel-Hirn-Trauma

131 Sandra Dietrich
Coordination of Unimanual Continuous Movements with External Events

132 R. Muralikrishnan
An Electrophysiological Investigation Of Tamil Dative-Subject Constructions

133 Christian Obermeier
Exploring the significance of task, timing and background noise on gesture-speech integration

134 Björn Herrmann
Grammar and perception: Dissociation of early auditory processes in the brain

135 Eugenia Solano-Castiella
In vivo anatomical segmentation of the human amygdala and parcellation of emotional processing

136 Marco Taubert
Plastizität im sensomotorischen System – Lerninduzierte Veränderungen in der Struktur und Funktion des menschlichen Gehirns

137 Patricia Garrido Vásquez
Emotion Processing in Parkinson's Disease: The Role of Motor Symptom Asymmetry

138 Michael Schwartze
Adaptation to temporal structure

139 Christine S. Schipke
Processing Mechanisms of Argument Structure and Case-marking in Child Development: Neural Correlates and Behavioral Evidence

140 Sarah Jessen
Emotion Perception in the Multisensory Brain

141 Jane Neumann
Beyond activation detection: Advancing computational techniques for the analysis of functional MRI data

142 Franziska Knolle
Knowing what's next: The role of the cerebellum in generating predictions

143 Michael Skeide
Syntax and semantics networks in the developing brain

144 Sarah M. E. Gierhan
Brain networks for language
Anatomy and functional roles of neural pathways supporting language comprehension and repetition

145 Lars Meyer
The Working Memory of Argument-Verb Dependencies
Spatiotemporal Brain Dynamics during Sentence Processing

146 Benjamin Stahl
Treatment of Non-Fluent Aphasia through Melody, Rhythm and Formulaic Language

147 Kathrin Rothermich
The rhythm's gonna get you: ERP and fMRI evidence on the interaction of metric and semantic processing

148 Julia Merrill
Song and Speech Perception – Evidence from fMRI, Lesion Studies and Musical Disorder

149 Klaus-Martin Krönke
Learning by Doing?
Gesture-Based Word-Learning and its Neural Correlates in Healthy Volunteers and Patients with Residual Aphasia

150 Lisa Joana Knoll
When the hedgehog kisses the frog
A functional and structural investigation of syntactic processing in the developing brain

151 Nadine Diersch
Action prediction in the aging mind

152 Thomas Dolk
A Referential Coding Account for the Social Simon Effect

153 Mareike Bacha-Trams
Neurotransmitter receptor distribution in Broca's area and the posterior superior temporal gyrus

154 Andrea Michaela Walter
The role of goal representations in action control

155 Anne Keitel
Action perception in development: The role of experience

156 Iris Nikola Knierim
Rules don't come easy: Investigating feedback-based learning of phonotactic rules in language.

157 Jan Schreiber
Plausibility Tracking: A method to evaluate anatomical connectivity and microstructural properties along fiber pathways

158 Katja Macher
Die Beteiligung des Cerebellums am verbalen Arbeitsgedächtnis

159 Julia Erb
The neural dynamics of perceptual adaptation to degraded speech

160 Philipp Kanske
Neural bases of emotional processing in affective disorders

161 David Moreno-Dominguez
Whole-brain cortical parcellation: A hierarchical method based on dMRI tractography

162 Maria Christine van der Steen
Temporal adaptation and anticipation mechanisms in sensorimotor synchronization

163 Antje Strauß
Neural oscillatory dynamics of spoken word recognition

164 Jonas Obleser
The brain dynamics of comprehending degraded speech

165 Corinna E. Bonhage
Memory and Prediction in Sentence Processing

S 2 Tania Singer, Bethany E. Kok, Boris Bornemann, Matthias Bolz, and Christina A. Bochow
The Resource Project
Background, Design, Samples, and Measurements

166 Anna Wilsch
Neural oscillations in auditory working memory

167 Dominique Goltz
Sustained Spatial Attention in Touch: Underlying Brain Areas and Their Interaction

168 Juliane Dinse
A Model-Based Cortical Parcellation Scheme for High-Resolution 7 Tesla MRI Data

169 Gesa Schaadt
Visual, Auditory, and Visual-Auditory Speech Processing in School Children with Writing Difficulties

170 Laura Verga
Learning together or learning alone: Investigating the role of social interaction in second language word learning

171 Eva Maria Quinque
Brain, mood and cognition in hypothyroidism

172 Malte Wöstmann
Neural dynamics of selective attention to speech in noise

173 Charles-Étienne Benoit
Music-based gait rehabilitation in Parkinson's disease

174 Anja Fengler
How the Brain Attunes to Sentence Processing Relating Behavior, Structure, and Function

175 Emiliano Zaccarella
Breaking Down Complexity: The Neural Basis of the Syntactic Merge Mechanism in the Human Brain

S 2 Tania Singer, Bethany E. Kok, Boris Bornemann, Matthias Bolz, and Christina A. Bochow
2nd Edition The Resource Project
Background, Design, Samples, and Measurements

176 Manja Attig
Handlungsverständnis in den ersten Lebensjahren: retrospektive und prospektive Verarbeitung

177 Andrea Reiter
Out of control behaviors?
Investigating mechanisms of behavioral control in alcohol addition, binge eating disorder, and associated risc factors

178 Anna Strotseva-Feinschmidt
The processing of complex syntax in early childhood

179 Smadar Ovadia-Caro
Plasticity following stroke: the recovery of functional networks as measured by resting-state functional connectivity

180 Indra Kraft
Predicting developmental dyslexia at a preliterate age by combining behavioral assessment with structural MRI

181 Sabine Frenzel
How actors become attractors
A neurocognitive investigation of linguistic actorhood

182 Anja Dietrich
Food craving regulation in the brain: the role of weight status and associated personality aspects

183 Haakon G. Engen
On the Endogenous Generation of Emotion

184 Seung-Goo Kim
Myeloarchitecture and Intrinsic Functional Connectivity of Auditory Cortex in Musicians with Absolute Pitch

185 Yaqiong Xiao
Resting-state functional connectivity in the brain and its relation to language development in preschool children

186 Sofie Louise Valk
The Structure of the Social Brain:
Dissociating socio-affective and socio-cognitive networks through the study of individual differences, brain plasticity, and disease models

187 Douglas Weinbrenner
Abstract pointing
ERP and behavioral evidence for its role in reference tracking

188 Elisabeth Kaminski
Augmenting dynamic balance performance by transcranial direct current stimulation

189 Claudia Barth
Exploring structural and functional brain dynamics across the menstrual cycle

190 Eleanor Elizabeth Harding
Neurocognitive entrainment to meter influences syntactic comprehension in music and language: An individual-differences approach

191 Maike Hoff
Motorische Plastizität über die Lebensspanne
Untersuchungen zur Reduktion altersbedingter feinmotorischer Defizite durch motorisches Lernen und nicht-invasiver Hirnstimulation

192 Viola Rjosk
Augmenting Motor Performance with Mirror Visual Feedback (MVF): Underlying Mechanisms and Neural Correlates

193 Charlotte Grosse Wiesmann
The Emergence of Theory of Mind
Cognitive and Neural Basis of False Belief Understanding in Preschool Ag

194 Michael A. Skeide
The brain basis of developmental dyslexia

195 Daniela Sammler
The melodic mind: Neural bases of intonation in speech and music

196 Niki K. Vavatzanidis
From syllables to words:
Language perception and language acquisition of young children with cochlear implants

197 Sebastian Huhn
The impact of nutrition on hippocampal function
Results of a literature review and a randomized controlled trial

198 Tomás Goucha
Conciliating language differences with universal competence in brain structure and function

199 Jana Kynast
What makes us social?
Investigating mindreading from the eyes in adulthood

200 Norman Forschack
Conscious and unconscious somatosensory perception and its modulation by attention

201 Ulrike Kuhl
The brain basis of emerging literacy and numeracy skills
Longitudinal neuroimaging evidence from kindergarten to primary school

202 Leon Kroczek
The impact of speaker information on language processing

203 Caroline Beese
The Effects of Neurocognitive Aging on Sentence Processing